An Epidemiological Crack Percolation Model with Application to Probabilities of Failure for Gas Turbines

Dissertation

submitted to the Faculty of Mathematics and Science

BERGISCHE
UNIVERSITÄT
WUPPERTAL

January, 2024

By:	Mathis Harder, M.Sc.
First Supervisor:	Prof. Dr. Hanno Gottschalk
Second Supervisor:	PD Dr. Matthias Rottmann

Acknowledgment

First of all, I would like to thank Prof. Dr. Hanno Gottschalk, my supervisor, for his support, invaluable guidance, and continuous motivation throughout the journey of completing this PhD thesis. His insightful ideas and constructive feedback have significantly contributed to the development and improvement of this research.
I am grateful to Julia for her support, encouragement and understanding. Her presence and encouragement have given me the strength and motivation to get through the challenges of this PhD thesis.
I am very thankful to my parents Uwe and Sabine for always supporting me, not only during my time at university.
I enjoyed the interesting cooperation with Siemens Energy and the RPTU Kaiserslautern-Landau, especially with Lucas Mäde and Philipp Lion. The discussions and exchange of ideas contributed to the success of this dissertation.
Thanks to my colleagues at the University of Wuppertal for the relaxed atmosphere. I enjoyed spending time with you.
Special thanks to my friends who managed to provide important distraction and relaxation even in the most stressful phases of the doctorate. In particular, I would like to thank Janine and Jan.

Contents

1. Introduction

1.1 Motivation

Due to their flexibility, gas turbines play an important role for the transition in energy generation to renewable energy source. They are used to offsetting load peaks in consumption and dips in production with renewable energies. Due to cold starts this application causes high thermal and mechanical loads in the turbine components. Special materials are used to manufacture the machine parts for use under these extreme conditions. Commonly used for such applications are Nickel-based super alloys.

To optimize maintenance cycles, ensure safe operation and design parts of a turbine, it is important to have knowledge of the probability of failure of large engineering components.

Standardized fatigue tests are used to determine material-specific key figures for estimating the fatigue life of components [71]. The failure times of the samples in these low cycle fatigue (LCF) tests scatter widely and failure occurs before the deterministic failure time is reached. Hence, safety factors are often used to account for these uncertainties in LCF lifetime and ensure the safe operation of components [15, 5].

An empirical local model for low-cycle fatigue based on a Poisson process model as presented in [61, 63] is a possible approach to model the statistical scatter in LCF lifetime. To address inhomogeneous load conditions, the model has been further developed with a notch support extension, as outlined in [49, 46]. Furthermore, related modeling was applied to other failure mechanisms such as high cycle fatigue (HCF) [48]. This branch of research has found practical applications, e.g. for the design of gas turbines [62, 63], manufacturing tolerance [48] and shape optimization [6, 26, 31, 29, 28].

While these models have proven effective in practical applications and have been validated through experiments, their empirical nature raises questions about the mechanical insights they provide into the complex micro-scale processes governing low cycle fatigue.

Nickel-based super alloys typically exhibit a relatively coarse grain structure. This specific grain configuration hinders homogenization effects on a size scale that is relevant for LCF crack formation. Moreover, when combined with the high anisotropic characteristic of the elasticity constants of nickel, the local grain structure has an important impact on the LCF lifetime of the material [72].

In recent research on LCF failure in macroscopic components, a diverse range of modeling approaches has emerged, particularly considering microstructural factors. One prominent category is multiscale models [40], which intricately integrate information spanning different length and time scales. These models capture the complex interplay between macroscopic loading conditions and microscopic material reactions, addressing mechanical processes on separate length scales and combining them through homogenization methods.

Multiscale modeling has demonstrated effectiveness in incorporating microstructural influences, such as directional grain solidification [64, 51] or non-metallic inclusions [16], into LCF lifetime predictions. This approach involves separate modeling on distinct scales, resulting in a model rooted in physical processes. However, a challenge arises in the intricate homogenization modeling required during scale transitions. Additionally, solutions for individual-scale models heavily rely on numerical approximations, often implemented through finite element methods (FEM). The use of nested finite element simulations significantly increases computational demands due to the inherent complexities in capturing multiscale interactions.

On the other hand, there are approaches explicitly considering the random nature of microstructures, one notable method being the stochastic finite element method (SFEM). Unlike traditional FEM, which assumes deterministic boundary conditions and material properties, SFEM incorporates random fields to specify these parameters [3, 57]. In a study [74], this approach was employed to investigate the influence of material variability and load fluctuations on the fatigue life of notched specimens. In another study [75], SFEM was utilized for a probabilistic fatigue analysis of a turbine blade under realistic loading conditions, and in [56], the authors applied the SFEM framework to explore the influence of material variability, load variation, and geometrical uncertainty on the fatigue reliability of a turbine blade. While SFEM has proven successful in application, its downside lies in the high computational cost associated with Monte Carlo simulations in combination with FEM simulations of complex geometries.

In this work, we present a different approach that shifts most of the computational costs to offline costs by developing a stochastic FEM-postprocessor, which is based on the Poisson process model and the microstructural properties of nickel-based alloys.

The microstructure of conventionally cast metals is characterized by microscopic grains, where atoms arrange themselves in crystallographic lattices. In this lattice structure, one-dimensional lattice defects, known as dislocations, can propagate under cyclic loads. The activation energy required for these dislocations is minimized along specific slip systems—planes of densest packing and particular directions on these planes within the crystal's lattice structure [33]. This emphasizes the crucial influence of the local orientation of grain structures. As grain structures assume a random orientation during the solidification process in conventional casting, fatigue processes dependent on grain orientation become inherently stochastic [20, 22, 23, 32].

In [27], some authors proposed a model based on Schmid factors, which represent the maximum shear stress on any crystallographic slip system depending on its relative orientation to the stress tensor. This model has been subsequently extended to consider the local anisotropy of the metal's elastic constants [23, 20, 22, 21]. A model solely based on the probability of failure (PoF) of individual grains—defining a metallic structure as failing when the first grain cracks—tends to significantly underestimate the statistically observed scatter. The mathematical explanation for this discrepancy lies in the narrowing effect of extremal value distributions [17], while the physical rationale can be linked to the experimental definition of a technically relevant mesoscopic crack, extending over several microscopic grains.

Crack percolation modeling, as outlined in [7], is an integral part of any successful physics-based model accounting for the variability in the number of cycles until mesoscopic crack initiation. The model presented in [52] incorporates multi-grain crack percolation, and subsequent work in [50] refines and extensively tests this model against experimental data. However, these models do not account for interactions between an already formed crack in one grain and the subsequent influence on crack formation in neighboring grains as local loads are redistributed from the cracked grain to adjacent ones. In this work, there is an effort to model such interaction effects in a physics-based probabilistic model of LCF. For this purpose, FEM simulations model the influence of an intragranular crack in a crystal with a random orientation on the shear stress on randomly oriented slip systems on the other side of the grain boundary. In this way, data on the relative increase or decrease of these stresses are extracted. Using this data, a gradient boosting machine [38] is trained to predict these stress deviations concerning the stress state in the same grain with a non-cracked neighbor grain, based on the total of six Euler angles of both grains.

The probabilistic grain-microstructure model utilized in this work involves employing random Voronoi tessellations [69], where each Voronoi cell is assigned a crystal orientation. Our model starts with the single grain crack initiation model until the point where the first grain is cracked. Subsequently, the stresses of neighboring grains undergo correction based on the machine learning model, almost always resulting in an accelerated consumption of the remaining life. This introduces an epidemiological aspect to the model, where clusters of cracked grains propagate more rapidly compared to the percolation model, eventually reaching the size of a technically relevant crack. The concept of technically relevant cracks, as defined in [35], is based on multiaxial critical stress concentration factors.

To calibrate and validate the epidemiologic crack percolation model, we utilize experimental data obtained from LCF tests. The experimental results, provided by the RPTU Kaiserslautern-Landau, encompass a range of loading conditions, including both uniaxial and multiaxial scenarios.

For the transfer of the microstructural crack model to macroscopic components we use the Poisson point process modeling of LCF failure. Utilizing the epidemiological crack percolation model, cumulative hazard rates are computed based on loading conditions, loading cycles, and surface size. The independence of crack initiation probability in distant regions results in a linear dependence of these cumulative hazard rates on surface size. This linearity is utilized to define the local cumulative hazard rate as the slope of these hazards. Since performing Monte Carlo simulations of the percolation model for each quadrature point of the FE model is impractical in the application, a surrogate model based on a neural network [38] is employed, utilizing Latin hypercube sampling.

1.2 Outline

In Section 2, we provide a brief introduction to the microstructure of Nickel-base alloys. Additionally, we introduce essential continuum mechanical terms and outline the basics of LCF failure.

Within Section 3, we introduce the basic concepts of finite element simulations and the representation of orientations using elements of the special orthogonal group $SO(3)$. This section also includes a discussion on representing microscopic crack initiation as a Poisson point process.

The epidemiologic crack percolation model for uniaxial stress states based on random grain orientations is presented in Section 4. Here, we also introduce gradient boosting. The section concludes with the calibration on LCF tests and a comparison of the model with and without the infection function.

In Section 5, we present an approach for modeling grain orientations in the case of directed solidification. Using the epidemiological percolation model, we investigate the influence of directional solidification on LCF lifetime in Section 6.5. Furthermore, in Section 5, we explore the influence of transcrystalline crack initiation on the percolation model.

In Section 6, we extend the infection model beyond uniaxial stress states. The model is calibrated on uniaxial tests and validated with multiaxial test data.

In Section 7, we present the modeling of the FEM postprocessor. The FEM postprocessor is tested using the example of a blisk blade.

We end with some concluding remarks in Section 8,

2. Basics on Mechanics and Fatigue of Metals

The atomic arrangement of Materials determine their mechanical behavior. The focus of this section is to describe the microstructure of Nickel-base alloys and to introduce some basic concepts of continuum mechanics.

This section closely follows [33, 35] and [60].

2.1 Polycrystalline Structure of Metals

Due to their elastic and thermodynamic properties, metals are often used for the construction of mechanical components. In the solid state, the metal atoms tend to arrange as densely and regularly as possible, so the electrons can spread widely over the atoms. This leads to a highly ordered crystalline lattice structure. A crystal lattice is a three-dimensional arrangement of points that looks the same from every point considered. Each lattice can be defined by the atomic arrangements in a so-called unit cell. There are 14

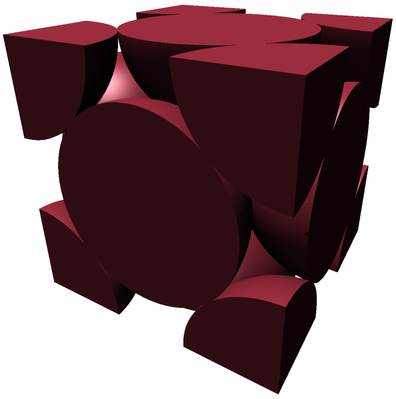

Figure 2.1: Unit cell of a face centered cubic crystal

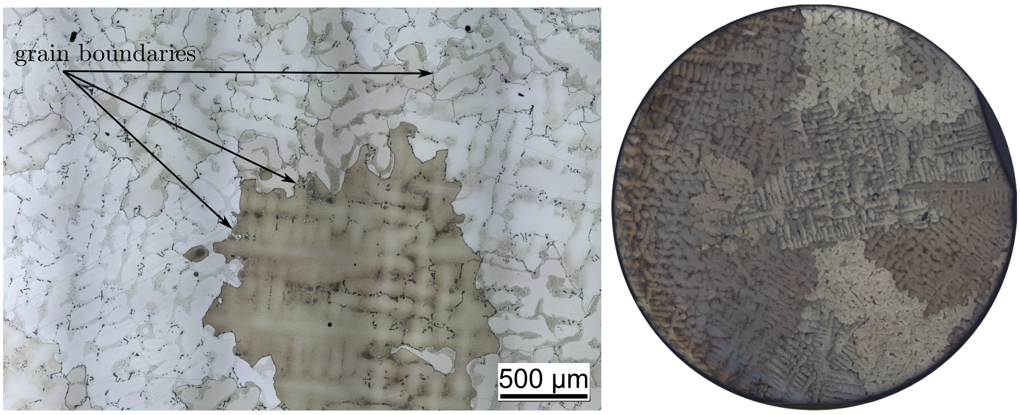

(a) Polycrystalline structure of a nickel-based alloy. The section is from a microscope image of a flat specimen.

(b) Grain structure in the cross-section of a round specimen

Figure 2.2: Grain structure of nickel base alloys. Reprinted with permission of the RPTU Kaiserslautern-Landau.

different ways to form such regular crystal lattices, these crystal types are also called Bravais lattices. These different lattices are distinguishable by their structure and symmetric properties. Since we are interested in nickel base alloys used in high temperature applications like gas turbine design, we focus on face-centered cubic (FCC) crystals. The unit cell of an FCC crystal has a quarter atom on each corner of the cube and in addition a half atom in each center of the six faces, see Figure 2.1.

The quarter atom means, that the unit cell shares the atom with the four adjacent unit cells, the half atom is shared with the adjacent cell respectively. The symmetry properties of the unit cell have an impact on the mechanical behavior of the material. When cast metal solidifies, this process starts in many places simultaneously. Therefore, atoms form a grain structure rather than a single crystal. The size of the grains is dependent on the parameters of the casting process, for example introducing additional materials into the metal or the temperature in the cooling phase. The grains differ in the orientation of the crystal lattice. In a coarse grain microstructure, which is shown in the microscopic pictures 2.2, the orientations of the grains have a significant impact on the elasticity and the fatigue properties of the metal.

Special alloys are used for applications under extreme conditions, such as

Element	Ni	Al	B	C	Co	Cr	Mo	Ti	W	Zr
Ma. - %	64.285	2.93	0.0151	0.17	9.48	14.04	4.03	5.08	4.02	0.011

(a) Material components of RENE80

Element	Ni	Al	C	Co	Cr	Hf	Mo	Nb	Si	Ta	Ti	W	Zr
Ma. - %	51.54	5.52	0.112	9.48	9.05	1.18	0.78	0.12	0.08	3.78	1.12	11.2	0.04

(b) Material components of Alloy247

Figure 2.3: Material proportions in the super alloys used in the experiments.

those found in gas turbines. In the experiments that we utilize to validate and fit the models developed here, two such super alloys are used. In addition to nickel, further elements are added to these alloys (table 2.3).

These additional elements allow the components manufactured with these materials to withstand high stresses even at high temperatures.

Microscope images (Figure 2.4) show that the various elements are distributed inhomogeneously in the material. The modeling approach we use in this work considers the material composition only indirectly via the material parameters.

2.2 Strain and Stress

As an outer force is applied to a metallic material, the force leads to a deformation. The deformation takes places because inner atoms of the material shift. There are two types of strain which we have to distinguish. At first we have a reversible deformation. When no more force is applied, the material returns to its original shape. The second type of deformation is irreversible, so-called plastic deformation. After the relief of the force, the material does not return to its original shape.

Metallic components used in gas turbines vary in size and usually have complex geometries, so that the stress varies over the geometry. To obtain material constants that describe the behavior of the material independently of its size and shape, we specify strain and stress locally in small volume units. The size scale we consider is larger than the spacing of individual

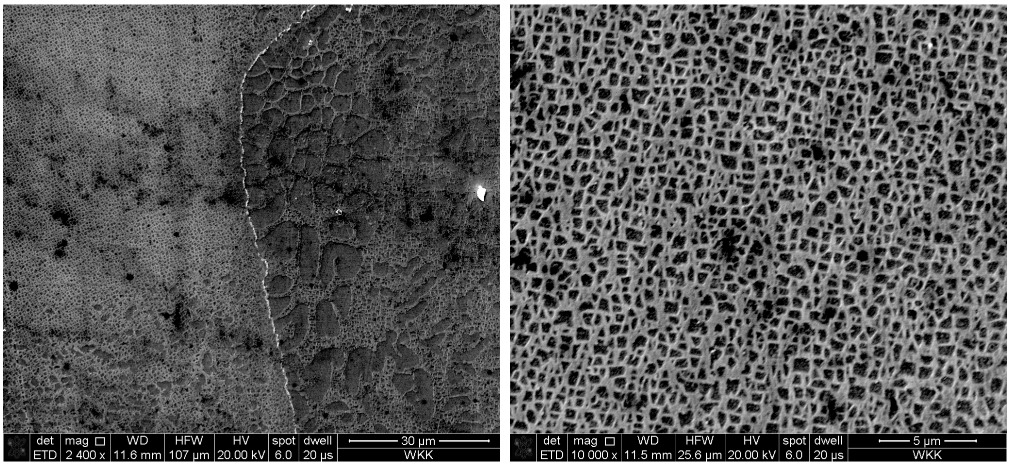

(a) Section with two grains. The bright line is a grain boundary.

(b) Close up of the microstructure.

Figure 2.4: Microstructure of Alloy247.

atoms, so that we can work within the framework of continuum mechanics.

Considering a Force F applied to an area A, the resulting stress is given by the Force divided by the area (Figure 2.5). There are two principal types of stress depending on whether the force is perpendicular or parallel to the surface. In the perpendicular case we have the so-called normal stress σ and in the parallel case the shear stress τ.

$$\sigma = \frac{F_\perp}{A}, \qquad \tau = \frac{F_\parallel}{A} \tag{2.1}$$

In other cases, where the force is neither totally perpendicular nor totally parallel, we can decompose the force in normal and shear stress. To describe the stress vector at a point, we intersect the volume in that point with a plane and take the lower limit of the average surface load

$$\lim_{A \to 0} \frac{\Delta F}{\Delta A}. \tag{2.2}$$

For the three-dimensional case we can build three differently orientated cross sections (Figure 2.6) and determine the resulting stress vectors.
A simple way is to use the three planes A_i perpendicular to the coordinate

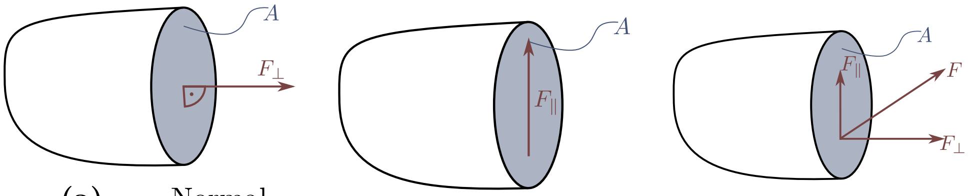

(a) Normal stress **(b)** Shear stress **(c)** Mixed stress

Figure 2.5: Different types of stress

axes x_i. The corresponding forces $F^{(i)}$can be decomposed into the individual components $F_j^{(i)}$. Therefor we can calculate the nine components $\sigma_{ij} = \frac{F_j^{(i)}}{A_i}$ and gain the stress tensor of second order:

$$\sigma = \begin{pmatrix} \sigma_{11} & \sigma_{12} & \sigma_{13} \\ \sigma_{21} & \sigma_{22} & \sigma_{23} \\ \sigma_{31} & \sigma_{32} & \sigma_{33} \end{pmatrix}. \tag{2.3}$$

Each row of the stress tensor describes the stress state acting on the cross-section plane were i stands for the normal of the plane. The entries with $i = j$ are the normal stresses acting in the direction of the normal of the plane. Those entries with $i \neq j$ are the shear stresses acting perpendicular to the normal. Since we assume a classical continuum, no momenta can be transferred in infinitesimally small elements. Therefore the strain tensor is symmetric

$$\sigma_{ij} = \sigma_{ji}, \quad \text{for} \quad i, j = 1, 2, 3, \tag{2.4}$$

and we have only 6 independent components. The stress tensor σ depends on the orientation of the plans. If we change the coordinate system, the stress state is the same but the stress tensor changes. For every stress state, there is a coordinate system, such that the stress tensor only has the three entries on the diagonal $\sigma_1, \sigma_2, \sigma_3$, the so-called principal stresses. The three planes that lead to the principal stresses are called principal planes. If the three components of the principal stress are sorted $|\sigma_I| \geq |\sigma_{II}| \geq |\sigma_{III}|$ we index them with roman numbers. The transformed stress Tensor in

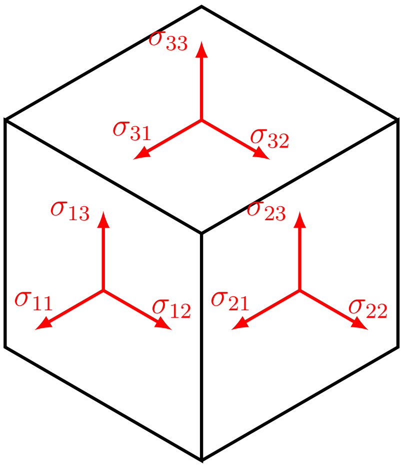

Figure 2.6: 3-dimensional stress tensor

principal axis form contains only normal stresses

$$\sigma = \begin{pmatrix} \sigma_I & 0 & 0 \\ 0 & \sigma_{II} & 0 \\ 0 & 0 & \sigma_{III} \end{pmatrix}. \tag{2.5}$$

The principal stress values are the eigenvalues of the stress tensor σ

$$\det(\sigma_{ij} - \delta_{ij}\sigma_e) = \det \begin{pmatrix} \sigma_{11} - \sigma_e & \sigma_{12} & \sigma_{13} \\ \sigma_{12} & \sigma_{22} - \sigma_e & \sigma_{23} \\ \sigma_{13} & \sigma_{23} & \sigma_{33} - \sigma_e \end{pmatrix} = 0, \quad e \in \{1,2,3\} \tag{2.6}$$

Therefore we gain the characteristic equation

$$\sigma_e^3 - I_1\sigma_e^2 - I_2\sigma_e - I_3 = 0. \tag{2.7}$$

with

$$\begin{aligned} I_1 &= \sigma_{11} + \sigma_{22} + \sigma_{33} \\ I_2 &= \sigma_{12}^2 + \sigma_{13}^2 + \sigma_{23}^2 - \sigma_{11}\sigma_{22} - \sigma_{11}\sigma_{33} - \sigma_{22}\sigma_{33} \\ I_3 &= \sigma_{11}\sigma_{22}\sigma_{33} + 2\sigma_{12}\sigma_{13}\sigma_{23} - \sigma_{12}^2\sigma_{33} - \sigma_{13}^2\sigma_{22} - \sigma_{23}^2\sigma_{11} = \det(\sigma). \end{aligned} \tag{2.8}$$

The coefficients in (2.8) are independent of the chosen coordinate system and are called the invariants of the stress state. In principal axis form the stress invariants simplify to

$$\begin{aligned}
I_1 &= \sigma_I + \sigma_{II} + \sigma_{III} \\
I_2 &= -\sigma_I \sigma_{II} - \sigma_I \sigma_{III} - \sigma_{II}\sigma_{III} \\
I_3 &= \sigma_I \sigma_{II} \sigma_{III}.
\end{aligned} \tag{2.9}$$

When deformation occurs, the points in the material shift. But as we move or rotate the whole material, the points in the material also move. Accordingly, we must distinguish between rigid body displacement or rigid body rotation and deformation. Under a deformation, the angles and distances between two points in the material change. Assume we have a mechanical component in form of a bounded region $\Omega \subseteq \mathbb{R}^3$ and its boundary $\partial\Omega$ and closure $\bar{\Omega}$. A force that acts on the component results in a deformation described by $u : \bar{\Omega} \to \mathbb{R}^3$, i.e. under the deformation the point x is moved to the new location $x + u(x)$. We assume that the component is fixed in some points, $u(x) = 0$ for $x \in \partial\Omega_D \subseteq \partial\Omega$. The strain tensor $\varepsilon : \Omega \to \mathbb{R}^{3\times 3}$ is given by

$$\varepsilon_{ij} = \frac{1}{2}\left(\frac{\partial u_i}{\partial x_j} + \frac{\partial u_j}{\partial x_i}\right), \tag{2.10}$$

it therefore holds that $\varepsilon_{ij} = \varepsilon_{ji}, i, j \in \{1, 2, 3\}$. The strain tensor thus has the same symmetry property as the stress tensor. We consider linear elastic material and small displacement, so it holds that the relation between strain and stress is given by Hooke's law:

$$\sigma_{ij} = C_{ijkl}\varepsilon_{kl} = \sum_{k=1}^{3}\sum_{l=1}^{3} C_{ijkl}\varepsilon_{kl}, \tag{2.11}$$

where $C \in \mathbb{R}^{3\times 3\times 3\times 3}$ is the so-called stiffness tensor. Due to the symmetry properties of the stress and strain tensor, this relationship can be expressed in a simplified matrix notation (Voigt notation). It holds that $C_{ijkl} = C_{jikl}$ and $C_{ijkl} = C_{ijlk}$ so the 81 entries of C reduce to 36 independent entries, and we can express the tensor C of rank for 4 as a quadratic matrix. Therefore, we change the indices $(\sigma_{ij}) \to (\sigma_\alpha)$, $(\varepsilon_{ij}) \to (\varepsilon_\alpha)$ and $(C_{ijkl}) \to (C_{\alpha\beta})$ where

$\alpha, \beta \in \{1, \dots, 6\}$, as follows

$$(\sigma_\alpha) = \begin{pmatrix} \sigma_{11} & \sigma_{22} & \sigma_{33} & \sigma_{23} & \sigma_{13} & \sigma_{12} \end{pmatrix} \tag{2.12}$$

$$(\varepsilon_\alpha) = \begin{pmatrix} \varepsilon_{11} & \varepsilon_{22} & \varepsilon_{33} & \gamma_{23} & \gamma_{13} & \gamma_{12} \end{pmatrix}, \qquad \text{with } \gamma_{ij} = 2\varepsilon_{ij}. \tag{2.13}$$

The stiffness tensor C has further symmetric properties, so it holds that $C_{\alpha\beta} = C_{\beta\alpha}$, and we get

$$\begin{pmatrix} \sigma_{11} \\ \sigma_{22} \\ \sigma_{33} \\ \sigma_{23} \\ \sigma_{13} \\ \sigma_{12} \end{pmatrix} = \begin{pmatrix} C_{11} & C_{12} & C_{13} & C_{14} & C_{15} & C_{16} \\ C_{12} & C_{22} & C_{23} & C_{24} & C_{25} & C_{26} \\ C_{13} & C_{23} & C_{33} & C_{34} & C_{35} & C_{36} \\ C_{14} & C_{24} & C_{34} & C_{44} & C_{45} & C_{46} \\ C_{15} & C_{25} & C_{35} & C_{45} & C_{55} & C_{56} \\ C_{16} & C_{26} & C_{36} & C_{46} & C_{56} & C_{66} \end{pmatrix} \begin{pmatrix} \varepsilon_{11} \\ \varepsilon_{22} \\ \varepsilon_{33} \\ \gamma_{23} \\ \gamma_{13} \\ \gamma_{12} \end{pmatrix}. \tag{2.14}$$

The Voigt notation is easy to handle but if we want to apply geometric transformations, such as rotations, we have to use the stiffness tensor of rank 4. The inverse of the stiffness tensor is called the compliance tensor S, and we have in Voigt notation:

$$\begin{pmatrix} \varepsilon_{11} \\ \varepsilon_{22} \\ \varepsilon_{33} \\ \gamma_{23} \\ \gamma_{13} \\ \gamma_{12} \end{pmatrix} = \begin{pmatrix} S_{11} & S_{12} & S_{13} & S_{14} & S_{15} & S_{16} \\ S_{12} & S_{22} & S_{23} & S_{24} & S_{25} & S_{26} \\ S_{13} & S_{23} & S_{33} & S_{34} & S_{35} & S_{36} \\ S_{14} & S_{24} & S_{34} & S_{44} & S_{45} & S_{46} \\ S_{15} & S_{25} & S_{35} & S_{45} & S_{55} & S_{56} \\ S_{16} & S_{26} & S_{36} & S_{46} & S_{56} & S_{66} \end{pmatrix} \begin{pmatrix} \sigma_{11} \\ \sigma_{22} \\ \sigma_{33} \\ \sigma_{23} \\ \sigma_{13} \\ \sigma_{12} \end{pmatrix}. \tag{2.15}$$

2.2.1 Isotropic and Anisotropic material

Due to the arrangement of the atoms in crystal lattices, metals show further symmetric properties. If the relationship between strain and stress is independent of the orientation of the material, the stiffness tensor must also be invariant under rotations. Such a material is called isotropic. The requirement of invariance under rotations reduce the stiffness tensor to the simplified form

$$C = \begin{pmatrix} C_{11} & C_{12} & C_{12} & 0 & 0 & 0 \\ C_{12} & C_{11} & C_{12} & 0 & 0 & 0 \\ C_{12} & C_{12} & C_{11} & 0 & 0 & 0 \\ 0 & 0 & 0 & C_{44} & 0 & 0 \\ 0 & 0 & 0 & 0 & C_{44} & 0 \\ 0 & 0 & 0 & 0 & 0 & C_{44} \end{pmatrix}, \qquad \text{with } C_{44} = \frac{C_{11} - C_{12}}{2}. \tag{2.16}$$

Often the material dependent parameters are expressed via Young's modulus E, the Poisson's ratio ν and the shear modulus G:

$$\begin{aligned} C_{11} &= \frac{E(1-\nu)}{(1+\nu)(1-2\nu)} \\ C_{22} &= \frac{E\nu}{(1+\nu)(1-2\nu)} \\ C_{44} = G &= \frac{E}{2(1+\nu)}. \end{aligned} \tag{2.17}$$

Due to the lattice structure, the mechanical properties of nickel crystal depends on the direction a force is applied. But if the scale of the material is large in respect to the size of a single grain and considering that the orientations of the grains are uniformly distributed, these anisotropic effects are averaged out by homogenization.
However, when considering volumes containing only a few grains or even a single crystal, the anisotropic material behavior must be taken into account. Since the crystal structure is responsible for the anisotropic behavior and nickel forms FCC crystals, the stiffness and compliance tensor have the same symmetries as a cubic unit cell.

For the description of the rotation axes we use Miller indices. Miller indices are frequently used to characterize directions and planes in crystallographic lattices. Here, we give just a brief overview how directions are denoted.

For the notation with Miller indices we choose a coordinate system with a lattices point as the origin and the lattice edges as the coordinate axes. The axes are scaled such that the next lattice point from the origin has the

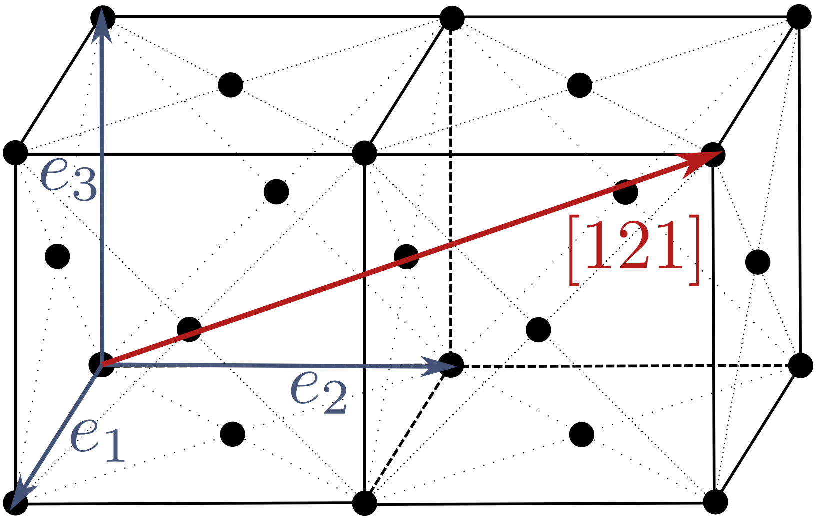

Figure 2.7: Example for a direction in an FCC crystal lattice notated with Miller indices.

value 1. In a cubic lattice this leads to a Cartesian coordinate system.

A direction in the crystallographic lattice is given by the origin and an additional lattice point. The direction in Miller indices $[hkl]$ is then given by the coordinates of the second point multiplied by a $q \in \mathbb{Q}$, such that $j, k, l \in \mathbb{Z}$ with the greatest comment divisor 1, as illustrated in Figure 2.7. Negative values are represented with a bar on top.

The notation of a direction with angled brackets $\langle hkl \rangle$ instead of square brackets stands for all crystallographic equivalent directions rather. Two directions are crystallographic equivalent if they are mapped onto one another under the action of the symmetry group of the crystallographic lattice.

With this notation, the edges of a cubic unit cell are given by $\langle 100 \rangle$, the surface diagonals by $\langle 110 \rangle$ and the volume diagonals by $\langle 111 \rangle$.

The rotational symmetries of a cubic crystal are

$$\begin{aligned} &n \cdot \frac{\pi}{2} \text{ around } \langle 100 \rangle, \\ &n \cdot \frac{2\pi}{3} \text{ around } \langle 111 \rangle \text{ and} \\ &n \cdot \pi \text{ around } \langle 110 \rangle. \end{aligned} \tag{2.18}$$

With these symmetries, the compliance matrix for an FCC material with unit cell edges parallel to the coordinate axis has to be of the form:

$$S = \begin{pmatrix} S_{11} & S_{12} & S_{12} & 0 & 0 & 0 \\ S_{12} & S_{11} & S_{12} & 0 & 0 & 0 \\ S_{12} & S_{12} & S_{11} & 0 & 0 & 0 \\ 0 & 0 & 0 & S_{44} & 0 & 0 \\ 0 & 0 & 0 & 0 & S_{44} & 0 \\ 0 & 0 & 0 & 0 & 0 & S_{44} \end{pmatrix}. \tag{2.19}$$

If the edges of the crystal cell are not parallel to the coordinate axis the compliance tensor can be calculated with

$$S_{ijkl}(U) = \sum_{p,q,r,s} U_{ip} U_{jq} U_{kr} U_{ls} S_{pqrs}, \tag{2.20}$$

where U is the corresponding rotation matrix. As the material behavior is direction-dependent, the young's modulus is given with respect to a direction E_i. Accordingly, two directions must be specified for poisson's ratio ν_{ij} and shear modulus G_{ij}. For the entries in the compliance matrix in equation (2.19) we have the following relations:

$$\begin{aligned} S_{11} &= \frac{1}{E_{\langle 100 \rangle}}, \\ S_{22} &= -\frac{\nu_{\langle 010 \rangle \langle 001 \rangle}}{E_{\langle 100 \rangle}} = -\frac{\nu_{\langle 001 \rangle \langle 100 \rangle}}{E_{\langle 100 \rangle}}, \\ S_{44} &= \frac{1}{G_{\langle 010 \rangle \langle 100 \rangle}} = \frac{1}{G_{\langle 001 \rangle \langle 100 \rangle}}. \end{aligned} \tag{2.21}$$

The stiffness tensor is of the same form as the compliance tensor in equation (2.19). In comparison to the isotropic case, it does not apply that C_{44} depends on C_{11} and C_{12}. For the conversion from compliance to stiffness matrix the following relations apply

$$\begin{aligned} C_{11} &= \frac{S_{11} + S_{12}}{(S_{11} - S_{12})(S_{11} + 2S_{12})}, & S_{11} &= \frac{C_{11} + C_{12}}{(C_{11} - C_{12})(C_{11} + 2C_{12})}, \\ C_{12} &= -\frac{S_{12}}{(S_{11} - S_{12})(S_{11} + 2S_{12})}, & S_{12} &= -\frac{C_{12}}{(C_{11} - C_{12})(C_{11} + 2C_{12})}, \\ C_{44} &= \frac{1}{S_{44}}, & S_{44} &= \frac{1}{C_{44}}. \end{aligned} \tag{2.22}$$

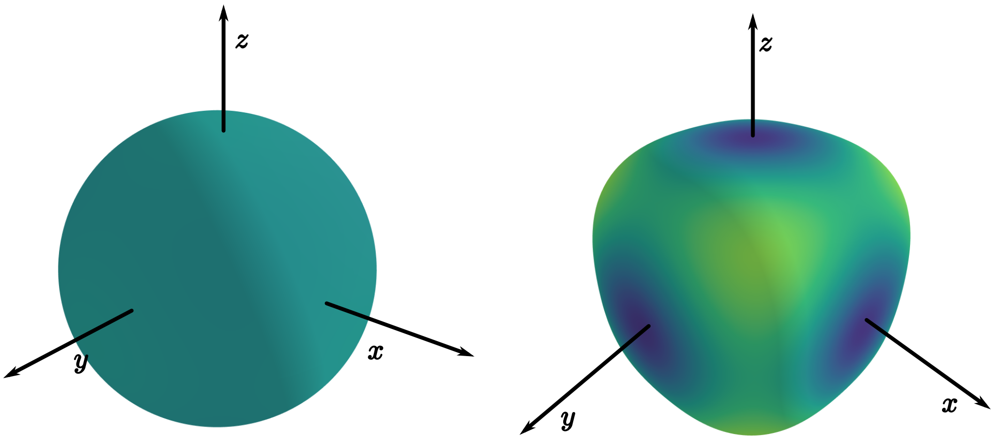

(a) Wolfram: $C_{11} = 501\text{GPa}$, $C_{12} = 198\text{GPa}$, $C_{44} = 151\text{GPa}$, Isotropic with $a_r = 1$

(b) Aluminium: $C_{11} = 108\text{GPa}$, $C_{12} = 61\text{GPa}$, $C_{44} = 29\text{GPa}$, Anisotropic with $a_r = 1.23$

Figure 2.8: Direction dependent Young modulus for different materials

This also holds for the isotropic case. The anisotropy of cubic material can be measured with Zener ratio [73] a_r which is defined by

$$a_r := \frac{2C_{44}}{C_{11} - C_{12}}. \tag{2.23}$$

Isotropic material has a Zener ratio of 1, if $a_r < 1$ or $a_r > 1$ the material is anisotropic. The direction dependent young modulus $E_{[hkl]}$ can be calculated with

$$\frac{1}{E_{[hkl]}} = S_{11} - \left[2(S_{11} - S_{12}) - S_{44}\right] r_{[hkl]} \tag{2.24}$$

were $r_{[hkl]}$ is a direction dependent factor, which is given by

$$r_{[hkl]} = \alpha^2\beta^2 + \alpha^2\gamma^2 + \beta^2\gamma^2. \tag{2.25}$$

In Figure 2.8 the direction dependent young modulus is shown for two different materials. On the left (Figure 2.8a) for wolfram, which is isotropic, so the E-modulus forms a sphere. The right figure in comparison shows aluminum, which is anisotropic. Here the direction dependence is easy to see.

The values α, β, γ are the cosines of the angles between the direction $[hkl]$

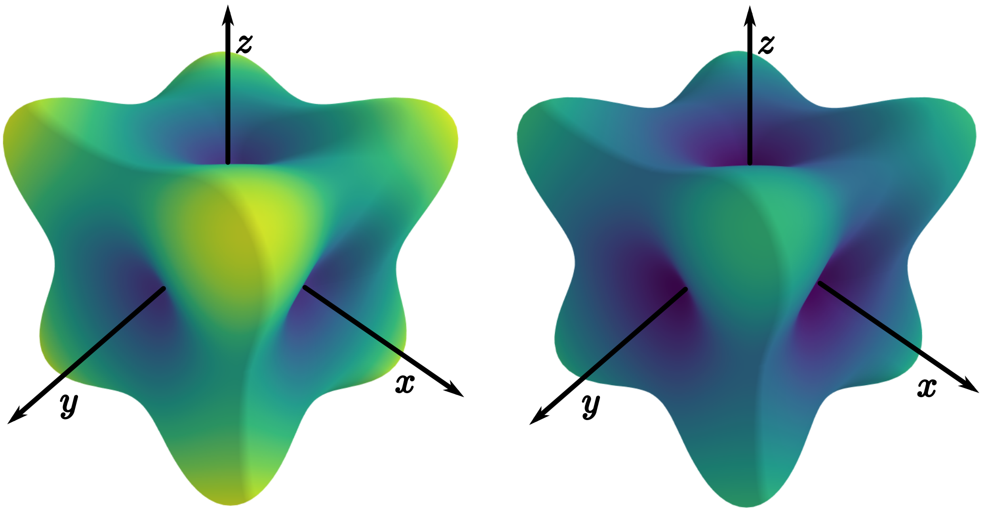

(a) INC738 at 25°C: $C_{11} = 225$GPa, $C_{12} = 191$GPa, $C_{44} = 127$GPa, Isotropic with $a_r = 2.8$

(b) INC738 at 850°C: $C_{11} = 226$GPa, $C_{12} = 161$GPa, $C_{44} = 99$ GPa, Isotropic with $a_r = 3.1$

Figure 2.9: Temperature dependent Young modulus for INC738

and the coordinate axis:

$$\begin{aligned}\alpha &= \cos([hkl],[100])\\ \beta &= \cos([hkl],[010])\\ \gamma &= \cos([hkl],[001])\end{aligned} \tag{2.26}$$

The material parameters depend on temperature, which can be seen in Figure 2.9 for the material INC738, which is a typical material for gas turbine components.

2.3 Plastic deformation

Plastic deformation is irreversible, so after the stress applied to the material is relieved, the arrangement of the atoms have changed permanently. In a perfect single crystal under a high enough shear load, i.e. if plastic deformation occurs, whole atomic layers slide off against each other.

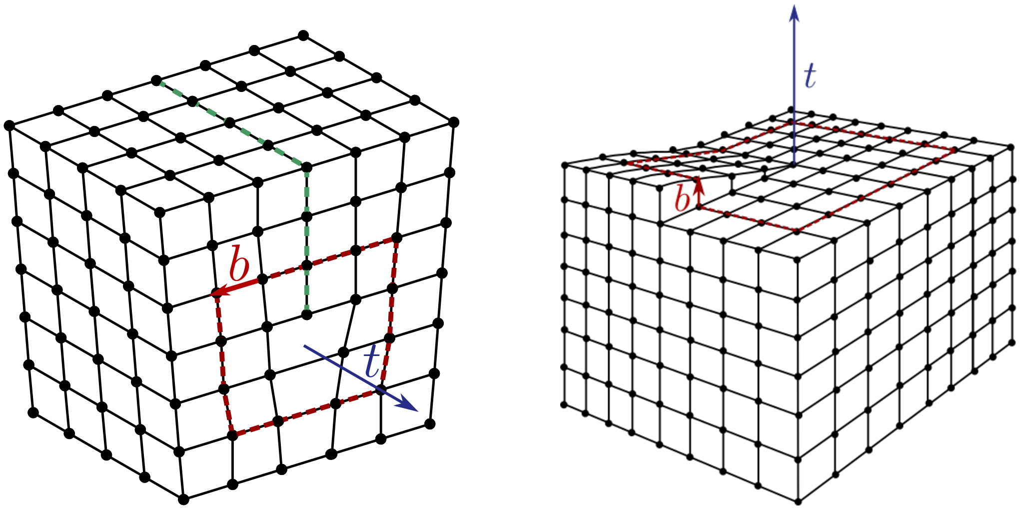

(a) Edge dislocation with Burgers vector and line vector. The additional half plane of atoms is marked green.

(b) Screw dislocation with Burgers vector and line vector. The additional half plane of atoms is marked green.

Figure 2.10: Basic types of dislocations

2.3.1 Dislocations

In cast metal the crystal lattice is not perfect. There are often defects in the lattice structures. The defects in the crystal lattice can be categorized into different types distinguished by their dimensionality. 0-dimensional errors, so-called point defects, occur if there is an additional atom in the lattice (interstitial defect) or if an atom of the lattice is missing (vacancy defect). Grain boundaries and phase boundaries are 2-dimensional planar defects. The defects we focus one are 1-dimensional line defects, called dislocations.

Dislocations are an additional half plane of atoms in the crystal lattice. They can be described by two vectors, the line vector t in the direction of the dislocation line and the Burgers vector b. The Burgers vector can be determined by drawing a path along the grid edges around the dislocation line. In a perfect lattice, the same number of steps are required in all crystallographic directions to close the circuit. Due to the effect of a dislocation the path around such a lattice defect does not end at the starting point. The additional steps along the lattice edges form the Burgers vector.

The two basic types of dislocations can be distinguished by the direction of

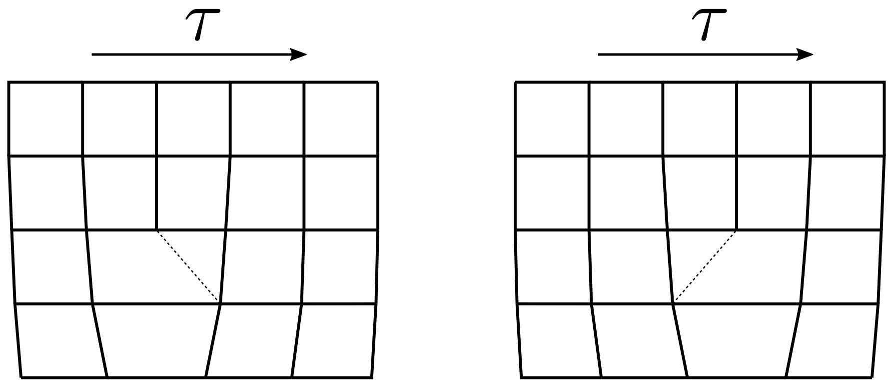

(a) Edge dislocations under shear stress

(b) The atomic binding at the dislocation line has flipped.

Figure 2.11: Movemt of a dislocation

the Burgers vector. If the Burgers vector is perpendicular to the dislocation line, it is called an edge dislocation, and if the Burgers vector is oriented parallel to the dislocation line, it is a screw dislocation. Normally, dislocation lines do not follow straight lines. They follow a complex path through the crystal, therefore the direction of the line vector depends on the location in the crystal. The Burgers vector of a dislocation, on the other hand, is independent of the location. As the angle between Burgers vector and line vector is dependent on the location, the characteristic of the dislocation changes along the dislocation line. Therefore, there are parts were the same dislocation line has a screw or an edge characteristic, or a mixture of both.

Around the dislocation line, the crystal lattice is distored and consequently there are atomic bonds that are shorter or longer than in a perfect lattice structure. Under a sufficient strong shear stress, the bonds at the dislocation line can flip and the dislocation moves through the crystal. Within the process the atomic structure changes permanently, as illustrated in Figure 2.11. This mechanism repeats itself until the dislocation reaches the surface of the crystal. The move of a dislocation requires less energy than a movement of a whole atomic layer. Therefore, plasticity sets on way before force are reached that could dissolve the atomic bonds spontaneously.

The critical shear stress, which is required to start this process, is denoted by τ_{crit}, see also Section 2.3.3 below.

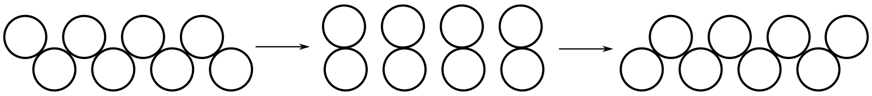

(a) Slipping in loosely packed direction

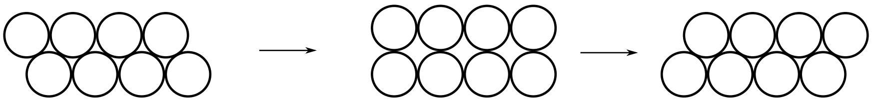

(b) Slipping in densely packed direction

Figure 2.12: Slipping of an atomic layer

2.3.2 Slip Systems

Mathematically, the motion of the dislocations can be described by a plane in which the atomic layers move against each other and the direction. The more densely packed the atoms are in the sliding direction, the less force is necessary to cause the sliding. This can be illustrated by simplifying the atoms to spheres and letting two atomic layers slide against each other. When the spheres are densely packed, they need to be lifted less than when they are loosely packed (Figure 2.12). Therefore there are preferred directions in a crystal lattice in which the dislocations move. The directions depend on the lattice structure and can be determined from the unit cell of the crystal. An FCC crystal has the densest possible sphere packing. One of the planes that contains the densest packing is shown in Figure 2.13a, the corresponding direction of the plane are the edges of the triangle. There are four independent planes with the densest packing, see Figure 2.13b. The 4 planes, each with 3 directions along the edges of the tetrahedron, give a total of 12 independent slip systems.
Crystals with different lattice structures have different slip systems, e.g., a body-centered cubic crystal (BCC) does not have a plane with the densest possible sphere packing. Instead, there are 6 planes that are most densely packed, each having 2 slip directions. Furthermore, there are 36 more planes that are almost similarly densely packed, each with one direction. So in a BCC crystal there are 48 possible slip systems in which dislocations can move.

As the material that we are interested in is a nickel-base alloy, we focus on FCC crystal structures at this point.

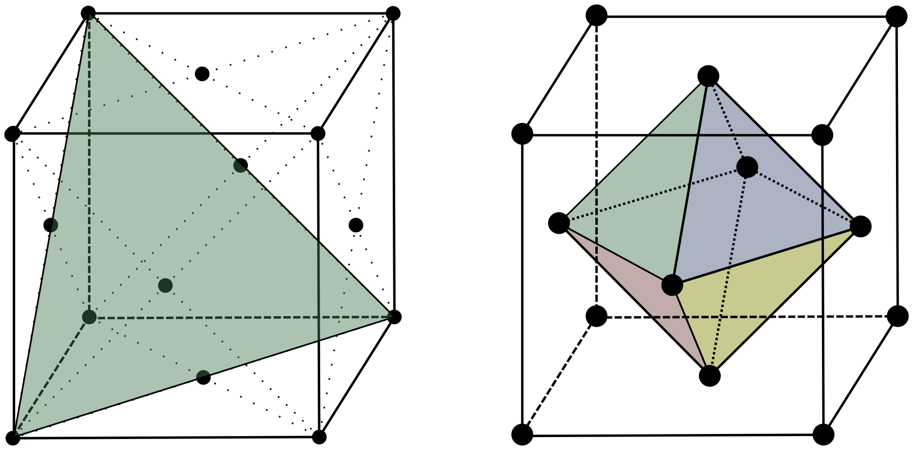

(a) One of the four slip planes, the three edges of the triangle are the corresponding directions.

(b) The slip systems of an FCC crystal, the four planes are colored, the edges of the triangles are the corresponding direction.

Figure 2.13: Slipsystems in a face centered cubic crystal

2.3.3 Yield criterion

Standardized tensile tests are performed to investigate the transition from elastic deformation to plastic deformation. In these tests, a specimen is clamped in a fixture and uni-axially strained at a constant rate. The force F and the length change Δl of the specimen is measured all the time. With the initial cross-section A_{init}, the stress is given by $\sigma = F/A_{\text{init}}$ and the strain can be determined by the ratio of the change in length and the initial length of the specimen $\varepsilon = \Delta l/l$.

The relation between strain and stress from the tensile tests can be visualized with a so-called strain-stress diagram (Figure 2.14). In general, strain-stress diagrams have the following form. For small strain, the stress increases linearly, the material shows linear elastic behavior. Therefore, Hooke's law (equation 2.11) can be applied to describe the relation between strain and stress. As the yield point R_p is reached, plastic deformation starts. Stress increases further with strain until the maximum stress is reached at the so-called tensile strength R_m. If strain increases even more, the measured stress reduces until fracture. This reduction in stress is due to an effect called necking, where the cross-section of the speciem reduces locally. Therefore, the stress in the necking zone is higher than measured.

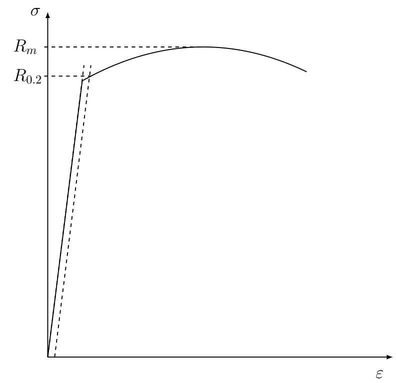

Figure 2.14: Strain-stress diagram.

The strain level, where the transition from elastic to plastic deformation starts, is not clearly defined. A common way to fix it, is the yield point $R_{p0.2}$. This is the stress which leads to a plastic deformation of 0.2% after the force is relieved. We can determine $R_{p0.2}$ from the strain-stress diagram by drawing a parallel line to the elastic part of the curve which intersects the $x-$axis at 0.2%, as illustrated in Figure 2.14. The intersection with the strain-stress curve is at the stress level $R_{p0.2}$.
As Hooke's law only hold for small strains an approximation for the strain-stress diagrams needs a further term. A common way for the approximation is the Ramberg-Osgood equation.

Definition 2.1 (Ramberg-Osgood Equation). *Let E be the young modulus, K the strength coefficient and n the strain hardening exponent. The relation between strain- and stress amplitude in the elastic-plastic case can be approximated by the Ramberg-Osgood (RO) equation:*

$$\varepsilon_a = RO(\sigma_a) = \frac{\sigma_a}{E} + \left(\frac{\sigma_a}{K}\right)^{1/n}. \tag{2.27}$$

The three coefficients are material dependent.

The first term of the RO equation is just Hooke's law in one dimension and describes the linear elastic part of the deformation. The second part is gained from Hollomon's equation: $\sigma = K\varepsilon_p^n$ which gives the stress from a plastic deformation.

2.3.4 Multiaxial yield criteria

As under Multiaxial loading states the stress tensor contains more than one entry that is not zero, the yield criterion becomes more complex. Generally yield criteria can be expressed with an equivalent stress σ_v. If σ_v reaches a critical value σ_{crit}, plastic deformation occurs:

$$\sigma_v(\sigma_{ij}) := \sigma_v(\sigma_{11}, \sigma_{22}, \sigma_{33}, \sigma_{12}, \sigma_{13}, \sigma_{23}) = \sigma_{\text{crit}}. \tag{2.28}$$

We use here a yield criterion formulated slightly differently:

$$f(\sigma_{ij}) = \sigma_v(\sigma_{ij}) - \sigma_{\text{crit}} = 0. \tag{2.29}$$

The yield criterion for the uni-axial case, just with stress $\sigma_{11} = \sigma_I$, from Section 2.3.3 then becomes:

$$f(\sigma_{11}) = \sigma_{11} - R_p = 0. \tag{2.30}$$

Experiments show that hydrostatic stress, i.e. stress that only contains normal stresses $\sigma_{11} = \sigma_{22} = \sigma_{33}$, has no influence on the plasticization of metals. In Section 2.4 below, we show that this effect is due to fact that the normal and the direction of a slip system are perpendicular to each other.

The hydrostatic part of an arbitrary stress state can be calculated by

$$\sigma_h = \frac{1}{3}\left(\sigma_{11} + \sigma_{22} + \sigma_{33}\right). \tag{2.31}$$

For yield criteria, we can use the so-called stress deviator σ', which is the stress tensor without the hydrostatic stress:

$$\sigma' = \begin{pmatrix} \sigma'_{11} & \sigma'_{12} & \sigma'_{13} \\ \sigma'_{21} & \sigma'_{22} & \sigma'_{23} \\ \sigma'_{31} & \sigma'_{32} & \sigma'_{33} \end{pmatrix} = \begin{pmatrix} \sigma_{11} & \sigma_{12} & \sigma_{13} \\ \sigma_{21} & \sigma_{22} & \sigma_{23} \\ \sigma_{31} & \sigma_{32} & \sigma_{33} \end{pmatrix} - \begin{pmatrix} \sigma_h & 0 & 0 \\ 0 & \sigma_h & 0 \\ 0 & 0 & \sigma_h \end{pmatrix}. \tag{2.32}$$

The three invariants of a stress state I_1, I_2, I_3 (see equations 2.8 and 2.9) can be calculated from the stress deviator as well. In order to avoid confusion, they are called I'_1, I'_2, I'_3. So by plugging in σ' in equation 2.8 the first invariant becomes:

$$I_1' = (\sigma_{11} - \sigma_h) + (\sigma_{22} - \sigma_h) + (\sigma_{33} - \sigma_h) = 0. \tag{2.33}$$

Notice, that

$$\begin{aligned}
&(\sigma_{11} - \sigma_h)(\sigma_{22} - \sigma_h) + (\sigma_{11} - \sigma_h)(\sigma_{33} - \sigma_h) + (\sigma_{22} - \sigma_h)(\sigma_{33} - \sigma_h) \\
&\quad = \sigma_{11}\sigma_{22} + \sigma_{11}\sigma_{33} + \sigma_{22}\sigma_{33} - 2\sigma_h(\sigma_{11} + \sigma_{22} + \sigma_{33}) + 3\sigma_h^2 \\
&\quad = \sigma_{11}\sigma_{22} + \sigma_{11}\sigma_{33} + \sigma_{22}\sigma_{33} - 3\sigma_h^2 \\
&\quad = \sigma_{11}\sigma_{22} + \sigma_{11}\sigma_{33} + \sigma_{22}\sigma_{33} - \\
&\qquad\quad \frac{1}{3}(\sigma_{11}^2 + \sigma_{22}^2 + \sigma_{33}^2 + 2\sigma_{11}\sigma_{22} + 2\sigma_{11}\sigma_{33} + 2\sigma_{22}\sigma_{33}) \\
&\quad = \frac{1}{3}\left(\sigma_{11}\sigma_{22} + \sigma_{11}\sigma_{33} + \sigma_{22}\sigma_{33} - \sigma_{11}^2 - \sigma_{22}^2 - \sigma_{33}^2\right).
\end{aligned} \tag{2.34}$$

With equation 2.34, we obtain for I_2', as we plug in the stress deviator,

$$\begin{aligned}
I_2' &= \sigma_{12}^2 + \sigma_{13}^2 + \sigma_{23}^2 - (\sigma_{11} - \sigma_h)(\sigma_{22} - \sigma_h) - \\
&\qquad (\sigma_{11} - \sigma_h)(\sigma_{33} - \sigma_h) - (\sigma_{22} - \sigma_h)(\sigma_{33} - \sigma_h) \\
&= \frac{1}{3}\left(\sigma_{11}^2 + \sigma_{22}^2 + \sigma_{33}^2 - \sigma_{11}\sigma_{22} - \sigma_{11}\sigma_{33} - \sigma_{22}\sigma_{33}\right) + \\
&\qquad \sigma_{12}^2 + \sigma_{13}^2 + \sigma_{23}^2
\end{aligned} \tag{2.35}$$

Under the use of the principal axis form, I_2' reduces with equation 2.34 to

$$\begin{aligned}
I_2' &= \frac{1}{3}\left(\sigma_I\sigma_{II} + \sigma_I\sigma_{III} + \sigma_{II}\sigma_{III} - \sigma_I^2 - \sigma_{II}^2 - \sigma_{III}^2\right) \\
&= \frac{1}{6}\left[(\sigma_I - \sigma_{II})^2 + (\sigma_I - \sigma_{III})^2 + (\sigma_{II} - \sigma_{III})^2\right]
\end{aligned} \tag{2.36}$$

A commonly used yield criterion is the von Mises shape modification hypothesis. This criterion uses the second stress invariant I_2' as the equivalent stress

$$f(I_2') = I_2' - k_f^2 = 0, \tag{2.37}$$

where k_f is a material dependent constant. Therefore the von Mises equiva-

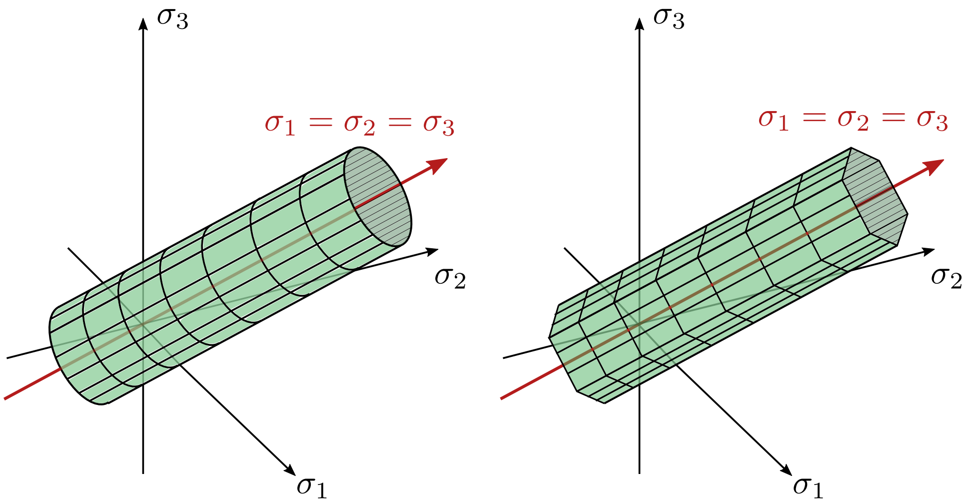

(a) Von Mises yield criterion, the yield surface is a cylinder around the hydrostatic stress

(b) Tresca's yield criterion, hexagonal yield surface around the hydrostatic stress

Figure 2.15: Yield surface for different yield criteria

lent stress is given by

$$\sigma_{vM} = \sqrt{\frac{1}{3}\left(\sigma_{11}^2 + \sigma_{22}^2 + \sigma_{33}^2 - \sigma_{11}\sigma_{22} - \sigma_{11}\sigma_{33} - \sigma_{22}\sigma_{33}\right) + \sigma_{12}^2 + \sigma_{13}^2 + \sigma_{23}^2}. \tag{2.38}$$

If we use stress in principal axis form (2.38) becomes

$$\sigma_{vM} = \sqrt{\frac{1}{6}\left[(\sigma_I - \sigma_{II})^2 + (\sigma_I - \sigma_{III})^2 + (\sigma_{II} - \sigma_{III})^2\right]}. \tag{2.39}$$

Utilizing the yield point R_p and a uniaxial stress, i.e. $\sigma_I = R_p, \sigma_{II} = 0$, $\sigma_{III} = 0$ we can express k_f in the von Mises yield criterion

$$k_f^2 = \sqrt{\frac{1}{6}\left[(\sigma_I - \sigma_{II})^2 + (\sigma_I - \sigma_{III})^2 + (\sigma_{II} - \sigma_{III})^2\right]}, \tag{2.40}$$

in terms of R_p, with

$$k_f = \sqrt{\frac{2}{3}} R_p. \tag{2.41}$$

If we consider the von Mises yield criterion in the principal axis space, it is the mantle surface of a cylinder around the hydrostatic stress with radius $\sqrt{\frac{2}{3}} R_p$ as shown in Figure 2.15a.

The other criterion frequently used in material science is the Tresca yield

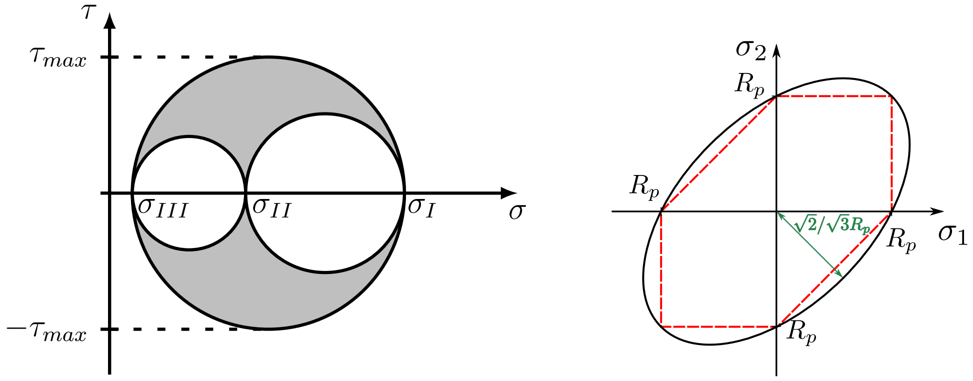

(a) Mohr's circle

(b) Von Mises yield criterion (black) and Tresca yield criterion (red) with $\sigma_3 = 0$.

Figure 2.16: Mohr's circel and comparison of both yield criteria.

criterion. It is based on the assumption that the maximum shear stress τ_{max} is responsible for the sliding of the atomic layer against each other.

One way to determine the maximum shear stress that can occur in a material is to use a Mohr's circle. For this purpose, we draw three circles in a coordinate system with the normal stress on the abscissa and the shear stress on the ordinate. Each of the circles is bounded by two of the principal stresses. The gray area in Figure 2.16a represents the possible stress states in the considered point. It is easy to see that τ_{max} is the radius of the circle bounded by σ_I and σ_{III}. Therefore, the maximum shear stress is independent of σ_{II} and can be determined by

$$\tau_{\text{max}} = \frac{\sigma_I - \sigma_{III}}{2}. \tag{2.42}$$

Plastic deformation in the material starts if the maximum shear stress reaches a critical value τ_{tr}. The Tresca yield criterion can be expressed as

$$f(\sigma_I, \sigma_{II}) = \frac{\sigma_I - \sigma_{III}}{2} - \tau_{\text{crit}} = 0. \tag{2.43}$$

With the tensile experiments from Section 2.3.3 we have $\sigma_I = R_p$ and $\sigma_{II} = \sigma_{III}$, thus $\tau_{tr} = R_p/2$ and the criterion becomes

$$\sigma_I - \sigma_{III} = R_p. \tag{2.44}$$

In principal axis space, the Tresca yield criterion is a six-sided prism around the hydrostatic stress (Figure 2.15b).

In Figure 2.16b, both yield criteria are displayed for $\sigma_3 = 0$. The maximum difference between both criteria is 15.5%.

2.4 Schmid factors

As mentioned in Section 2.3.2, in anisotropic materials plastic deformation move through the crystal along the slip systems. This process starts when the shear stress in a slip system reaches a critical value τ_{crit}. The shear stress in a slipsystem usually differs from the global shear stress. Under uniaxial stress ($\sigma_2 = \sigma_3 = 0$) the shear stress in a slipsystem of FCC crystal can be determined by the following approach.

For $i \in \{1, \dots, 4\}, j \in \{1, 2, 3\}$ n_i be the normal vector of the slipplane and s_{ij} the slipdirection (see Figure 2.17). The cross-sectional area of the specimen is donated with A_0 and the Force with F. In order to gain the force F_{ij} in the direction of the slip system, we need to project F on s_{ij} by

$$F_{ij} = F \cos(\kappa_{ij}), \tag{2.45}$$

where κ_{ij} is the angle between the F and s_{ij}. Let γ_i be the angle between the n_i and F, then the area of the slip plane inside the specimen A_i is given by

$$A_i = \frac{A_0}{\cos(\gamma_i)}. \tag{2.46}$$

Thus, with $\tau_{ij} = F_{ij}/A_i$,$\sigma_1 = F/A_0$ and both equations (2.45),(2.46) it follows that:

$$\tau_{ij} = \sigma_1 \cos(\kappa_{ij}) \cos(\gamma_i). \tag{2.47}$$

The relation between shear stress and the applied stress is the so-called Schmid factor:

$$m_{ij} := \frac{\tau_{ij}}{\sigma_1} = \cos(\kappa_{ij}) \cos(\gamma_i). \tag{2.48}$$

The vectors s_{ij} and n_i are perpendicular to each other, so the Schmid factor

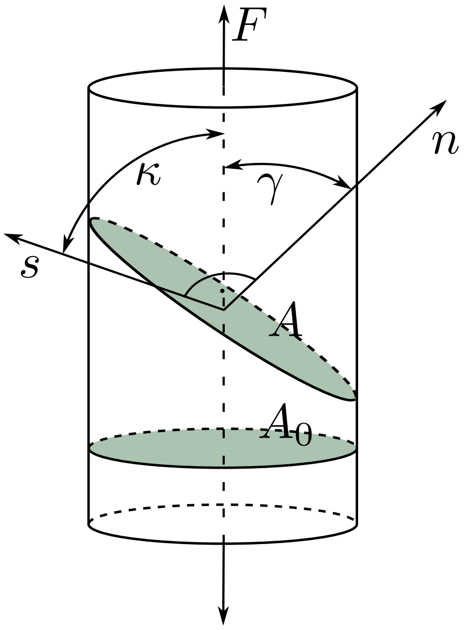

Figure 2.17: Schematic illustration of the orientation of a slip plane in a cylindrical specimen.

can be at most 0.5. This also becomes clear if we consider a Mohr's circle with $\sigma_I = \sigma_1$ and $\sigma_{II} = \sigma_{III} = 0$. It is just one circle with radius $\sigma_1/2$ and therefore is $\tau_{\max} = \sigma_1/2$. An alternative way to gain the shear stress acting in a slip system is to use the normalized direction and normal vector. We can project

$$\sigma = \begin{pmatrix} \sigma_1 & 0 & 0 \\ 0 & 0 & 0 \\ 0 & 0 & 0 \end{pmatrix} \tag{2.49}$$

directly via

$$\tau_{ij} = n_i \cdot \sigma \cdot s_{ij}. \tag{2.50}$$

The slip system which reaches the critical shear stress τ_{crit} first gets activated, and the dislocations start to move through the crystal. Therefore, we can take the maximum over all slip systems in the crystal

$$\tau = \max_{ij} |\tau_{ij}|, \tag{2.51}$$

to compare it with the critical value τ_{crit}.

If we consider a multiaxial stress state, we can use a slightly different definition of the Schmid factor introduced in [27, 52]. Equation (2.50) holds for a multiaxial stress

$$\sigma = \begin{pmatrix} \sigma_{11} & \sigma_{12} & \sigma_{13} \\ \sigma_{12} & \sigma_{22} & \sigma_{23} \\ \sigma_{13} & \sigma_{23} & \sigma_{33} \end{pmatrix} \tag{2.52}$$

as well. We define the alternative Schmid factor as the ratio of shear stress and the applied stress

$$m_{ij} := \frac{\tau_{ij}}{\sqrt{3/2} \cdot \sigma_{vM}}. \tag{2.53}$$

With equation (2.50), it is straight forward that the hydrostatic part of the stress tensor σ is negligible.

$$\begin{aligned} \tau_{ij} &= n_i \cdot \sigma \cdot s_{ij} = n_i \cdot \left(\sigma' + \sigma_h \begin{pmatrix} 1 & 0 & 0 \\ 0 & 1 & 0 \\ 0 & 0 & 1 \end{pmatrix} \right) \cdot s_{ij} \\ &= n_i \cdot \sigma' \cdot s_{ij} + \sigma_h n_i \cdot \begin{pmatrix} 1 & 0 & 0 \\ 0 & 1 & 0 \\ 0 & 0 & 1 \end{pmatrix} \cdot s_{ij} \\ &= n_i \cdot \sigma' \cdot s_{ij} + \sigma_h n_i \cdot s_{ij} = n_i \cdot \sigma' \cdot s_{ij} \end{aligned} \tag{2.54}$$

The last step follows, as n_i is perpendicular to s_{ij}.

2.5 Fatigue

The previous subchapters only have dealt with static or monotonic loading. In real components, like gas turbine parts, the loads are often cyclic due to vibrations or activation or deactivation processes. Cyclic loading means that several load states alternate in time. In the case of such recurring loads, much lower stresses are sufficient to cause the failure of the material than in the case of a static load.

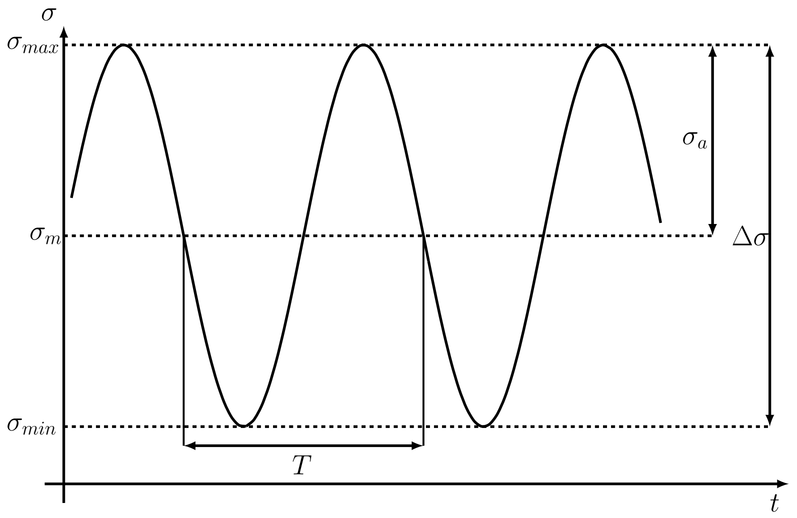

Figure 2.18: Stress-time diagram

2.5.1 Load During Fatigue Testing

The load history of a real component is often very complex. This complexity is reduced in standardized fatigue tests. For example, sine-shaped load-time curves are used. A stress-time diagram for such a stress controlled test is shown in Figure 2.18.

Important variables of such a test are the maximum stress σ_{max} and the minimum stress σ_{min} between which is alternated. Then there is the oscillation bandwidth $\Delta\sigma = \sigma_{\text{max}} - \sigma_{\text{min}}$. The stress amplitude is half of the oscillation bandwidth

$$\sigma_a = \frac{\Delta\sigma}{2}, \tag{2.55}$$

and the mean stress is given by

$$\sigma_m = \frac{\sigma_{\text{max}} + \sigma_{\text{min}}}{2}. \tag{2.56}$$

In such tests, the number of load cycles N_i to failure is measured. Here, a load cycle is the single run through the load change and the number of cycles is given by the time t and oscillation time T via $N_i = t/T$. Material failure in this context is not necessarily a total fracture of the specimen. It rather means that the resistance to load is reduced due to a crack in the material. The failure criteria in such test differ, i.e. in strain controlled fatigue tests a

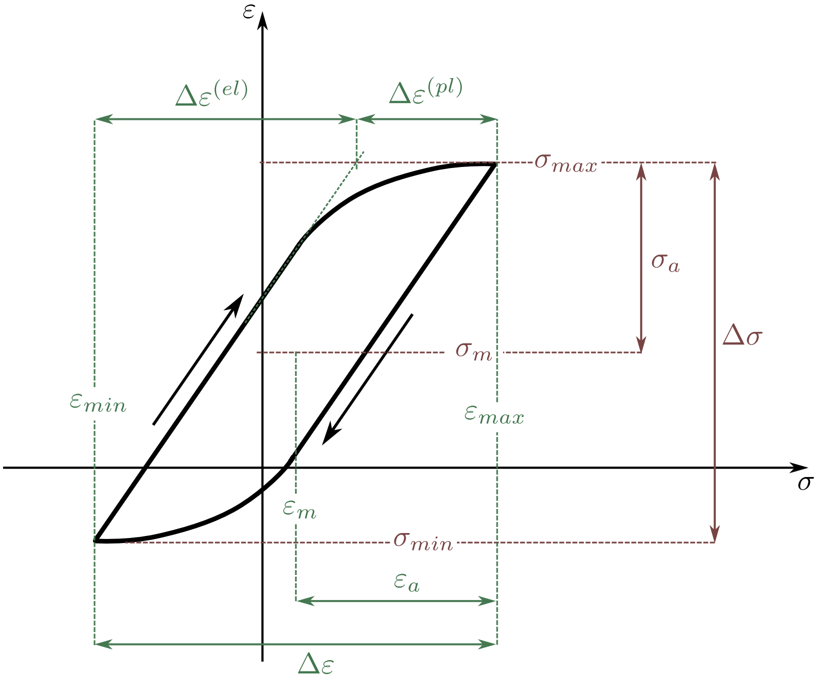

Figure 2.19: Strain-stress Hysteresis under cycle load

reduction of the stress by a certain percentage is often used. This criterion results from the consideration that a crack reduces the cross-sectional area of the specimen. As the stress is proportional to the cross-sectional area, a total crack length can be derived from this stress decrease.

The development of a crack under cyclic loading can be divided into three stages. The first stage (stage I) is the initiation of cracks, which changes into cyclic crack growth (stage II). The last stage (stage III) is the so-called residual fracture.

2.5.2 Stage I: Crack Initiation

Under recurrent loading conditions, cracking often begins where there is a stress concentration in the material. For example, this can be the case at notches built in the geometry. Casting defects and inclusions can also lead to crack initiation under cyclic loading. Also in a defect free material cracks can initiate. Even if the yield point $R_{p0.2}$ is not reached, dislocations start to move under cyclic load, this effect is negligible under static load. We can see that if we plot the strain over the stress for one cycle in a so-called hysteresis loop (Figure 2.19), there is an elastic part of the strain

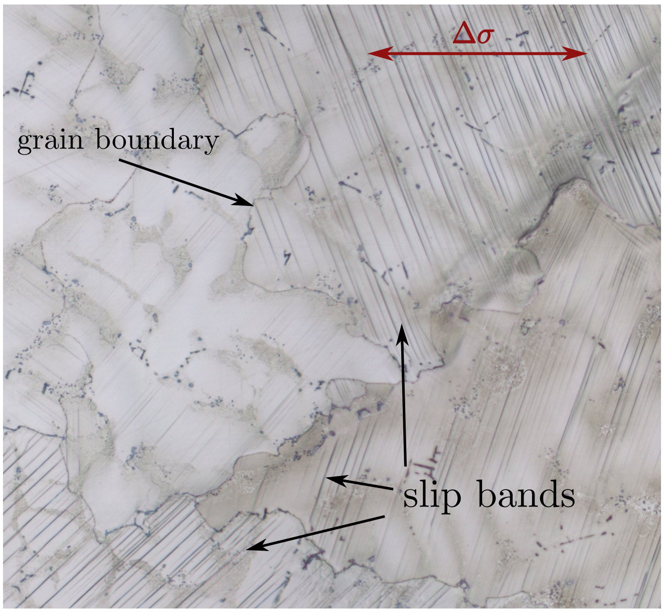

Figure 2.20: Slip bands in a specimen. The direction of the bands varying in distinct grains.

$\Delta\varepsilon^{(pl)}$. The dislocations accumulate at the surface and form slip bands in the direction of the slip system which has the highest shear stress. These slip bands can be seen in microscopic images of the speciemen, an example is shown in Figure 2.20.

Further cyclic loading results in the formation of extrusions and intrusions, this process is shown schematically in Figure 2.21. The surface of the metal becomes rougher. Small cracks can form on the notches formed on the surface and grow into the material in the direction of the slip system.

Due to the higher shear stress in the slip system, grains with an angle close to $\pi/4$ between slip system direction and the main direction of the stress are more likely to start this process.

Under small loads and a speciem without notches, the crack initiation stage is the main part of the fatigue life. The dislocations move slowly through the crystals. Defects and notches have a greater impact as under higher loads, where the dislocations are moving faster.

As the length of such a microcrack increases, so does the stress concentration at the tip of the crack. If this concentration becomes large enough, the growth changes to stage II as shown in Figure 2.22.

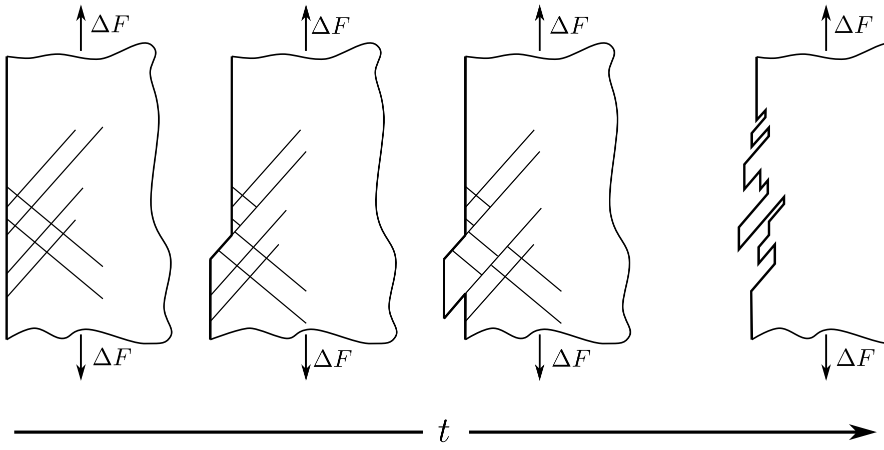

Figure 2.21: Process of building extrusions and intrusions.

2.5.3 Stage II: Crack Propagation

In stage II, the crack no longer grows along the direction of the slip system but perpendicular to the main direction of the stress. This is a consequence of a different mechanism dominating the propagation stage. The loading mode changes from mode II and mode III to mode I, that basically means stresses act rather perpendicular to the crack surface and not parallel to it. For more details see Section 2.6.

The application of stress causes the crack flanks to open, resulting in stress concentration at the crack tip. This stress concentration leads to plasticization of the material in the area of the tip and the crack grows. As the stress is relieved, the crack is closing. A reapplication of tensile load leads again to a crack opening and further growth of the crack. Under constant static load the crack growth would stop, therefore this is so-called stable crack growth.

This process repeats until the crack reaches a critical length.

2.5.4 Stage III: Fracture

The stress intensity in the tip of the crack increases with the length of the crack during the propagation stage. As the intensity becomes lager than fracture toughness K_c of the material, the growth of the crack becomes instable. The crack grows through the reaming cross-section, and the material finally fails.

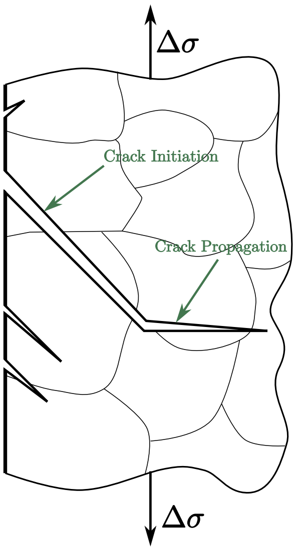

Figure 2.22: Different phases of crack growth

2.5.5 Wöhler Curves

Simple load-time curves are used in laboratory tests to determine the fatigue life of metals. The number of load cycles N_i until a failure criterion is reached is measured. The period time of the load cycles is constant. If for stress controlled tests, the stress amplitude σ_a is plotted against the number of cycles until failure, a stress Wöhler curve or S-N (Figure 2.23a) curve is obtained. Usually, a double logarithmic representation is chosen. In these tests, the ratio $R = \sigma_{\max}/\sigma_{min}$ remains constant.
As the microstructure of metals is random and due to the fact that small defects on the surface of the speciem have a high impact on the fatigue life, the results from these tests scatter widely. Therefore, several tests are performed for each stress amplitude. The failure cycles can be roughly divided into two ranges. Short lifetimes are called low cycle fatigue (LCF) and the longer ones high cycle fatigue (HCF). There is no exact definition for these two ranges but usually about 10^4 cycles are taken as a threshold. The straight line in the log-log plot of the cycle stress relation can be described with the following equation.

Definition 2.2 (Basquin Equation)**.** *The relation between stress amplitude and load cycles till failure for metals can be approximated by*

$$\sigma_a = \sigma' \; \cdot \, (2N_i)^b, \tag{2.57}$$

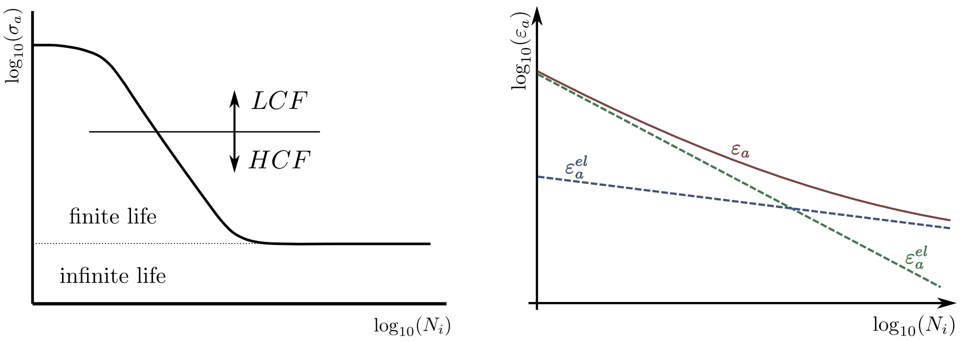

(a) S-N curve

(b) strain-cycle Wöhler diagram

Figure 2.23: Stress-cycle and strain-cycle diagram

where $\sigma' > 0$ *is the material dependent fatigue strength coefficient and* $b < 0$ *is the fatigue strength exponent.*

If we consider a strain Wöhler diagram instead of the stress Wöhler diagram (Figure 2.23b), the strain cycle relation can be approximated with two functions. The blue straight line for higher cycles describes the elastic part of the strain and mainly the HCF behavior. Therefore, if Hooke's law is applied to the Basquin Equation we obtain

$$\varepsilon_a^{el} = \frac{\sigma'}{E}(2N_i)^b. \tag{2.58}$$

The other part, for lower cycles, is mostly driven by plastic deformation.

Definition 2.3 (Coffin-Manson Equation)**.** *Let* $\varepsilon'_f > 0$ *be the material dependent ductility coefficient. Furthermore, let* $c < 0$ *be the ductility exponent, which depends on the solidification of the material. The relation between load cycles and plastic strain can be approximated by the so-called Coffin-Manson Equation:*

$$\varepsilon_a^{pl} = \varepsilon' \ \cdot (2N_i)^c \tag{2.59}$$

To approximate the strain-load-cycle relationship over both ranges, both equations are used in combination.

Definition 2.4 (Coffin-Manson Basquin Equation)**.** *With the same material dependent parameters from definitions 2.2 and 2.3, the relation between total* *strain and load cycles can be approximated by*

$$\mathrm{CMB}(N_i) := \varepsilon_a^{el} + \varepsilon_a^{pl} = \frac{\sigma'}{E}(2N_i)^b + \varepsilon' \ \cdot (2N_i)^c \tag{2.60}$$

To calculate the deterministic number of loading cycles from an applied strain amplitude, the Coffin-Manson Basquin equation (CMB) has to be inverted

$$N_i = \mathrm{CMB}^{-1}(\varepsilon_a). \tag{2.61}$$

2.5.6 Damage Accumulation

As soon as the cyclic load changes over time, neither the Wöhler curves nor the CMB relation can predict the load cycles till failure. A common way to approximate the fatigue lifetime under different loads is Miner's rule. Let there be $k \in \mathbb{N}$ load parts given by $\varepsilon_a^j \in \{1, \ldots, k\}$. Each of the loads was applied for n_j cycles. The portion to the damage D for each load is then given by the ratio $n_j/\mathrm{CMB}^{-1}(\varepsilon_a^j)$. Therefore, the total damage is the sum over all partial damages:

$$D = \sum_{j=1}^{k} \frac{n_j}{\mathrm{CMB}^{-1}(\varepsilon_a^j)} \tag{2.62}$$

If the total damage becomes equal or greater than one, the components fail.

2.6 Stress Intensity Factor

As mentioned before, a crack in the component changes the local stress field. On a macroscopic scale, a crack is a cut in the material, both surfaces of the crack are called crack faces. The tip of the crack is called the crack front (Figure 2.24a). Our aim is to describe the stress increases which is induced due to the crack right in a small area at the crack front. The stress field is influenced on the one hand by the geometry of the component and the cracks and on the other hand by the applied stress.

In linear fracture mechanics there is a whole field dealing with the deter-

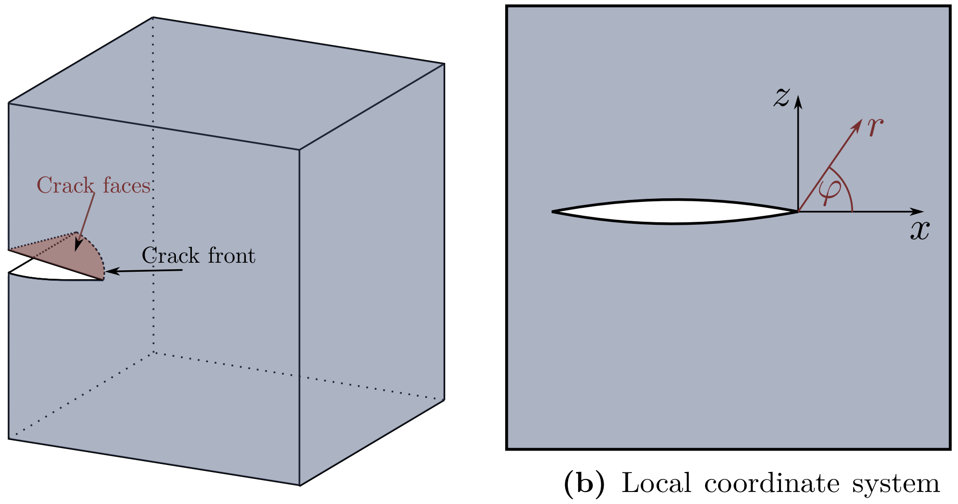

(a) Crack geometry

(b) Local coordinate system at the crack front.

Figure 2.24: Cracked geometry and polar coordinate system for the crack-tip

mination of geometry factors and the crack tip field. This section follows the introduction of K-factors in [35], for a mathematically more rigorous introduction see [54].

As we are interested in the stress at the tip of the crack, it is useful to consider a polar coordinate system with its origin at the tip of the crack (Figure 2.24b). Note that this approach is locally 2-dimensional.

If we consider a crack under load, there are three different types of crack opening that has to be distinguished, which are shown in Figure 2.25. If both crack surfaces open symmetrically and perpendicular to the crack faces, the crack opening is donated with mode I (Figure 2.25a). Under mode II crack opening, both the crack faces open antisymmetrically in the plane of the crack surface but perpendicular to the crack front(Figure 2.25b). In the case that the crack is opening in the direction of the crack front (Figure 2.25c), the crack opening is called mode III. Usually these crack opening modes are just locally defined, i.e. at the tip of the crack.

The crack-tip field can be described with the stress intensity factors (also known as K-factors) K_I, K_{II} and K_{III}. Each of these factors corresponds to one of the crack opening modes. Locally the stress field at the tip of the crack is given, according to [35], due to linear fracture mechanics via

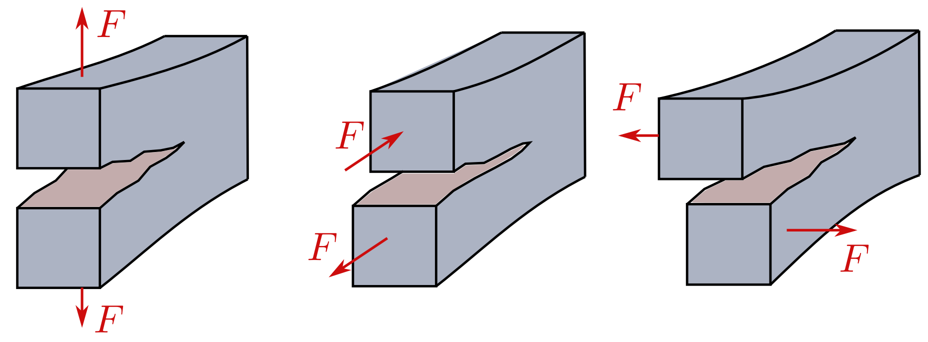

(a) Mode I **(b)** Mode II **(c)** Mode III

Figure 2.25: Different types of crack opening.

$$\sigma_{ij} = \frac{1}{\sqrt{2\pi r}} \left[K_I \tilde{\sigma}_{ij}^{I}(\varphi) + K_{II} \tilde{\sigma}_{ij}^{II}(\varphi) + K_{III} \tilde{\sigma}_{ij}^{III}(\varphi) \right]. \tag{2.63}$$

In the equation $\tilde{\sigma}_{ij}^{I}(\varphi), \ldots, \tilde{\sigma}_{ij}^{III}(\varphi)$ are known functions of the angle φ, so the stress field at the tip of the crack is fully described by the K-factors. For the 2-dimensional case, there is no mode III crack opening and therefore the term $K_{III}\tilde{\sigma}_{ij}^{III}(\varphi)$ is omitted from the equation.

As mentioned before, the K-factors depend on the geometry, including the geometry of the cracks, and the applied stress. In [35] and related literature there are tables for different geometries and load states.

For a straight semi-circular crack in a plane surface with lengths l the K-factors are

$$\begin{pmatrix} K_I \\ K_{II} \end{pmatrix} = \begin{pmatrix} \sigma \\ \tau \end{pmatrix} \cdot \sqrt{\frac{\pi \cdot l}{2}}, \tag{2.64}$$

where σ is the normal stress and τ the shear stress acting in the plane.

2.6.1 Fracture Criteria

Since the stress intensity factors are sufficient to describe the stress field in the region directly at the crack tip, we can use them to specify a fracture criterion in the form of

$$f(K_I, K_{II}, K_{III}) = K_{\text{eq}} - K_c = 0. \tag{2.65}$$

Here K_c is the material dependent fracture toughness. For the 2-dimensional case K_{III} is again omitted.

In the literature, see e.g. [67] and [12], many calculations for the equivalent stress intensity factor K_{eq} can be found. We here use the approach mentioned in [36] which is as follows

$$K_{\text{eq}} = \sqrt{K_I^2 + K_{II}^2}. \tag{2.66}$$

2.7 LCF Experiments

For the fitting and validation of the models we develop in the following, we use LCF failure data from experiments. These experiments were designed at the TU Kaiserslautern. All LCF tests were carried out at an operating temperature of 850°C.

Two different specimen geometries were used for the experiments. For the uniaxial loading case, strain-controlled tests were performed with cylindrical solid specimens. The gauge area of the specimens has a length of 18 mm and a diameter of 7 mm, a schematic representation of these specimens is shown in Figure 2.26.

Two distinct series of test are performed with this geometry. One of which with high strain amplitudes in the range of 0.55 % to 0.65 %. During these tests, the strain is measured by an extensometer. The extensometer measures the distances of two points in the gauge area of the specimen. These experiments were performed with specimens cast with the super alloy RENE80. Within this gauge region, an average of 198 grains are present, leading to an average grain diameter of approximately 1.6 mm. For the experiments, the cycle to fatigue is determined at a stress amplitude reduction of 5%.

The results from this series of experiments are shown in Section 4.5.

The second series of test with this geometry is carried out with lower strain amplitudes, ranging from 0.25% to 0.4%. For these experiments specimens cast with Alloy247 were used. Here, a different failure criteria is employed. Instead of using the drop in load we use the direct current potential drop (DCPD) method. For the DCPD-method, direct current is applied to the

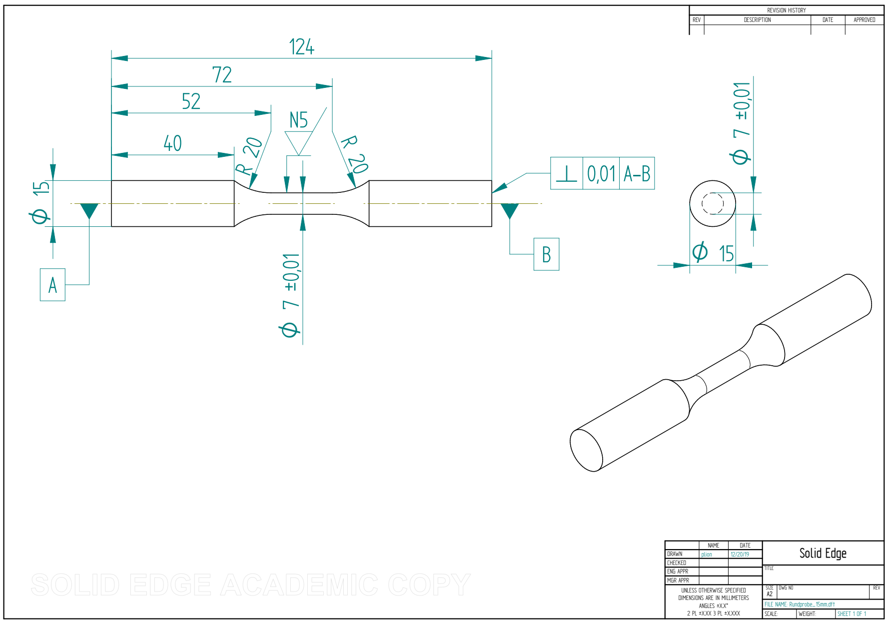

Figure 2.26: Technical drawing of the solid specimens. Reprinted with permission of the RPTU Kaiserslautern-Landau.

specimen and the change in electrical resistance is measured. A crack in the specimen reduces the cross-sectional area during the application of tensile load and therefore increases the electrical resistance of the specimen.
The cycle of failure is the first load cycle in which the change in resistance exceeds a pre-defined threshold. If a specimen is cracked, the measurement of the strain can depend on the position of the extensometer. The advantage of the DCPD method is that it does not rely on the measurement of the strain.
We use the results of these experiments in Section 6.3 to fit our model.

In a third series of experiments, the impact of multiaxial loading conditions on the LCF life onto the material is investigated. Here, a different specimen geometry is employed. Instead of a solid geometry hollow specimen are used (Figure 2.27). The specimens have an inner diameter of 6 mm. The gauge area has a diameter of 10 mm and a length of 20 mm. These stress controlled experiments are performed with 4 different stress levels σ_{vM} ranging from 450 MPa to 600 MPa. Instead of a pure uniaxial tensile stress, a mixture of tensile and torsional stress is applied. On each stress level several distinct portions of tensile and torsional stress are used. The failure criterion for

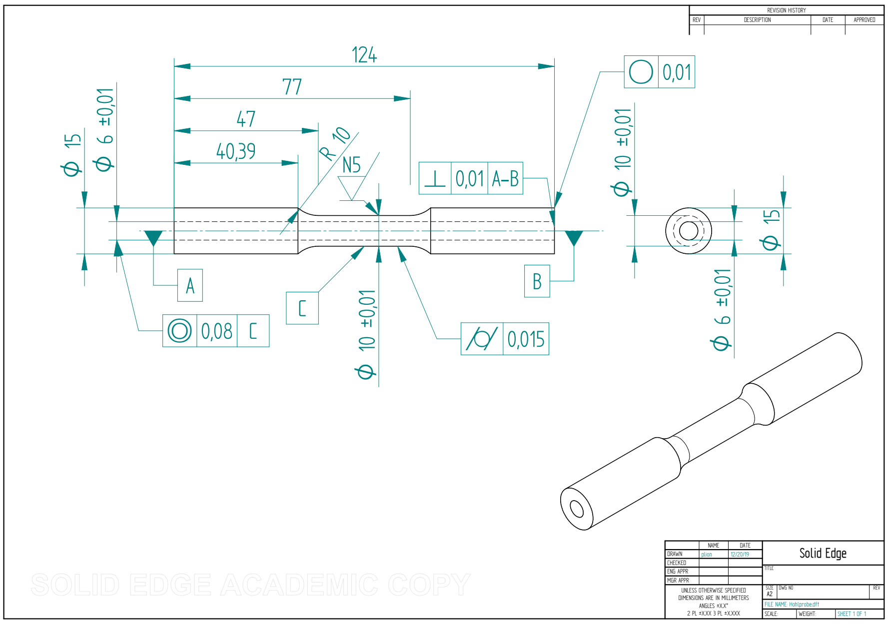

Figure 2.27: Technical drawing of the hollow specimens. Reprinted with permission of the RPTU Kaiserslautern-Landau.

this series of experiments is a change in electrical resistance with the DCPD method.

3. Mathematic Foundation

3.1 Boundary Value Problem

For the linear elastic case, the relationship between deformation u, strain ε, and stress σ introduced in Section 2 can be expressed mathematically as a variational problem, which is as follows. Let $f : \Omega \to \mathbb{R}^3$ be the body force and $g : \Omega \times S^2 \to \mathbb{R}^3$ the surface force, where S^2 is the unit sphere of $\mathbb{R}^3$. The variational problem is to minimize the energy

$$\Pi(u) := \int_\Omega \left[\frac{1}{2}\varepsilon(x) : \sigma(x) - f(x)u(x)\right] dx - \int_{\partial\Omega} g(x) \cdot u(x)\, dx, \tag{3.1}$$

where $\varepsilon(x) : \sigma(x) := \sum_{ij} \varepsilon_{ij}\sigma_{ij}$.
The solution of the associated boundary value problem can be approximated using the finite element method (FEM). This section closely follows [10, 14, 24].

3.1.1 Weak Solutions

Before we introduce the finite element method, we have to define the boundary value problem (BVP) and give a short summary about important results that state the existence of unique weak solutions for the BVPs. For the definition we need a smoothness property of the boundary of the domain. Therefore, we assume that the boundary of the domain is a Lipschitz boundary [45].

Definition 3.1. *Let $\Omega \subseteq \mathbb{R}^3$, be a domain with piecewise Lipschitz boundary $\partial\Omega$. Furthermore, let $\partial\Omega_D \subseteq \Omega$ be the Dirichlet boundary and $\partial\Omega_N = \partial\Omega \setminus \Omega_D$ the Neumann boundary. Assume, that*

$$Lu(x) := \sum_{i,k} \partial_i(a_{ik}(x)\partial_k u(x)) + a_0(x)u(x), \tag{3.2}$$

where the matrices $A(x) := (a_{ik}(x))_{i,j}$ *are positive definite and* $a_0(x) \geq 0$ *for* $x \in \Omega$*, be a second order elliptic partial differential operator. The elliptic boundary value problem with mixed boundary conditions is given by*

$$\begin{aligned} Lu(x) = \hat{f}(x) \quad x \quad &\in \Omega, \\ u(x) = \hat{g}(x) \quad x \quad &\in \partial\Omega_D, \\ \sum_{i,k} n_i(x) a_{ik}(x) \partial_k u(x) = \hat{h}(x) \quad x \quad &\in \partial\Omega_N. \end{aligned} \tag{3.3}$$

In (3.3), $n_i(x)$ *is the on* $\partial\Omega$ *almost everywhere defined outward pointing normal and* $\hat{f}, \hat{g}$ *and* $\hat{h}$ *are arbitrary functions on* Ω*.*

If $\partial\Omega_N = \emptyset$ then we have an elliptic boundary value problem with Dirichlet boundary conditions and if $\partial\Omega_D = \emptyset$ it is called an elliptic boundary value problem with Neumann boundary conditions.
Boundary value problems with pure Dirichlet boundary conditions can be transformed to problems with homogeneous boundary conditions. Therefore, it is assumed that there is a known function u_0 with $u_0(x) = \hat{g}(x)$, for $x \in \partial\Omega$. Then the BVP

$$\begin{aligned} Lu(x) = \hat{f}(x) \quad x \quad &\in \Omega, \\ u(x) = \hat{g}(x) \quad x \quad &\in \partial\Omega, \end{aligned} \tag{3.4}$$

can be rewritten as

$$\begin{aligned} Lu(x) = \hat{f}_1(x) \quad x \quad &\in \Omega, \\ u(x) = 0 \quad x \quad &\in \partial\Omega, \end{aligned} \tag{3.5}$$

where $\hat{f}_1 := \hat{f} - Lu_0$.
The existence of weak solutions for the boundary value problem can be shown, with the variational formulation of the problem. Therefore, we need the following theorem.

Theorem 3.2 (Characterization Theorem)**.** *Assume that* V *is a linear space and*

$$a : V \times V \to \mathbb{R} \tag{3.6}$$

is a symmetric, positive bilinear form, that means $a(u, u) > 0, \forall u \in V, u \neq 0$*.*

Further, suppose that

$$l : V \to \mathbb{R} \tag{3.7}$$

is a linear functional. Then

$$J(v) := \frac{1}{2}a(v,v) - \langle l, v\rangle \tag{3.8}$$

is minimal in $u \in V$*, if and only if*

$$a(u,v) = \langle l, u\rangle \qquad \forall v \in V. \tag{3.9}$$

Furthermore, this solution is unique.

Proof. See [10]. ☐

With this theorem it can be shown, that every solution of the BVP (3.5) is also a solution for the variational problem with

$$\min J(v(x)) := \int_\Omega \left[\frac{1}{2}\sum_{i,k} a_{ik}(x)\partial_i v(x)\partial_k v(x) + \frac{1}{2}a_0(x)v(x)^2 - \hat{f}(x)v(x)\right] dx, \tag{3.10}$$

over all functions in $C^2(\Omega) \cap C^0(\bar{\Omega})$. Therefore, we set

$$a(u,v) := \int_\Omega \left[\sum_{i,j} a_{ik}(x)\partial_i u(x)\partial_k v(x) + a_0(x)u(x)v(x)\right] dx \tag{3.11}$$

$$\langle l, v\rangle := \int_\Omega \hat{f}(x) \cdot v(x)\, dx. \tag{3.12}$$

In the proof of this property, which is given in [10], it is also shown, that every solution in $C^2(\Omega) \cap C^0(\bar{\Omega})$ for the variational problem (3.10) is a classical solution for the BVP.
What remains is the existence of such solutions. This can be achieved by solving the variational problem in a suitable Hilbert space.

Definition 3.3. *Assume that* H *is a Hilbert space. A bilinear form* $a : H \times H \to \mathbb{R}$ *is called continuous, if* $C > 0$ *exist such that*

$$|a(u,v)| \leq C\|u\| \cdot \|v\| \qquad \forall u, v \in H \tag{3.13}$$

holds. A symmetric, continuous bilinear form a is called H-elliptic, if

$$a(v, v) \geq \alpha \|v\|^2 \qquad \forall v \in H \tag{3.14}$$

and some $\alpha > 0$.
An H-elliptic bilinear form a induces a norm which is given by

$$\|v\|_a := \sqrt{a(v, v)}. \tag{3.15}$$

This norm is equivalent to the norm of the Hilbert space and is called energy-norm.

With this definition we can formulate the following important theorem. Note that V' denote the space of continuous linear functionals on a normed space V.

Theorem 3.4. *(Lax-Milgram) Let* $V \subset H$ *be a closed convex set in a Hilbert space* H*. Assume that,* $a : H \times H \to \mathbb{R}$ *is an elliptic bilinear form. Then the variational problem*

$$\min J(v) := \frac{1}{2} a(v, v) - \langle l, v \rangle \tag{3.16}$$

has a unique solution for every $l \in H'$ *in* V.

Proof. see [10] □

We now introduce a different solution concept for BVP, the so-called weak solutions.

Definition 3.5 (Weak Solution)**.** *A function* $u \in H_0^1(\Omega)$ *is called a weak solution of the elliptic boundary value problem with Dirichlet boundary conditions from definition 3.1, if for the associated bilinear form* $a(u, v)$ *the equation*

$$a(u, v) = (f, v)_0 \tag{3.17}$$

holds for all $v \in H_0^1(\Omega)$.

With the Lax-Milgram theorem the existence of weak solutions for the homogeneous boundary value problem can be shown.

Theorem 3.6 (Existence for Dirichlet BVP)**.** *Let L be a second order uniformly elliptic partial differential operator. Then the elliptic boundary value problem with Dirichlet boundary conditions (see definition 3.1) has a weak solution in $H_0^1(\Omega)$. The solution is the minima of the variational problem*

$$\min_{v \in H_0^1(\Omega)} \frac{1}{2} a(v,v) - (\hat{f}, v)_0. \tag{3.18}$$

Proof. see [10] □

For the boundary value problem with Neumann boundary conditions, the differential is again assigned with the bilinear form a as in equation (3.11). Additionally, it is assumed, that $a_0(x)$ is positive and bounded from below. With the additional assumption the quadratic form $a(v,v)$ is elliptic on $H^1(\Omega)$. With $\hat{f} \in L_2(\Omega)$ and $\hat{h} \in L_2(\partial\Omega)$ we set the linear functional from equation (3.12) as

$$\langle l, v \rangle := \int_\Omega \hat{f}(x) v(x)\, dx + \int_{\partial\Omega} \hat{h}(x) v(x)\, dx. \tag{3.19}$$

For the following theorem, we need a further property of the set Ω, the cone property. For a cone with direction ζ, opening angle θ and height l, we use the notation

$$C(\zeta, \theta, l) = \{x \in \mathbb{R}^3 : |x| < l, x \cdot \zeta > |x| \cos(\theta)\}. \tag{3.20}$$

Now we give the definition of the cone property [8, 13].

Definition 3.7. *Let $\Omega \subset \mathbb{R}^3$ be a bounded open set. For $\theta \in]0, \pi/2[$, $l > 0$ and $0 < 2r < l$ the subset $\hat{\Omega} \subset \Omega$ fulfills the cone property, if for every $x \in \partial\hat{\Omega}$ there exists a cone $C_x = C_x(\zeta_x, \theta, l)$, where ζ_x is a unit vector in $\mathbb{R}^3$, such that*

$$y + C_x \subset \hat{\Omega}, \qquad y \in B(x,r) \cap \hat{\Omega}, \tag{3.21}$$

here $B(x,r) \subset \mathbb{R}^3$ is the open Ball with center x and radius r.

Theorem 3.8 (Trace Theorem)**.** *Let $\Omega \subset \mathbb{R}^3$ be bounded with a piecewise Lipschitz boundary. Furthermore, let Ω fulfill the cone property. Then there exists a linear bounded mapping,*

$$\gamma : H^1(\Omega) \to L_2(\partial\Omega), \qquad ||\gamma(v)||_{o,\partial\Omega} \le c||v||_{1,\Omega}, \tag{3.22}$$

with $\gamma v = v_{|\partial\Omega}$ *for all* $v \in C^1(\Omega)$.

Proof. see [10] ☐

For the proof of the next theorem we need Green's formula.

Lemma 3.9. *Green's formula Let* $\Omega \subseteq \mathbb{R}^3$. *For* $u, v \in C^1(\bar{\Omega})$ *it holds, that*

$$\int_\Omega u(x)\partial_i v(x)\, dx = -\int_\Omega v(x)\partial_i u(x)\, dx + \int_{\partial\Omega} u(x)v(x)n_i(x)\, dx, \tag{3.23}$$

with $n_i(x)$ *is normal* $x \in \partial\Omega$.

Proof. For the proof, we refer to [68]. ☐

Now we can prove the existence of solutions for the boundary value problem with Neumann boundary conditions.

Theorem 3.10. *Let* Ω *fulfill the same properties as in the trace theorem (3.8). There exists a unique solution* $u \in H^1(\Omega)$ *for the variational problem*

$$\min J(v) := \frac{1}{2}a(v,v) - (f,v)_{0,\Omega} - (g,v)_{0,\partial\Omega}. \tag{3.24}$$

Furthermore, it holds that the solution $u \in C^2(\Omega) \cap C^1(\bar{\Omega})$, *if and only if* u *is the classical solution for the boundary value problem*

$$\begin{aligned} Lu(x) &= \hat{f}(x) \quad x \quad \in \Omega, \\ \sum_{i,k} n_i(x)a_{ik}(x)\partial_k u(x) &= \hat{g}(x) \quad x \quad \in \partial\Omega. \end{aligned} \tag{3.25}$$

Proof. The bilinear form a is H^1-elliptic, therefore it follows, with the Lax-Milgram theorem, that there exists a unique solution $u \in H^1(\Omega)$. Furthermore, with

$$a(u,v) = (f,v)_{0,\Omega} + (g,v)_{0,\partial\Omega} \qquad \forall v \in H^1(\Omega) \tag{3.26}$$

u is characterized. Now, suppose that $u \in C^2(\Omega) \cap C^1(\bar{\Omega})$. For $v \in H^1_0(\Omega)$ it holds that $\gamma v = 0$, therefore with (3.26) it follows

$$a(u,v) = (f,v)_0 \qquad \forall v \in H^1_0(\Omega). \tag{3.27}$$

From this it can be shown that u solves the Dirichlet problem. It is

$$Lu(x) = \hat{f}(x) \qquad x \in \Omega. \tag{3.28}$$

With Green's formula, we obtain for $v \in H^1(\Omega)$

$$\begin{aligned}\int_\Omega v(x)\partial_i(a_{ik}(x)\partial_k u(x))\,dx = &-\int_\Omega \partial_i v(x) a_{ik}(x)\partial_k u(x)\,dx \\ &+ \int_{\partial\Omega} v(x)a_{ik}(x)\partial_k u(x) n_i(x)\,dx.\end{aligned} \tag{3.29}$$

Therefore, we have

$$\begin{aligned}a(u,v) - (f,v)_0 - (g,v)_{0,\partial\Omega} = &\int_\Omega v(x)\left[Lu(x) - f(x)\right]\,dx \\ &+ \int_{\partial\Omega}\left[\sum_{i,k} n_i(x)a_{ik}\partial_k u(x) - \hat{g}(x)\right] v(x)\,dx.\end{aligned} \tag{3.30}$$

It is easy to see, that with equation (3.26) and (3.28) the second integral on the right in equation (3.30) vanishes. Suppose that $v_0(x) := n_i(x)a_ik(x)\partial_k u(x) - \hat{g}(x)$ does not vanish. It follows that $\int_{\partial\Omega} v_0(x)^2\,dx > 0$. Now, $C^1(\bar{\Omega})$ is dense in $C^0(\bar{\Omega})$, and therefore there exists a $v \in C^1(\bar{\Omega})$, such that $\int_{\partial\Omega} v_0(x)v(x)\,dx > 0$. This is a contradiction to the assumptions. Hence, the boundary conditions are satisfied. From (3.30) on the other hand, it follows that every solution of (3.26) satisfies (3.25). □

3.1.2 Linear Elasticity as a Boundary Value Problem

In this section the variational problem (3.1) is formulated as an BVP. To the contrary to Section 2, here we use a slightly different notation for the material laws. The relation between the displacement u and the strain ε is given by:

$$\varepsilon_{ij}(x) = \frac{1}{2}\left(\frac{\partial u_i(x)}{\partial x_j} + \frac{\partial u_j(x)}{\partial x_i}\right) \qquad \text{for } x \in \Omega, \tag{3.31}$$

so $\varepsilon\left(u(x)\right) := \nabla u(x)$. The relation between strain and stress, introduced in Section 2 as Hook's Law can be rewritten

$$\begin{aligned} \varepsilon(u(x)) &= \frac{1+\nu}{E}\sigma(x) - \frac{\nu}{E}\operatorname{tr}(\sigma(x)) \cdot I, && (3.32)\\ \sigma(x) &= \frac{E}{1+\nu}\left(\varepsilon(x) + \frac{\nu}{1-2\nu}\operatorname{tr}(\varepsilon(u(x))) \cdot I\right). && (3.33) \end{aligned}$$

Here, we use instead of the Poisson ratio and Young modulus the Lame coefficients:

$$\lambda = \frac{E\nu}{(1+\nu)(1-2\nu)}, \quad \mu = \frac{E}{2(1+\nu)} \tag{3.34}$$

Therefore, equation (3.33) becomes:

$$\sigma(x) = \lambda\operatorname{tr}(\varepsilon(u(x)))I + 2\mu\,\varepsilon(u(x)). \tag{3.35}$$

Hence, for the energy density in (3.1) it follows

$$\begin{aligned} \frac{1}{2}\sigma(x) : \varepsilon(u(x)) &= \frac{1}{2}\left(\lambda\operatorname{tr}(\varepsilon(u(x))) \cdot I + 2\mu\,\varepsilon(u(x)) : \varepsilon(u(x))\right) && (3.36)\\ &= \frac{\lambda}{2}\left(\operatorname{tr}(\varepsilon(u(x)))\right)^2 + \mu\,\varepsilon(u(x)) : \varepsilon(u(x)). && (3.37) \end{aligned}$$

With this we can express Π in the variational problem (3.1) as

$$\begin{aligned} \Pi(u) := \int_\Omega \left[\mu\varepsilon(u(x)) : \varepsilon(u(x)) + \frac{\lambda}{2}(\operatorname{div} v)^2 - f(x)u(x)\right] dx \\ - \int_{\partial\Omega_N} g(x) \cdot u(x)\, dx. \end{aligned} \tag{3.38}$$

The boundary $\partial\Omega$ is divided into the part where the zero Boundary condition holds $\partial\Omega_D$ and the part $\partial\Omega_N$, where forces may act on. Following [10], we obtain the differential equation

$$\begin{aligned} -\operatorname{div}\,\sigma(x) &= \hat{f}(x) && x \in \Omega,\\ u(x) &= 0 && x \in \Omega_D,\\ \sigma(x) \cdot n(x) &= \hat{g}(x) && x \in \Omega_N, \end{aligned} \tag{3.39}$$

where div $\sigma(x)$ is the trace of the Jacobian of σ at x and σ as in equation (3.35).

Theorem 3.11. *(Korn's Inequality) Let $\Omega \subset \mathbb{R}^3$ an open, bounded subset* *with piecewise Lipschitz boundary. Assume that $\partial\Omega_D$ has a positive two-dimensional measure. Then, there exists a $c = c(\Omega, \partial\Omega_D) \geq 0$, such that*

$$\int_\Omega \varepsilon(v(x)) : \varepsilon(v(x))\, dx \geq c||v||_1^2 \quad \text{for } v \in H^1_{\partial\Omega}(\Omega) \tag{3.40}$$

holds. Here $H^1_{\partial\Omega}$ is the closure of $\{v \in C^\infty(\Omega)^3; v(x) = 0 \text{ for } x \in \partial\Omega_D\}$ with respect to the $\| \cdot \|_1$-norm.

Proof. See [10]. ☐

With Korn's Inequality, it holds that the variational problem (3.38) is elliptic, so with the results from Section 3.1.1, we gain the following theorem.

Theorem 3.12. *Suppose $\Omega \subset \mathbb{R}^3$ is a domain with picewise Lipschitz boundary and $\partial\Omega_D$ has a positive two-dimensional measure. Then the variational problem (3.38) has a unique solution.*

Now we can state the variational formulation for the linear elastic PDE

$$a(u, v) = \int_\Omega f(x) \cdot v(x)\, dx + \int_{\partial\Omega} g(x) \cdot v(x)\, dA, \forall v \in H^1_{\partial\Omega}(\Omega), \tag{3.41}$$

where the bilinear form a is given by

$$\begin{align} a(u, v) &= \int_\Omega \varepsilon(v(x)) : \sigma(u(x))\, dx \tag{3.42} \\ &= \lambda \int_\Omega \operatorname{div}(u(x)) \operatorname{div}(v(x))\, dx + 2\mu \int_\Omega \varepsilon(u(x)) : \varepsilon(v(x))\, dx. \tag{3.43} \end{align}$$

3.1.3 Finite Element Method

A possible way to solve elliptic boundary value problems numerically is the finite element method (FEM). For this purpose, the variational problem to find the minima of the functional J (equation 3.16) is not solved over the Sobolev space $H^m(\Omega)$ but over a discretized, finite dimensional subspace S_h. Therefore, in the two-dimensional case, the domain Ω is partitioned for example by triangles or quadrilaterals, and in the three-dimensional case by tetrahedrons or cuboids. The next definition introduces some requirements for such a partition of the domain Ω.

Definition 3.13. *(i) Let $\mathcal{T} = \{K_1, \ldots, K_N\}$ be a partition of Ω into triangles or quadrilaterals, and in the three-dimensional case into*

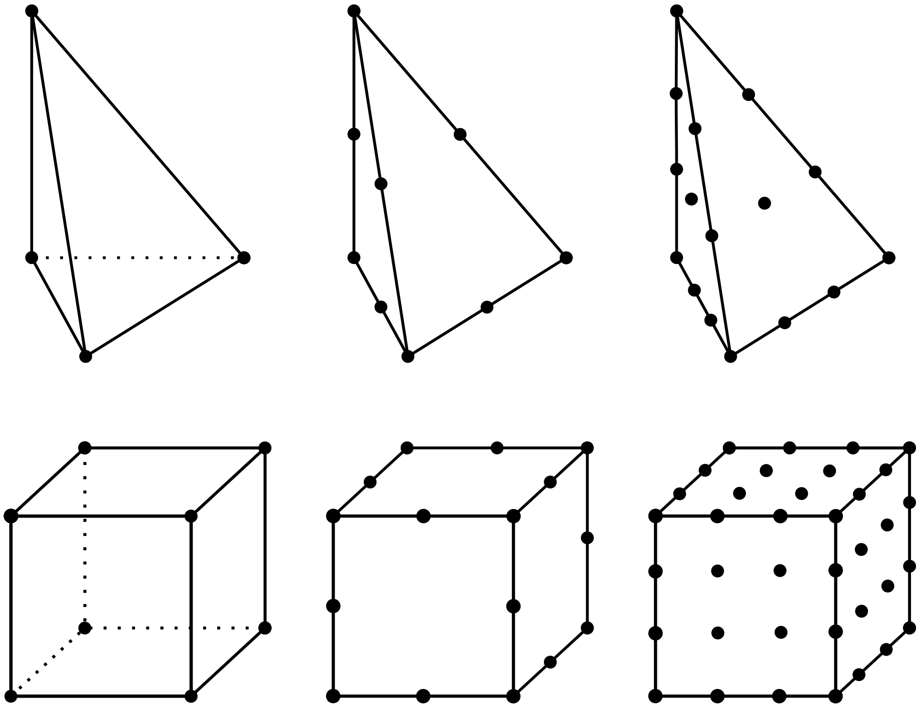

Figure 3.1: Tetrahedron and Cube 3-dimensional linear, quadratic and cubic Lagrange finite elements.

tetrahedrons or rectangular parallelepipeds, respectively. $\mathcal{T}$ *is called admissible if,*

a) $\bar{\Omega} = \bigcup_{i=1}^{N} \bar{K}$

b) $K_i \cap K_j = \emptyset, \quad i \neq j, \quad ,\forall i, j \in \{1, \dots, N\}$

c) K_i *is open for all* $i \in \{1, \dots, N\}$

(ii) We use the notation $\mathcal{T}_h$ *instead of* $\mathcal{T}$*, if the diameter of each element of* $\mathcal{T}$ *is at most* $2h$

(iii) A family of partitions $\{\mathcal{T}_h\}$ *is called shape regular if there exist a* $\kappa > 0$ *such that every* K *in* $\mathcal{T}_h$ *contains a ball of radius* ρ_K *with*

$$\rho_K \geq h_K/\kappa, \tag{3.44}$$

where h_K *is the half diameter of K.*

(iv) A family of partitions $\{\mathcal{T}_h\}$ *is called uniform if there exist a* $\kappa > 0$ *such that every* K *in* $\mathcal{T}_h$ *contains a ball of radius* $\rho_K \geq h/\kappa$

Next we give a formal definition of a finite element.

Definition 3.14. *A finite element is a triplet* $\{K, P, \Sigma\}$*, with:*

(i) *K is a polyhedron in $\mathbb{R}^d, d = 2, 3$.*

(ii) *P is a vector space of functions $p : K \to \mathbb{R}^m$ for some integer m*

(iii) *Σ is a set of n_{sh} linear forms $\{\varphi_1, \dots, \varphi_{n_{sh}}\}$ acting on the elements of P, and such that the linear mapping*

$$P \ni p \longmapsto (\varphi_1(p), \dots, \varphi_{n_{sh}}(p)) \in \mathbb{R}^{n_{sh}}, \tag{3.45}$$

is bijective, i.e., Σ is a basis $\mathcal{L}(P; \mathbb{R})$. The linear forms $\{\varphi_1, \dots, \varphi_{n_{sh}}\}$ are called the local degrees of freedom.

If the local degrees of freedom form a basis of P, they are called local shape functions and are denoted by $\{\theta_1, \dots, \theta_{n_{sh}}\}$. So with the local shape functions every function $u \in P(K)$ can be rewritten as

$$u = \sum_{i=1}^{n_{sh}} u_i \theta_i, \qquad u_i \in \mathbb{R}. \tag{3.46}$$

The finite elements that we use here have an additional property.

Definition 3.15 (Lagrange finite element)**.** *A finite element $\{K, P, \Sigma\}$ is called a Lagrange finite element if there exists a set of points $\{a_1, \dots, a_{n_{sh}}\}$ in K for which it holds that for all $p \in P$:*

$$\varphi_i(p) = p(a_i), \qquad 1 \le i \le n_{sh}. \tag{3.47}$$

The points $\{a_1, \dots, a_{n_{sh}}\}$ are the so-called nodes of the finite element. The local shape functions $\{\theta_1, \dots, \theta_{n_{sh}}\}$ are called the nodal basis of P.

The tetrahedral (ted) and hexahedral (brick) Lagrange elements are shown in Figure 3.1.

Definition 3.16 (Affine Family)**.** *A family of partitions $\{\mathcal{T}_h\}$ of $\Omega \subseteq \mathbb{R}^d, d = 2, 3$ is called an affine family, if there exists a finite element $\{\hat{K}, \hat{P}, \hat{\Sigma}\}$, with the following properties. For all $K \in \mathcal{T}_h$, there exist an affine mapping $T_K : \hat{K} \to K$ such that*

(i) $\hat{\Pi} = \Pi \circ T_K$*,*

(ii) $\hat{\theta}_j := \theta_j \circ T_K$*,*

(iii) $\hat{\varphi}_j(p \circ T_K) := \varphi_j(p)$*.*

$\{\hat{K}, \hat{P}, \hat{\Sigma}\}$ is called the reference element. $\hat{\theta}_j$ are the local shape functions and $\hat{\varphi}_j$ the local degrees of freedom on the reference element for each K.

We now give a brief introduction to the Galerkin method, which is an approach to transform the analytical variational problem (3.16) into an algebraic form.

Theorem 3.2 ensures the existence of a solution for the variational problem

$$\min_{S_h} J(v) := \frac{1}{2}a(u,v) - \langle l, v\rangle, \tag{3.48}$$

where S_h is a subspace of V. Furthermore, it follows that $u_h \in S_h$ is a solution if

$$a(u_h, v) = \langle l, v\rangle, \qquad \forall v \in S_h \tag{3.49}$$

holds. Let $\{\theta_1, \dots, \theta_{n_{sh}}\}$ be a basis of S_h, then (3.49) is equivalent to

$$a(u_h, \theta_i) = \langle l, \theta_i\rangle, \qquad i = 1, \dots, n_{sh}. \tag{3.50}$$

With

$$u_h = \sum_{k=1}^{n_{sh}} z_k \theta_k, \tag{3.51}$$

we obtain the following system of equations

$$\sum_{k=1}^{n_{sh}} a(\theta_k, \theta_i) z_k = \langle l, \theta_i\rangle, \qquad i = 1, \dots, n_{sh}. \tag{3.52}$$

We can rewrite the equation in matrix-vector form as

$$Bz = b, \tag{3.53}$$

with $B_{ik} = a(\theta_k, \theta_i)$ and $b_i = \langle l, \theta_i\rangle$. If a is an H^m-elliptic bilinear form, B is positive definite. Therefore, this approach leads to a unique solution.

For the discretization of the linear elastic equation

$$a(u,v) = \int_\Omega f(x) \cdot v(x)\, dx + \int_{\partial\Omega} g(x) \cdot v(x)\, dA, \forall v \in H^1_{\partial\Omega,h}(\Omega, \mathbb{R}^3), \tag{3.54}$$

by Lagrange fininte elements we follow the approach proposed in [29] and [9]. The integrals are approximated via Gauss quadrature. We partitioned the domain $\Omega \subset \mathbb{R}^d, d = 2, 3$, with a finite mesh $\mathcal{T}_h$ with N grid points $X = \{X_1, \dots, X_N\}$. With this mesh we obtain N_{el} Lagrange finite elements

$\{K, P, \Sigma\}$. So, for each element K we have n_{sh} local shape functions which are defined by the nodes $X_1^K, \dots, X_{n_{sh}}^K \in X$. With the assumption that the family of finite elements is affine, we obtain a reference element $\{\hat{K}, \hat{P}, \hat{\Sigma}\}$ and the bijective transformation $T_K : \hat{K} \to K$ for each K as introduced in Definition 3.16. It is

$$T_K = T_K(\hat{x}, X) = \sum_{j=1}^{n_{sh}} \hat{\theta}_j(\hat{x}) X_j^K, \qquad \hat{x} \in \hat{K}. \tag{3.55}$$

For the numerical quadrature of the integral, we chose q^K quadrature points $\hat{x}_l^K$ for each $K \in \mathcal{T}_h$ with weights $\hat{\omega}_l^K$. The discretized version of the bilinear form (3.42) is given as follows

$$\begin{aligned}
a(u, v) &= \lambda \sum_{K \in \mathcal{T}_h} \int_K \operatorname{div}(u(x)) \operatorname{div}(v(x))\, dx + 2\mu \sum_{K \in \mathcal{T}_h} \int_K \varepsilon(u(x)) : \varepsilon(v(x))\, dx \\
&= \lambda \sum_{K \in \mathcal{T}_h} \int_K \operatorname{div}(u(T_K(\hat{x})))\, \operatorname{div}(v(T_K(\hat{x}))) \det(\hat{\nabla} T_K(\hat{x}))\, d\hat{x} \\
&+ 2\mu \sum_{K \in \mathcal{T}_h} \int_K \varepsilon(u(T_K(\hat{x}))) : \varepsilon(v(T_K(\hat{x}))) \det(\hat{\nabla} T_K(\hat{x}))\, d\hat{x} \\
&\approx \lambda \sum_{K \in \mathcal{T}_h} \sum_{l=1}^{q^K} \hat{\omega}_l^K \operatorname{div}(u(T_K(\hat{x})))\, \operatorname{div}(v(T_K(\hat{x}))) \det(\hat{\nabla} T_K(\hat{x})) \\
&+ 2\mu \sum_{K \in \mathcal{T}_h} \sum_{l=1}^{q^K} \hat{\omega}_l^K \varepsilon(u(T_K(\hat{x}))) : \varepsilon(v(T_K(\hat{x}))) \det(\hat{\nabla} T_K(\hat{x})).
\end{aligned}$$

Now we can express $u(x)$ with the local shape functions on the reference element with $u(x) = \sum_{m=1}^{n_{sh}} u_m \hat{\theta} \circ T_K^{-1}(x)$ and therefore

$$\nabla u(x) = \sum_{m=1}^{n_{sh}} u_m \otimes (\hat{\nabla}(\hat{x})^T)^{-1} \hat{\nabla} \theta_m(\hat{x}). \tag{3.56}$$

Hence,

$$\operatorname{div}(u(x)) = \sum_{m=1}^{n_{sh}} \operatorname{tr}(u_m \otimes (\hat{\nabla}(\hat{x})^T)^{-1} \hat{\nabla} \theta_m(\hat{x})). \tag{3.57}$$

The volume force can be discretized in a similar way to the bilinear form

$$\int_\Omega f(x) \cdot v(x)\, dx = \sum_{K \in \mathcal{T}_h} \sum_{l=1}^{q^K} \hat{\omega}_l^K \det\left(\hat{\nabla} T_K(\hat{x}_l)\right) f(T_K(\hat{x}_l)) \cdot v(T_K(\hat{x}_l)). \tag{3.58}$$

For the surface force only faces F of the finite elements K that lie on $\partial\Omega$

are taken into account. Therefore, let $\mathcal{N}_h$ be the set of all the Faces that lie on $\partial\Omega$ and $K = K(F) \in \mathcal{T}_h$ be the respective elements. Assume that $\hat{F}$ be the face of the reference element $\hat{K}$ with $T_{K(F)} : \hat{F} \to F$. For the quadrature additional q^F quadrature points $\hat{x}_l^F$ and weights $\hat{\omega}_l^F$ have to be chosen. The determinant of the derivative of T_K has to be replaced with the square root of the Gram determinant $\sqrt{\det g_F(\hat{x}_l^F)}$, which is given by

$$g_F(\hat{x}) = \hat{\nabla}(T_K|_{\hat{F}})(\hat{x}) \left(\hat{\nabla}(T_K|_{\hat{F}})\right)^T (\hat{x}). \tag{3.59}$$

So for the surface force we finally obtain

$$\int_{\partial\Omega} g(\hat{x}) \cdot v(\hat{x})\, dA = \sum_{F \in \mathcal{N}_h} \sum_{l=1}^{q^F} \hat{\omega}_l^F \sqrt{\det g_F(\hat{x})} g(T_{K(F)}(\hat{x}_l^F)) \cdot v(T_{K(F)}(\hat{x}_l^F)). \tag{3.60}$$

3.2 Rotations

As mentioned in Section 2, within a given grain the material properties of nickel base alloys are direction dependent. Therefore, the orientation of the grains have to be taken into account. Orientations can be described as rotations. For this purpose we use a reference orientation, e.g., a grain where the axes of the unit cell are parallel to the coordinate axes. The orientation is then given by the rotation that maps the reference grain onto the grain that is considered (Figure 3.2). In this section, we follow [47, 19]. To describe rotations mathematically, we recap the definition of a group.

Definition 3.17 (Group)**.** *Let* Γ *be a set and* $\cdot : \Gamma \times \Gamma \to \Gamma$ *a binary operation. The pair* $(\Gamma, \cdot)$ *is called group if* $\cdot$ *satisfies the following properties:*

(i) $a \cdot (b \cdot c) = (a \cdot b) \cdot c \quad \forall a, b, c \in \Gamma$ *(Associativity)*

(ii) $\exists e \in \Gamma$ *such that* $e \cdot a = a \cdot e = a \ \forall a \in \Gamma$ *(Existence of identity)*

(iii) $\forall a \in \Gamma \ \exists a^{-1} \in \Gamma$ *such that* $a^{-1} \cdot a = a \cdot a^{-1} = e$ *(Existence of inverse)*

Definition 3.18 (Hausdorff space)**.** *A topological space* (X, τ) *is called Hausdorff, if* $\forall x, y \in X \ \exists U, V \in \tau$ *with* $x \in U$ *and* $y \in V$ *such that* $U \cap V = \emptyset$.

We now define a topological group.

Definition 3.19 (Topological Group)**.** *Let* $(\Gamma, \cdot)$ *be a group and further let* Γ *be a topological space.* $(\Gamma, \cdot)$ *is called a topological group if the mappings,*

$$\begin{aligned} \Gamma \times \Gamma \ni (a, b) \mapsto ab \in \Gamma, \\ \Gamma \ni a \mapsto a^{-1} \in \Gamma \end{aligned} \tag{3.61}$$

are continuous. Here $\Gamma \times \Gamma$ *is provided with the product topology.*

If we have a Group with the Hausdorff topology, then it is called locally compact if each point $x \in \Gamma$ has a compact neighborhood.

The three-dimensional rotations form the special orthogonal group over $\mathbb{R}^3$, i.e., SO(3), which is defined as follows.

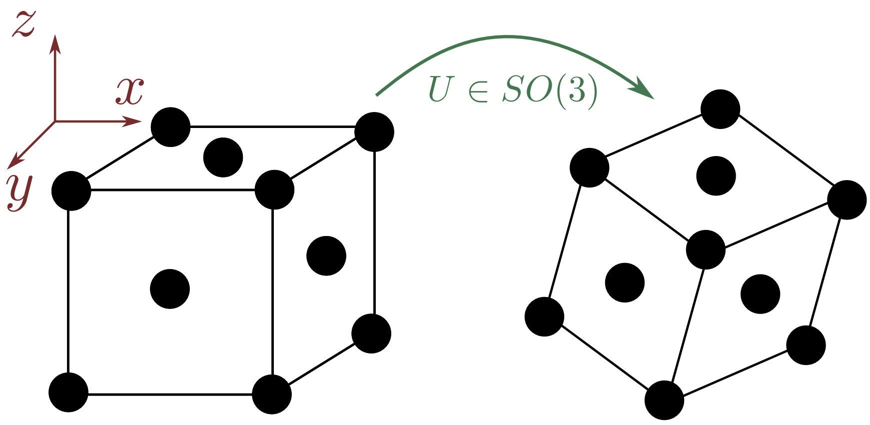

Figure 3.2: Orientation of an FCC crystal represented by a three-dimensional rotation.

Definition 3.20 (Group SO(3))**.** *The group on* $R \subset \mathbb{R}^{3\times 3}$ *with* $R = \{U | U \in \mathbb{R}^{3\times 3} : UU^T = U^T U = \mathbb{1}, \det(U) = 1\}$ *and the usual matrix multiplication is called the special orthogonal group* SO(3)*. It represents the rotations in* $\mathbb{R}^3$*.*

There are many ways to describe a three-dimensional rotation. One particular possibility is obviously directly with a matrix $U \in \mathrm{SO}(3)$. In material science, orientations are often specified by Miller indices, where orientations are specified using intersections between crystal planes and coordinate axes (compare Section 2.2.1). This notation has the disadvantage that transformations and calculations with it are impractical.

Therefore, we focus here on two different notations. The first method, that is although often used are the Euler angles. Euler's angles are a triplet of angles each representing a rotation around a coordinate axis. There are different ways how the rotations are executed. On the one hand, the axes around which the rotations are executed differ and on the other hand intrinsic or extrinsic rotations are executed. Performing extrinsic rotations means that there is a fixed global coordinate system and the rotations are executed around these fix axes. In the case of intrinsic rotations, each rotation is performed around the axes defined by the previous rotations. Here, we use the Euler angles with the Bunge convention.

Definition 3.21 (Euler angles Bunge)**.** *The triplet* $\mathcal{E} := (\varphi_1, \vartheta, \varphi_2) \in [0, 2\pi] \times [0, \pi] \times [0, 2\pi]$ *is called Euler angles in the Bunge convention. The first intrinsic rotation* $g^Z_{\varphi_1}$ *is performed around the* Z*-axis, the second angle*

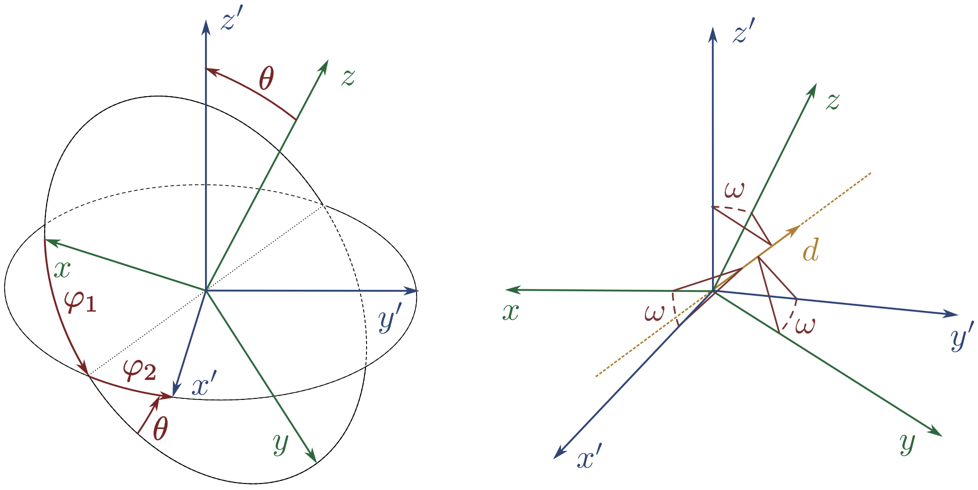

(a) Rotation parametrized by Euler angles in the Bungee convention.

(b) Rotation given by axis d and angle ω.

Figure 3.3: Different notations for rotations. Initial coordinate system in green, coordinate system after rotation in blue.

g_θ^X *around the* X*-axis and the third* $g_{\varphi_2}^Z$ *again around the* Z*-axis. Therefore the full rotation is given by:*

$$U(\mathcal{E}) = U(\varphi_1, \theta, \varphi_2) := g_{\varphi_2}^Z \cdot g_\theta^X \cdot g_{\varphi_1}^Z. \tag{3.62}$$

The parametrization of a rotation with Euler angles is illustrated in Figure 3.3a. For the Euler rotations in definition 3.21 we obtain:

$$g_{\varphi_1}^Z = \begin{pmatrix} \cos(\varphi_1) & \sin(\varphi_1) & 0 \\ -\sin(\varphi_1) & \cos(\varphi_1) & 0 \\ 0 & 0 & 1 \end{pmatrix}, \tag{3.63}$$

$$g_\theta^X = \begin{pmatrix} 1 & 0 & 0 \\ 0 & \cos(\theta) & \sin(\theta) \\ 0 & -\sin(\theta) & \cos(\theta) \end{pmatrix}, \tag{3.64}$$

$$g_{\varphi_2}^Z = \begin{pmatrix} \cos(\varphi_2) & \sin(\varphi_2) & 0 \\ -\sin(\varphi_2) & \cos(\varphi_2) & 0 \\ 0 & 0 & 1 \end{pmatrix}. \tag{3.65}$$

With this elementary rotations we can calculate the rotation matrix via

$$U(\varphi_1,\theta,\varphi_2) = \begin{pmatrix} c(\varphi_1)c(\varphi_2) - s(\varphi_1)s(\varphi_2)c(\theta) & s(\varphi_1)c(\varphi_2) + c(\varphi_1)s(\varphi_2)c(\theta) & s(\varphi_2)s(\theta) \\ -c(\varphi_1)s(\varphi_2) - s(\varphi_1)c(\varphi_2)c(\theta) & -s(\varphi_1)s(\varphi_2) + c(\varphi_1)c(\varphi_2)c(\theta) & c(\varphi_2)s(\theta) \\ s(\varphi_1)s(\theta) & -c(\varphi_1)s(\theta) & c(\theta) \end{pmatrix}, \tag{3.66}$$

where c stands for cosin and s for sin. It is easy to see, that the mapping from angles to rotation matrices in the case $\theta = 0$ is singular, then the rotation is only determined by the sum $\varphi_1 + \varphi_2$.

The conversion $\mathcal{E}(U)$ from a rotation matrix U to Euler angles is straight forward, θ is directly given via

$$\theta = \arccos(u_{33}). \tag{3.67}$$

For $\theta > 0$ we get

$$\varphi_1 = -\arctan\left(\frac{u_{31}}{u_{32}}\right) \tag{3.68}$$

$$\varphi_2 = \arctan\left(\frac{u_{13}}{u_{23}}\right). \tag{3.69}$$

If $\theta = 0$ we set $\varphi_2 = 0$ and obtain

$$\varphi_1 = \arccos(u_{11}). \tag{3.70}$$

The second notation that we introduce for rotations is by a rotation axis which is represented by a unit vector $d \in \mathbb{R}^3$ and a rotation angle $\omega \in [0, 2\pi]$, see Figure 3.3b. This parametrization is especially useful for transforming geometries. Let $\hat{\omega}_i := d_i(1-\cos(\omega)), i = 1, 2, 3$, then for a rotation $\omega \in [0, 2\pi]$ around the axis $d \in \mathbb{R}^3$ the associated rotation matrix is given by

$$U(\{d,\omega\}) = \begin{pmatrix} d_1\hat{\omega}_1 + c(\omega) & d_2\hat{\omega}_1 - n_3 s(\omega) & d_3\hat{\omega}_1 + d_2 s(\omega) \\ d_1\hat{\omega}_2 + d_3 c(\omega) & d_2\hat{\omega}_2 + c(\omega) & d_3\hat{\omega}_2 - d_1 s(\omega) \\ d_1\hat{\omega}_3 - d_2 c(\omega) & d_2\hat{\omega}_3 + d_1 s(\omega) & d_3\hat{\omega}_3 + c(\omega) \end{pmatrix}, \tag{3.71}$$

where again c stands for the cosin and s for sin.

3.2.1 Symmetries of the Compliance Tensor

The slip systems of an FCC crystal are symmetric with respect to the unit cell of the FCC lattice. Therefore, the crystal lattice, which is aligned with the coordinate axis, is invariant under rotations with an angle $\omega \in \{2\pi/3, 4\pi/3\}$ around the axis $d \in D_{2\pi/3} := \{1/\sqrt{3}(1,1,1), 1/\sqrt{3}(-1,1,1), 1/\sqrt{3}(1,-1,1), 1/\sqrt{3}(1,1,-1)\}$ and $\omega = \pi$ around $d \in D_{\pi} := \{(1,0,0), (0,1,0), (0,0,1)\}$. The same rotational symmetries hold for the compliance tensor $S = (s_{ijkl})_{i,j,k,l} \in \mathbb{R}^{3\times3\times3\times3}$ of an FCC crystal. From Section 2 we know that if the lattice of the crystal is aligned with the coordinate axis, then for the entries of the compliance tensor it follows that

$$s_{ijkl} = \begin{cases} S_{11} & \text{for } i = j = k = l, \\ S_{12} & \text{for } i = j \wedge k = l \wedge i \neq k, \\ S_{44} & \text{for } i \neq j \wedge (i = k \wedge j = l \vee i = l \wedge j = k), \\ 0 & \text{else .} \end{cases} \tag{3.72}$$

Under a rotation U, it holds for the tensor S that

$$s'_{ijkl} = \sum_{p=1}^{3}\sum_{q=1}^{3}\sum_{r=1}^{3}\sum_{t=1}^{3} u_{ip}u_{jq}u_{kr}u_{lt}s_{pqrt} \quad i,j,k,l \in \{1,2,3\}, \tag{3.73}$$

see, e.g., [55]. If we plug in the values from (3.72), this simplifies to

$$s'_{ijkl} = a_{11}S_{11} + a_{12}S_{12} + a_{44}S_{44}, \tag{3.74}$$

where,

$$a_{11} := u_{i1}u_{j1}u_{k1}u_{l1} + u_{i2}u_{j2}u_{k2}u_{l2} + u_{i3}u_{j3}u_{k3}u_{l3}, \tag{3.75}$$

$$\begin{aligned} a_{12} := {} & u_{i1}u_{j1}u_{k2}u_{l2} + u_{i1}u_{j1}u_{k3}u_{l3} + u_{i2}u_{j2}u_{k1}u_{l1} + u_{i2}u_{j2}u_{k3}u_{l3} \\ & + u_{i3}u_{j3}u_{k1}u_{l1} + u_{i3}u_{j3}u_{k2}u_{l2}, \end{aligned} \tag{3.76}$$

$$\begin{aligned} a_{44} := {} & u_{i1}u_{j2}u_{k1}u_{l2} + u_{i1}u_{j2}u_{k2}u_{l1} + u_{i2}u_{j1}u_{k1}u_{l2} + u_{i2}u_{j1}u_{k2}u_{l1} \\ & + u_{i1}u_{j3}u_{k1}u_{l3} + u_{i1}u_{j3}u_{k3}u_{l1} + u_{i3}u_{j1}u_{k1}u_{l3} \\ & + u_{i3}u_{j1}u_{k3}u_{l1} + u_{i2}u_{j3}u_{k2}u_{l3} + u_{i2}u_{j3}u_{k3}u_{l2} \\ & + u_{i3}u_{j2}u_{k2}u_{l3} + u_{i3}u_{j2}u_{k3}u_{l2}. \end{aligned} \tag{3.77}$$

With the rotations around the axes $d = (d_x, d_y, d_z) \in D_{2\pi/3}$ the rotation matrices are given by

$$U(\{d, 2\pi/3\}) = \frac{1}{2}\begin{pmatrix} 0 & 3d_xd_y - \sqrt{3}d_z & 3d_xd_z + \sqrt{3}d_y \\ 3d_xd_y + \sqrt{3}d_z & 0 & 3d_yd_z - \sqrt{3}d_x \\ 3d_xd_z - \sqrt{3}d_y & 3d_yd_z + \sqrt{3}d_x & 0 \end{pmatrix}, \tag{3.78}$$

$$U(\{d, 4\pi/3\}) = \frac{1}{2}\begin{pmatrix} 0 & 3d_xd_y + \sqrt{3}d_z & 3d_xd_z - \sqrt{3}d_y \\ 3d_xd_y - \sqrt{3}d_z & 0 & 3d_yd_z + \sqrt{3}d_x \\ 3d_xd_z + \sqrt{3}d_y & 3d_yd_z - \sqrt{3}d_x & 0 \end{pmatrix}, \tag{3.79}$$

and for the rotations around $d \in D_\pi$

$$U(\{d, \pi\}) = \begin{pmatrix} (-1)^{d_x+1} & 0 & 0 \\ 0 & (-1)^{d_y+1} & 0 \\ 0 & 0 & (-1)^{d_z+1} \end{pmatrix}. \tag{3.80}$$

For all of these matrices, it holds that in each row and each column there is only one entry which is non-zero. The entries that are non-zero are either 1 or -1. Therefore, we get with equations (3.75), (3.76) and (3.77)

$$a_{11} = \begin{cases} 1 & \text{for } i = j = k = l, \\ 0 & \text{else }, \end{cases} \tag{3.81}$$

$$a_{12} = \begin{cases} 1 & \text{for } i = j \wedge k = l \wedge i \neq k, \\ 0 & \text{else }, \end{cases} \tag{3.82}$$

$$a_{44} = \begin{cases} 1 & \text{for } i \neq j \wedge (i = k \wedge j = l \vee i = l \wedge j = k), \\ 0 & \text{else }. \end{cases} \tag{3.83}$$

Finally, we can conclude with equation (3.74) that

$$s'_{ijkl} = s_{ijkl}. \tag{3.84}$$

The rotational symmetries of the unit cell hold for the compliance tensor (and therefore the stiffness tensor as well) of an FCC crystal. The slip systems of an FCC crystal depend directly on the structure of the unit cell. Accordingly, the same symmetrical properties hold for the slip systems.

3.2.2 Haar measure

We assume that the orientation of the grains is randomly distributed. We suppose that this distribution is translation invariant. So first, for $a \in \Gamma$ we define a left translation $L(a)$ and a right translation $R(a)$ as follows

$$L(a) : \Gamma \to \Gamma, \; L(a)x := xa, \; \text{for } x \in \Gamma, \tag{3.85}$$

$$R(a) : \Gamma \to \Gamma, \; R(a)x := xa, \; \text{for } x \in \Gamma. \tag{3.86}$$

In the following, $C(\mathbb{R}^p)$ is used to denote the set of functions $f : \mathbb{R}^p \to \mathbb{R}$ which are continuous and $C_C(\mathbb{R}^p)$ for the functions $f \in C(\mathbb{R}^p)$ that have a compact support.

Definition 3.22.

(i) A linear form $I : C_C(\Gamma) \to \mathbb{R}$ is called left invariant, if

$$I(f \circ L) = I(f), f \in C_C(\Gamma). \tag{3.87}$$

(ii) A measure $\nu : \mathcal{B}(\Gamma) \to [0, \infty]$ is called left invariant, if

$$\nu(yB) = \nu(B), B \in \mathcal{B}(\Gamma), y \in \Gamma, \tag{3.88}$$

where $yB := \{y \cdot b : b \in B\}$.

(iii) A linear form $I : C_C(\Gamma) \to \mathbb{R}$ is called positive, if for $f \in C_C(\Gamma)$, with $f \geq 0$ holds, that $I(f) \geq 0$.

Theorem 3.23. *Let Γ be a locally compact Hausdorff topological group. Further, let $I : C_C(\Gamma) \to \mathbb{R}$ a left invariant positive linear form, then there exist one and only one Radon measure $\nu : \mathcal{B}(\Gamma) \to [0, \infty]$ such that*

$$I(f) = \int_\Gamma f \, d\nu, \; f \in C_C(\Gamma), \tag{3.89}$$

the measure ν *is left invariant. Reversely, to each left invariant Radon measure* $\nu : \mathcal{B}(\Gamma) \to [0, \infty]$ *corresponds to a left invariant positive linear form* $I : C_C(\Gamma) \to \mathbb{R}$ *by equation (3.89).*

Proof. For the proof we refer to [19]. ☐

Theorem 3.24 (Haar Integral)**.** *Let* Γ *be a locally compact Hausdorff topological group, then there exists a left invariant positive linear form* $I : C_C(\Gamma) \to \mathbb{R}, I \neq 0$. *I is uniquely determined up to a constant factor. I is called left Haar integral of* $C_C(\Gamma)$.

Proof. The proof can be found in [19]. ☐

Theorem 3.25 (Haar Measure)**.** *Let* Γ *be a locally compact Hausdorff topological group. Then there exists a left invariant Radon-measure* $\mu : \mathcal{B}(\Gamma) \to [0, \infty], \mu \neq 0$. *Furthermore,* μ *is uniquely determined up to a constant factor.* μ *is called the left Haar measure.*

Proof. The theorem follows immediately from (3.23) and (3.24). ☐

A Radon measure is finite on compact sets, therefore it follows directly

Corollary 3.26. *Let* Γ *be a compact Hausdorff topological group. Then there exist a left invariant uniquely determined probability measure* $\mu : \mathcal{B}(\Gamma) \to [0, 1]$.

This corollary ensures the existence and uniqueness of a translation invariant probability measure on the group of rotations SO(3). We simply call this measure the Haar measure on SO(3) in the following.

3.3 Crack Initiation Process

In the following, we want to model the LCF crack initiation of mechanical component as a stochastic process. The component can be described as a bounded, open domain $\Omega \subset \mathbb{R}^3$ with a Lipschitz boundary $\partial\Omega$. The time domain $\mathcal{T}$ is either $\mathbb{R}_+$ if we use the natural time or $\mathbb{N}_0$ if load cycles are considered. As we only consider surface cracks, we define the configuration space of crack initiation as the product space of the time axis and surface of the component $\mathcal{C} := \mathcal{T} \times \partial\Omega$. Note that we follow the crack initiation process proposed in [63, 30].
We assume in the following that $\mathcal{C}$ is assigned the standard metric topology.

Definition 3.27 (Counting Measurs)**.** *Let $\mathcal{B}(\mathcal{C})$ be the Borel σ-algebra of $\mathcal{C}$ and $\mathcal{R} = \mathcal{R}(\mathcal{C})$ be the set of all Radon measures on $\mathcal{C}$. A Radon measure $\gamma \in \mathcal{R}$ is called counting measure if $\gamma(B) \in \mathbb{N}_0$ for all $B \subseteq \mathcal{C}$ measures and bounded. The set of all counting measures on $\mathcal{C}$ is denoted with $\mathcal{R}_{\mathcal{C}}$.*

According to [44] it holds, that the restriction of a counting measure $\gamma \in \mathcal{R}(\mathcal{C})$ to $B \in \mathcal{B}(\mathcal{C})$ can be written as

$$\gamma_{|B} = \sum_{i=1}^{n} b_j \delta_{c_j},\ c_j \in \mathcal{C}, c_i \neq c_j, i \neq j \text{ and } b_j \in \mathbb{N}_0. \tag{3.90}$$

This decomposition is unique up to order. The Radon counting measure γ is called simple, if $b_j = 1$ for $j = 1, \dots, n$ for al $B \in \mathcal{B}(\mathcal{C})$.
Now let $f \in C_C(\mathcal{C})$ we then denote the σ-algebra on $\mathcal{R}$ which is generated by the mapping $\gamma \to \int_{\mathcal{C}} f \, d\gamma$ with $\mathcal{N}(\mathcal{R}_{\mathcal{C}})$.
With this we can define a point process as follows.

Definition 3.28. *Let $(X, \mathcal{A}, P)$ be a probability space.*

(i) A measurable mapping $\gamma : (X, \mathcal{A}, P) \to (\mathcal{R}_{\mathcal{C}}, \mathcal{N}(\mathcal{R}_{\mathcal{C}}))$ is called a point process.

(ii) If $\gamma(\,\cdot\,, \omega)$ is simple for P-almost all $\omega \in X$, the point process is called simple.

(iii) If $P(\gamma(\{c\}) > 0) = 0$ for all $c \in \mathcal{C}$, the point process is non-atomic.

(iv) Let $B_1, \dots, B_n \in \mathcal{B}(\mathcal{C})$ mutually disjoint, if the random variables $\gamma(\{B_1\}), \dots, \gamma(\{B_n\})$ are independent, the point process has independent increments.

Next, we introduce a special point process where the number of events are Poisson distributed in bounded sets of σ-algebra.

Definition 3.29 (Poisson Point Process)**.** *Let γ be a point process on $(X, \mathcal{A}, P)$, if there exists a unique Radon measure $\rho \in \mathcal{R}$, such that*

$$P(\gamma(B) = n) = e^{\rho(B)} \frac{\rho(B)^n}{n!} \quad \forall B \in \mathcal{B}(\mathcal{C}) \text{ bounded}, \tag{3.91}$$

then γ is a Poisson point Process. ρ is called the intensity measure of γ.

Proposition 3.30. *Let γ be non-atomic, simple point process with independent increments, then γ is a Poisson point process.*

Proof. Is proven in Corollary 7.4 of [43]. ☐

Now we can introduce the crack initiation process. For the process we consider that the probability that a crack originates at an exact location on the surface $x \in \partial\Omega$ should be zero. Further we assume that two cracks that initiate at the same location and time are considered as the same crack. In addition, suppose that a surface crack has only a negligible influence on the stress field on the component surface. This assumption is justified by the fact that the LCF cracks that we consider are small compared to the component surface. These properties are leading to the following definition

Definition 3.31 (Crack initiation Process)**.** *A crack initiation process γ is a simple, non-atomic point process on $\mathcal{C}$ with independent increments.*

We suppose now that the first apparent of an LCF crack leads to failure.

Definition 3.32 (Failure Time)**.** *The failure time $T : X \to \mathcal{T}^*$ for the crack initiation process γ on $\mathcal{C}$ is given by the random variable*

$$T = \mathfrak{t}(\gamma) = \min\{t > 0 : \gamma(\mathcal{C}_t) > 0\}, \tag{3.92}$$

where $\mathcal{C}_t := \{(s, x) \in \mathcal{C} : s \leq t\}$ and $\mathcal{T}^* = \mathcal{T} \cup \{\infty\}$.

From the upper continuity of Radon measures and the right continuity of $t \to \gamma(\mathcal{C}_t)$ it follows that the minimum in (3.92) is attained.
Due to proposition 3.30 a crack initiation process is a Poisson point process.

Theorem 3.33. *Let γ be a crack initiation process on $\mathcal{C}$. Then following statements hold.*

(i) The distribution function F_T of the failure time T associated with the crack initiation process γ is given by $F_T(t) = 1 - \exp(-H(t))$ with cumulative hazard function $H(t) := \rho(\mathcal{C}_t)$.

(ii) If $\rho(\mathcal{C}) = \infty$, then $P(T = \infty) = 0$ and thus T can be modified to $T : (X, \mathcal{A}) \to (\mathcal{T}, \mathcal{B}(\mathcal{T}))$.

Proof. (i) With proposition 3.30 it follows that,

$$F_T(t) = 1 - P(T > t) = 1 - P(\gamma(\mathcal{C}_t) = 0) = 1 - e^{-\rho(\mathcal{C}_t)} = 1 - e^{-H(t)}. \tag{3.93}$$

(ii) Let $\rho(\mathcal{C}) = \infty$, as Radon measures are lower continuous we obtain $H(t) \to \infty$ for $t \to \infty$. Therefore, $S(t) = \exp(-H(t)) = P(T > t) \to 0$ for $t \to \infty$. With the lower continuity of P it holds that $T < \infty$ P almost-sure, and therefore we can redefine $T = 0$ on the null set $\{T = \infty\}$ without changing the probability law on T. □

In the following we suppose that the intensity measure ρ of the crack initiation process γ is absolutely continuous with respect to $dtdA$, where dA is the Lebesgue measure on $\partial\Omega$. We use this assumption because we presuppose that in a finite region and time only finite cracks can initiate. With these considerations we can gain for the cumulative hazard rate

$$H(t) = \int_0^t h(s)\, ds, \tag{3.94}$$

where $h(t)$ is the hazard function. It further holds that

$$h(t) = \int_{\partial\Omega} \varrho(t, \sigma(x))\, dA, \text{ for almost every } t \in \mathcal{T}, \tag{3.95}$$

here the hazard density $\varrho(t, \sigma(x))$ is the Radon-Nikodyn derivative of ρ with respect to $dtdA$. $\sigma(x)$ is the stress at $x \in \partial\Omega$.

We now consider a decomposition of the surface area $\partial\Omega$ in m mutually disjoint subsets

$$\partial\Omega = \bigcup_{i=1}^{m} A_i. \tag{3.96}$$

The crack initiation process has independent increments, therefore the hazard function can be written as

$$h(t) = \sum_{i=1}^{m} h_{A_i}(t), \tag{3.97}$$

with

$$h_{A_i}(t) = \int_{A_i} \varrho(t, \sigma(x))\, dA. \tag{3.98}$$

Let now $A \subseteq \partial\Omega$ be a region on the surface where the load is almost constant, $\sigma(x) \approx \sigma_A, x \in A$. We subdivide A in m subsets A_j with equal surface size $|A_j| = |A|/m$. With the assumption that the stress is almost constant we get that $h_{A_j} \approx h_{A_k}$ for $j, k = 1, \ldots, m$. Consequently, we obtain

$$h_A(t) = \sum_{j=1}^{m} h_{A_j}(t) \approx m \cdot h_{A_1} = \frac{|A|}{|A_1|} h_{A_1}. \tag{3.99}$$

For the hazard density we obtain with $m \to \infty$

$$\varrho(t, \sigma_A) = \lim_{m\to\infty} \frac{h_{A_1}(t)}{|A_1|}, \text{ thus } h_A(t) \approx |A| \cdot \varrho(t, \sigma_A). \tag{3.100}$$

With equation (3.94) we can define the surface dependent cumulative hazard on the region A as

$$H_A(t) := \int_0^t h_A(s)\, ds \approx |A| \int_0^t \rho(t, \sigma)\, ds = |A| \cdot H(t, \sigma_A). \tag{3.101}$$

In section 7 we apply the cumulative hazards to an actual turbine blade. We use a FE-model of a blisk blade under realistic loading conditions as an example. With a FE-mesh discretization of the component we calculate the cumulative hazard on the surface as follows,

$$\begin{aligned} H(t) &= \sum_{F\in\mathcal{N}_h} \int_F H(\sigma(x), t)\, dA \\ &= \sum_{F\in\mathcal{N}_h} H\left(\sigma(\hat{T}_{K(F),t}(\hat{x}))\right) \sqrt{\det g_F(\hat{x})}\, d\hat{A} \\ &\approx \sum_{F\in\mathcal{N}_h} \sum_{l=1}^{q^F} \hat{\omega}_l^F H\left(s, \sigma(\hat{T}_{K(F)}(\hat{x}^{F_l}))\right) \sqrt{\det g_F(\hat{x}^{F_l})} \\ &=: \hat{H}(t). \end{aligned} \tag{3.102}$$

Therefore, we can approximate the probability of Failure of the whole component with

$$F_T(t) = 1-\exp\left(-\int_0^t h(s)\ ds\right) = 1-\exp\left(H(t)\right) \approx 1-\exp\left(\hat{H}(t)\right). \quad (3.103)$$

4. Epidemiological Percolation Model Uniaxial Stress

In this section, we present a probabilistic LCF failure model for polycrystalline metals under uniaxial loading. For this purpose, we use a basic percolation model as introduced, e.g., in [52, 50]. We extend this model with an infection function. The infection function models the interaction between a crack grain and the neighboring grains. Note that this model has been already published in [37].

4.1 Single Grain Crack Initiation Times

We assume that the crack initiation in the single grains is driven by the shear stress in the slip systems and therefore by the Schmid factors.

4.1.1 Random Schmid Factors

Let us consider a grain with an FCC crystal structure. This grain is characterized by an orientation $U \in SO(3)$. The rotation matrix U maps the lattice of a crystal with its unit cell aligned with the coordinate axis onto the lattice of the given grain. By applying the rotation matrix U, we can obtain the slip directions and normals of the grain with orientation U by transforming the slip systems of the grain with a standard lattice

$$\begin{aligned} n_i(U) &= U n_i \\ s_{ij}(U) &= U s_{ij}. \end{aligned} \tag{4.1}$$

An example for a rotation acting on an FCC lattice cell is shown in Figure 4.1. To describe the mechanical behavior of the grain, we need to consider its

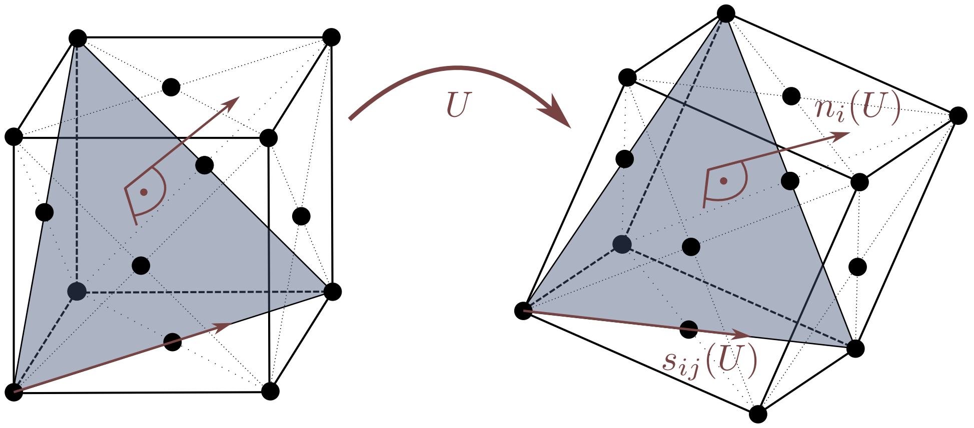

Figure 4.1: Rotation of a slip system.

stiffness tensor C. The components of this tensor, denoted as $C_{ijkl}(U)$, can be obtained by

$$C_{ijkl}(U) = \sum_{p,q,r,s=1}^{3} U_{ip}U_{jq}U_{kr}U_{ls}C_{pqrs}. \tag{4.2}$$

We now consider a given isotropic strain ε_{iso} that acts uniformly over the entire surface area. By applying the rotated stiffness tensor, we can determine the anisotropic stress acting on the grain using Hook's law

$$\sigma(U)_{ani} = C(U)\varepsilon_{iso}. \tag{4.3}$$

To calculate the shear stress on the grain with a specific orientation U, we project the anisotropic stress onto the slip systems using equation (2.50)

$$\tau_{ij}(U) = n_i(U) \cdot \sigma(U)_{ani} \cdot s_{ij}(U). \tag{4.4}$$

Moreover, the Schmid factors for each slip system, denoted as $m_{ij}(U)$, can be obtained using equation (2.53)

$$m_{ij}(U) = \frac{\tau_{ij}(U)}{\sqrt{3/2} \cdot \sigma_{vM}}. \tag{4.5}$$

Here, σ_{vM} represents the von Mises equivalent stress of the isotropic stress tensor σ_{iso}.

As mentioned in Section 2, we consider only the highest Schmid factor for crack initiation. Therefore, we take the maximum over all twelve slip

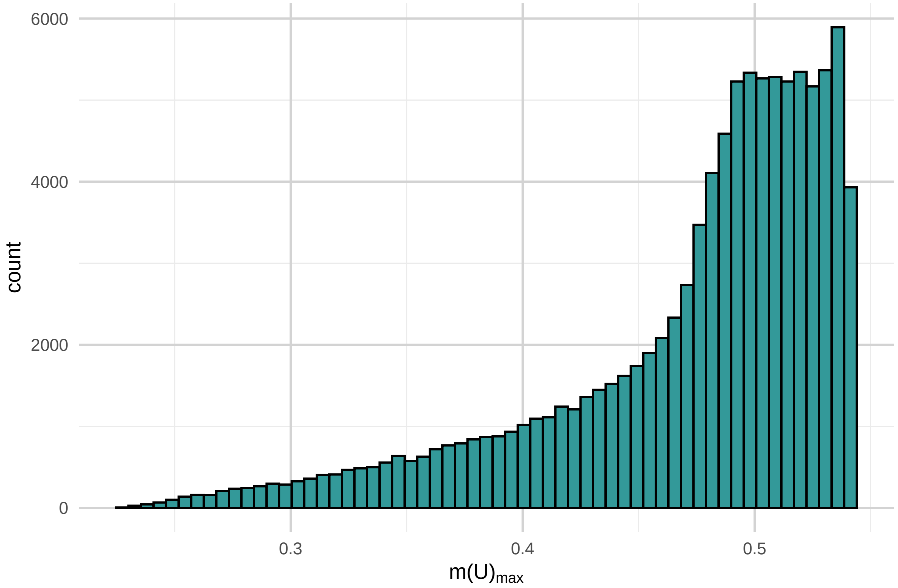

Figure 4.2: Histogram of $m_{\max}(U)$ with 10^5 random orientated grains sampled from the Haar measure on $SO(3)$ for INC738 at $850°C$: $C_{11} =$ 226GPa, $C_{12} = 161$GPa, $C_{44} = 99$ GPa.

systems of the FCC crystal

$$m_{\max}(U) = \max_{i,j} \left(m_{ij}(U)\right). \tag{4.6}$$

If we now assume that $U \in SO(3)$ is randomly distributed, then both the direction and normals of the slip systems, as well as the anisotropic stress, become random variables. Considering this, the maximum Schmid factors will also be randomly distributed.

The distribution of the maximum Schmid factors for randomly sampled orientations from the Haar measure is shown in the histogram in Figure 4.2. Notably, the observed Schmid factors surpass the previously stated maximum value of 0.5 mentioned in Section 2. This deviation is due to the transformation from isotropic to anisotropic stress in equation (4.3). The material parameters, which we use in the following, are for the nickel-base super alloy INC738 at $850°C$: $C_{11} = 226$GPa, $C_{12} = 161$GPa, $C_{44} = 99$ GPa. They can be found in [4]

4.1.2 Random Crack Initiation Times

We now use the random Schmid factor to gain a random crack initiation time N_i under cyclic loading with a given strain amplitude ε_a.

Therefore, we again consider a single grain with a random orientation $U \in SO(3)$. We apply the inverse of the Ramberg Osgood equation to the strain amplitude and weight it with the random maximal Schmid factor

$$\mathrm{RO}^{-1}(\varepsilon_a) \cdot \frac{m_{\max}(U)}{\lambda}, \tag{4.7}$$

this gives the elastic plastic stress that acts in the slip system with the highest Schmid factor. Here, λ is the expected value $\mathbb{E}_U\left[m_{\max}(U)\right]$, which is used as a scaling factor.

This stress can be transformed back to a strain via the Ramberg Osgood equation, then the inverse of Coffin Manson Basquin equation is applied

$$N_i(U) = \mathrm{CMB}^{-1}\left(\mathrm{RO}\left(\mathrm{RO}^{-1}(\varepsilon_a) \cdot \frac{m_{\max}(U)}{\lambda}\right)\right), \tag{4.8}$$

which leads to a probabilistic crack initiation time for the grain.

4.2 Percolation Model

We later want to fit and validate our model with experimental LCF failure data from Section 2.7. The experiments are performed with cylindrical specimens. The surface area is therefore given by the height h_s and the radius r_s of the gauge area of the specimen.

For a given number n of grains the polycrystalline surface is modeled with a Voronoi tessellation. We assume that the seeds $(x_g, z_g) \in [0, 2\pi r_s] \times [0, h_s], g \in G = \{1, \ldots, n\}$ are uniformly distributed. The Voronoi cells represent the single grains. A Voronoi tessellation with 30 random seeds is shown in Figure 4.3a.

Each grain g has a random orientation, parametrized by the Euler angles $\mathcal{E}^g := (\varphi_1^g, \theta^g, \varphi_2^g)$. The orientations are sampled according to the Haar

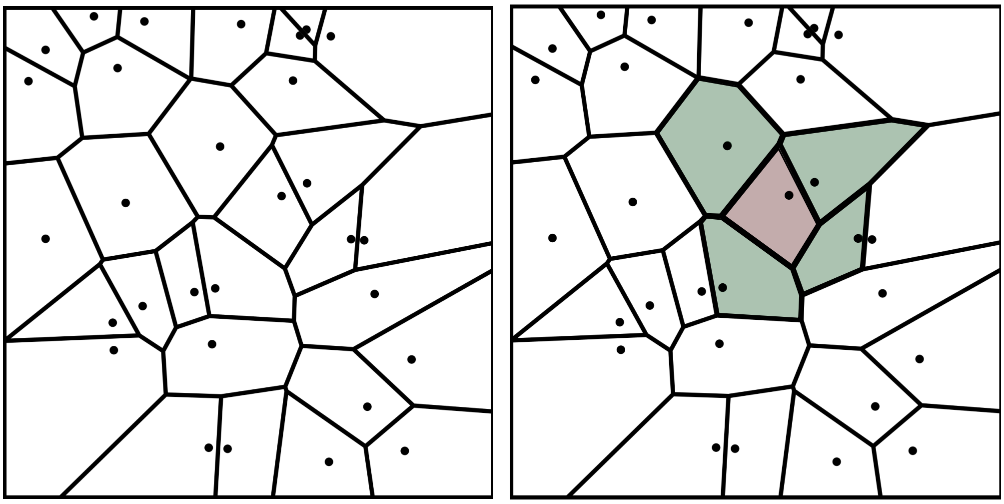

(a) Voronoi tessellation with 30 seeds.

(b) Grain (red), neighborhood (green).

Figure 4.3: Voronoi tessellation

measure on $SO(3)$. With equation (3.66) we can determine the rotation matrix U^g. Furthermore, with equation (4.8) the initial crack time $N_i(U^g)$ for each single grain is calculated.

With these initiation times we can determine the first grain that cracks and the corresponding crack time by taking the minimum,

$$g_1 = \arg\min_{g \in G} N_i(U^g), \quad N_i^1 = N_i(U^{g_1}). \tag{4.9}$$

A crack in a grain has an influence on the stress field around the grain. We want to address this change in stress by an infection function. We assume that only the grains which are directly adjacent to the cracked one are effected. Such a neighborhood of a grain is shown in Figure 4.3b. Let $G_k \subset G$ be the set of grains that have a common boundary with the grain g_k, we refer to them as the neighborhood of g_k. If a crack initiates in grain g_k at load cycle $N_i^{g_k}$, then we calculate the new shear stress in the slip systems in the neighborhood of g_k by an infection function

$$\bar{\tau}_{ij}^{g_l} = f(\tau_{ij}^{g_l}, \mathcal{E}^{g_l}, \mathcal{E}^{g_k}), \; g_l \in G_k. \tag{4.10}$$

The modelling of the infection function is described in detail in Section 4.3. With the new shear stress the resulting Schmid factors $\bar{m}_{ij}^{g_l}$ after infection

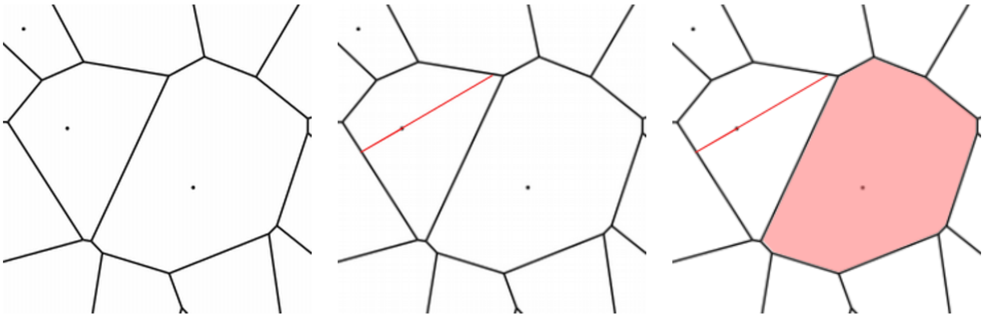

(a) The neighborhood just contains grains without cracks.

(b) The cracked adjacent grain changes the Schmid factors.

(c) The new crack initiation is calculated via a Miners rule.

Figure 4.4: Procedure of the infection.

are calculated with equation (2.53).

For the new crack times of the grain $g_l \in G_k$ we use Miner's rule see Section 2.5.6

$$1 = \frac{N_i^{g_k}}{N_i^{g_l}} + \frac{\bar{N}_i^{g_l} - N_i^{g_k}}{N_i(\max(\bar{m}_{ij}^{g_l}))} \tag{4.11}$$

here the first summand is the fraction of the lifetime used up to the formation of a crack in the neighboring grain. With equation (4.11), it follows that the new crack initiation time for the infected grains is given by

$$\bar{N}_i^{g_l} = \left(1 - \frac{N_i^{g_k}}{N_i^{g_l}}\right) N_i(\max(\bar{m}_{ij}^{g_l})) + N_i^{g_k}. \tag{4.12}$$

4.3 Uniaxial Infection Function

To quantify the change in shear stress that a crack induces in an adjacent grain, we apply FEM simulations. In these simulations we model two adjacent grains with orientations $\mathcal{E}_l, \mathcal{E}_r$ parametrized by Euler angles. For each pair of orientations we run two simulations one where both grains are intact and another where the left grain is cracked.

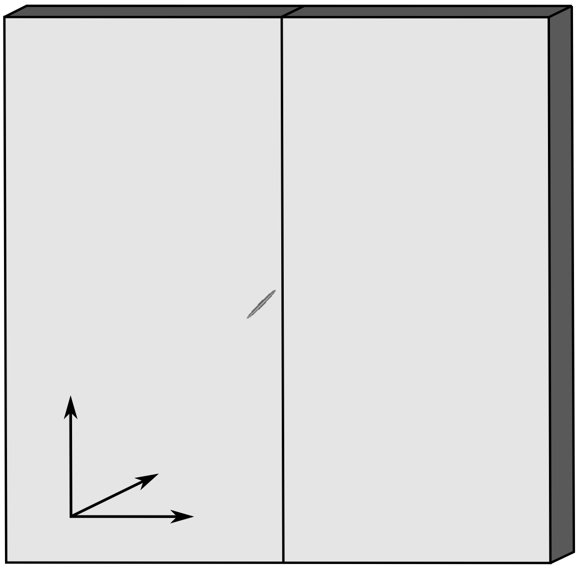

Figure 4.5: Geometry for the infection model with cracked left grain.

4.3.1 Geometry and Boundary Conditions

The geometry in the simulations is a cuboid with edge lengths of $d_x = d_z = 10\ cm$ and $d_y = 5\ cm$. The grain boundary is perpendicular to the x-axis in the middle of the cuboid. For the cracked geometry (Figure 4.5) we use a spheroid crack. The direction of the crack depends on the orientation of the grain. We assume that the slip system with the highest Schmid factor is cracked. So the direction is the projection of the slip system direction in the $x - z$-plane. A detailed illustration of the crack is shown in Figure 4.6. The minimal distance from the crack to the grain boundary is $d_c = 0.15\ mm$. We choose a crack height of $c_h = 0.15\ mm$ and $c_l = 1.5\ mm$ for the length of the crack.

As boundary condition we apply an uniaxial stress σ_z in z-direction

$$\sigma_z = \begin{pmatrix} 0 & 0 & 0 \\ 0 & 0 & 0 \\ 0 & 0 & 1 \end{pmatrix}. \tag{4.13}$$

The geometry is discretized using quadratic tetrahedral elements. Shear stress within the right grain is evaluated within a small volume $B \subset \Omega$. To achieve this, we intersect the right grain with a spherical shape. The sphere's center corresponds to the point along the grain boundary nearest

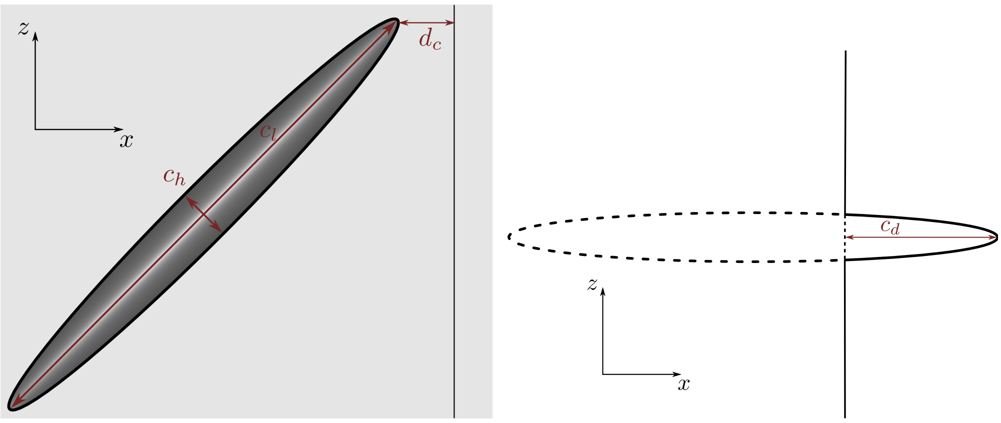

(a) Top view of the crack and the grain boundary.

(b) Cross section of the crack.

Figure 4.6: Geometry of the spheroid crack

to the crack, as illustrated in Figure 4.7. We then take the average shear stress in the resulting quarter sphere B

$$\bar{\tau}_{ij} = \frac{1}{|B|} \int_B \tau_{ij} dx. \tag{4.14}$$

With the finite element discretization, the average shear stress is approximated via

$$\bar{\tau}_{ij} \approx \sum_{K \in \mathcal{T}_h} W_K \sum_{l=1}^{q^K} \hat{\omega}_l^K \tau_{ij}(T_K(\hat{x}_l)) \det T_K(\hat{x}), \tag{4.15}$$

where W_k is the fraction of the volume of element K that lies within the quarter sphere.

4.3.2 Numerical Results

The simulation toolchain follows this sequence: the programming language `R` [58] is employed for both pre-processing and post-processing stages. During pre-processing, the tasks involve rotating the stiffness sensors, constructing the geometry, and evaluating the volume fractions denoted as W_k. For the volume fractions the python package `overlap` [66] is used, embedded into R with the R-library `reticulate` [70]. Then the FE mesh is generated with `Gmsh` [25]. The solver for the FEM simulations is `CalculiX`.

The mesh of the fractured geometry is composed of around 210,000 nodes

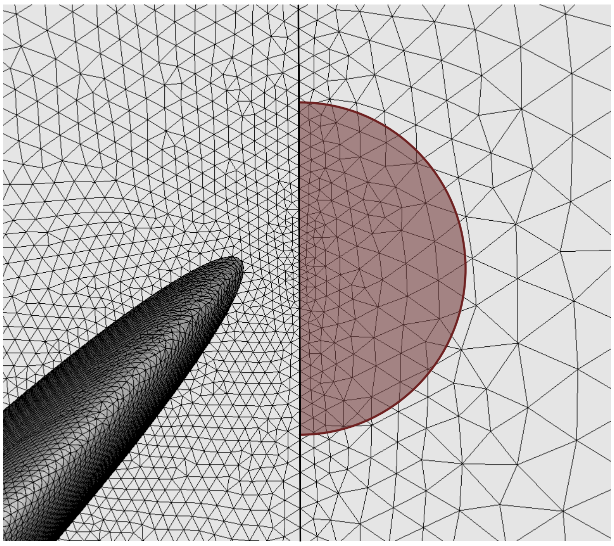

Figure 4.7: Evaluation volume.

and 130,000 elements. Conversely, the geometry without a crack utilizes approximately 24,000 elements and 38,000 nodes. This leads computing time of around 12 minutes with the CPUs we are using. We run these simulations on up to 6 machines in parallel, with up to 50 CPUs on each machine. `CalculiX` has here the advantage that it is published under GNU GPL allowing us to run as many simulations in parallel as our hardware can support.

In Figure 4.8, the shear stress in the right grain for an angle pair $\mathcal{E}_l, \mathcal{E}_r$ in one slip system (τ_{13}) is shown. The red semicircle illustrates the evaluation volume B. In both cases, the shear stress diminishes as the distance from the grain boundary increases. But in the case of the cracked geometry (Figure 4.8b) an overall higher shear stress is observed.

Now we want to investigate how the orientations of the two grains influence the shear stress within the right grain. To achieve this, we keep one of the grain orientations fixed while altering the orientation of the other grain.
In simulations involving a fixed left grain, we opt for $\mathcal{E}_l = (3.098, 1.686, 3.038)$ and a range of orientations for the right grain, with $\varphi_1^r \in [0.698, 1.744]$ and $\theta^r \in [0.702, 1.750]$, while keeping φ_2^r fixed at 4.196. For the scenario of a fixed left grain, the orientation of the right grain is held constant as $\mathcal{E}_r = (1.221, 1.226, 4.196)$, and the orientations of the left grain are in the range of $\varphi_1^l \in [2.575, 3.622]$ and $\theta^l \in [1.162, 2.021]$, with fixed $\varphi_2^l = 3.038$.

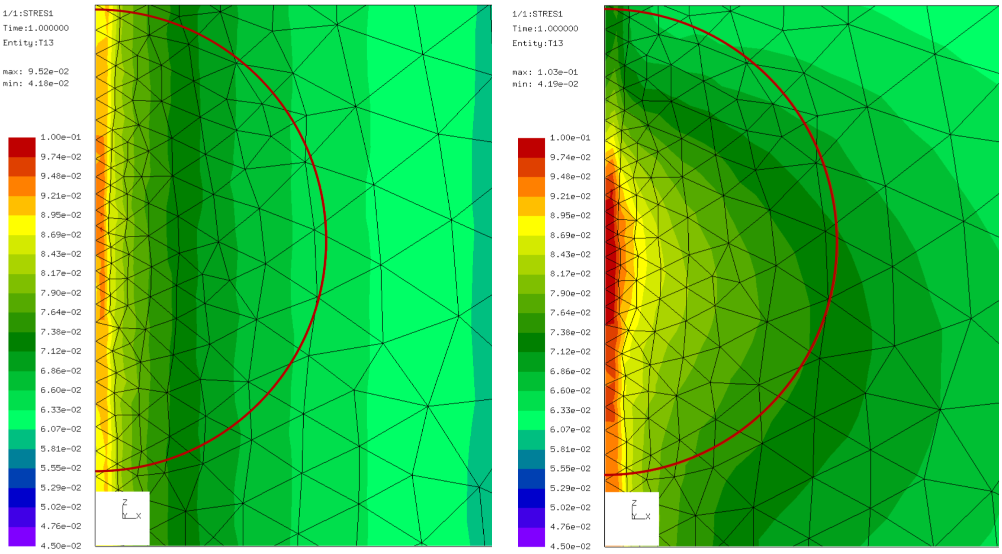

(a) Left grain is intact.   **(b)** Cracked left grain.

Figure 4.8: Shear stress in one slip system of the right grain. The grain boundary is at the left edge.

In both cases we use a grid of $100 \cdot 100$ orientations.

For the simulations with fixed orientation of the left grain, the course of the maximum shear stress is shown in Figure 4.9. The existence of a crack within the left grain leads to an amplified maximum shear stress within the slip systems of the right grain (Figure 4.9b). However, the variation of the shear stresses changes only insignificantly due to the crack. It's noteworthy that the points where the graph's slope changes abruptly correspond to the regions where the slip system exhibiting the highest shear stress also changes.

Accordingly, the ratio of shear stress with crack and without crack

$$q_{\tau} = \frac{\max(\bar{\tau}_{ij}^{WC})}{\max(\bar{\tau}_{ij}^{NC})} \tag{4.16}$$

is almost constant in large areas, as we can see in Figure 4.11a. Only at the points where the maximum loaded slip system changes, the ratio changes as well.

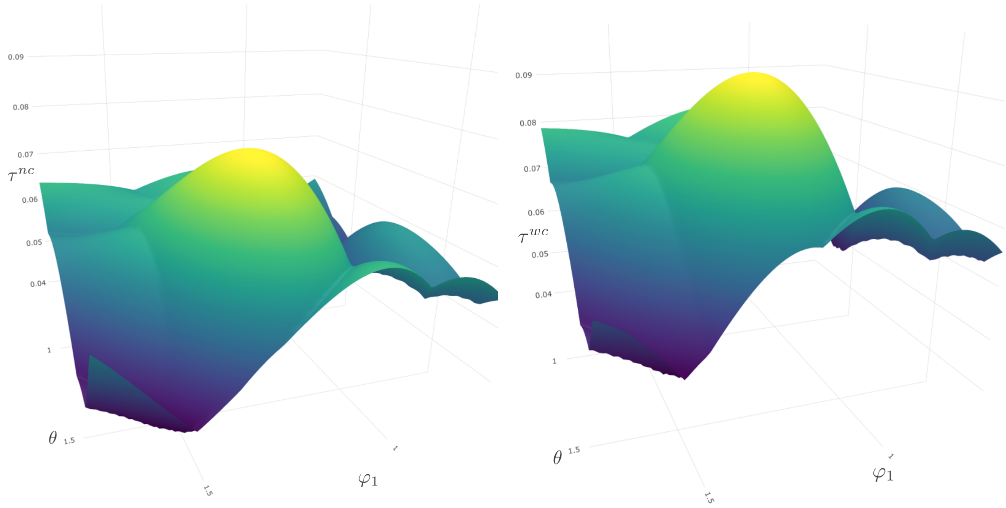

(a) Left grain is intact.

(b) Cracked left grain.

Figure 4.9: Maximum shear stress in right grain over orientation of the right grain.

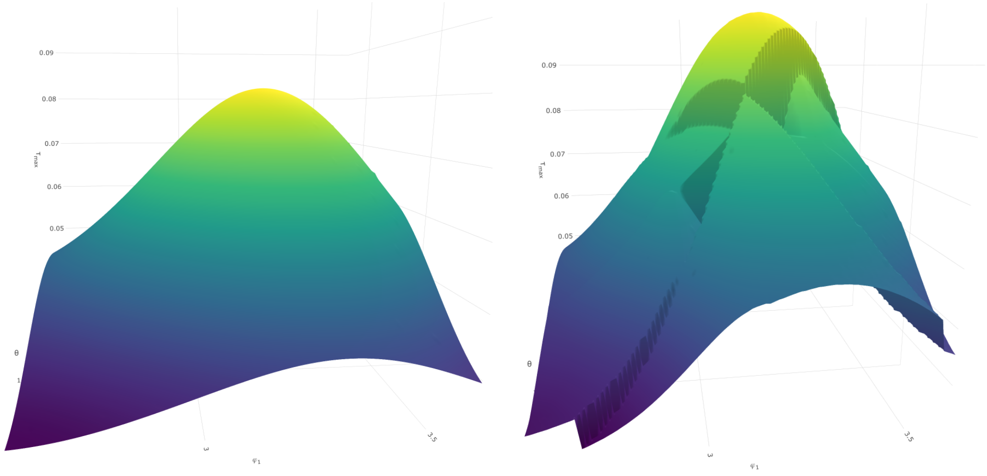

(a) Left grain is intact.

(b) Cracked left grain.

Figure 4.10: Maximum shear stress in right grain over orientation of the left grain.

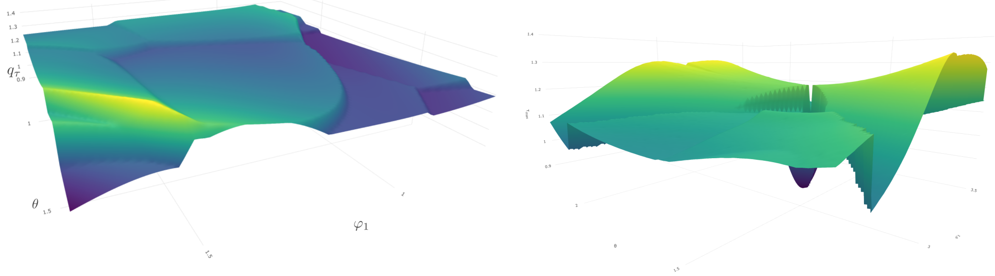

(a) Fix left grain. **(b)** Fix right grain.

Figure 4.11: Ratio between maximum shear stress in right grain with a cracked left grain and with intact left grain.

The simulations with a fixed right grain (Figure 4.10) show a different behavior. In cases where the left grain remains intact, modifying the orientation of the left grain leads to a gradual change in stress within the right grain. This change is smooth and results in a continuous shift in the maximum shear stress within the right grain, as one can see in Figure 4.10a. On the other hand, if the left grain is cracked, a rotation of the left grain leads to a variation of the crack direction. The crack direction has a significant impact on the stress field in the right grain. Especially when the rotation induces a shift in the maximum loaded slip system within the left grain, the direction of the crack undergoes an abrupt change. This results in discontinuity of the maximum shear stress in the right grain (Figure 4.10b). Consequently, these discontinuities can also be seen in the ratio q_τ (Figure 4.11b). Furthermore, it is noticeable that for a change in the orientation of the left grain in the quotient from the maximum shear stresses, the constant areas are no longer present.

4.3.3 Gradient Boosting Trees

Given the substantial time and computational resources that FEM simulations demand, their direct integration into the percolation model is impractical. Instead, we use a machine learning-based surrogate model as a viable alternative.

The model that we choose for the regression is a so-called gradient boosting tree. Here we give a brief introduction to this method following [38, 41]. Gradient boosting builds upon decision trees. For simplicity, we consider $\mathcal{X} = X_1 \times \cdots \times X_d = [0,1]^d$ as the d-dimensional input pace and $Y \in \mathcal{Y} = [0,1]$ as the target value to predict. In tree-based regression, the input space is partitioned into J mutually disjoint sets $R_j \subseteq \mathcal{X}, j = 1, \ldots, J$. Each of the sets is associated with a constant value γ_m. The regression function is then given by

$$\hat{f}(x) = \sum_{j=1}^{J} \gamma_m I_{R_j}(x), \tag{4.17}$$

where I_{R_j} is the indicator function on R_j. The model can be represented by a tree tree as shown for $d = 2$ in Figure 4.12a. $\hat{f}$ is a d-dimensional step function (Figure 4.12b). Let now $\Theta = \{(R_j, \gamma_j) : j \in 1, \ldots, J\}$ for a fix $J \in \mathbb{N}$, then we can write the regression function as

$$T(x; \Theta) = \sum_{j=1}^{J} \gamma_j I_{R_j}(x). \tag{4.18}$$

The aim is here to minimize the loss function $L(y_i, T(x_i; \Theta))$ which takes the true value and the prediction as an input. A commonly used loss function for a regression task is the quadratic error

$$L(y_i, \hat{f}(x_i)) = \frac{1}{2}\left(y_i - \hat{f}(x_1)\right)^2. \tag{4.19}$$

Therefore, the minimization is given by

$$\hat{\Theta} = \arg\min_{\Theta} \sum_{j=1}^{J} \sum_{x_i \in R_j} L(y_i, \gamma_j). \tag{4.20}$$

It is easy to see that, with the quadratic error as loss function and for given partition $R_1, \ldots, R_J$, finding the γ_j that minimize (4.20) is trivial. The solutions are just the average values of y_i in each set R_j:

$$\hat{\gamma}_j = \frac{1}{\#(\{x_i : x_i \in R_j\})} \sum_{x_i \in R_j} y_i, \tag{4.21}$$

where $\#(A)$ is the number of elements in A. The harder task is to find the partition. The computational effort to find the optimal partition is infeasible.

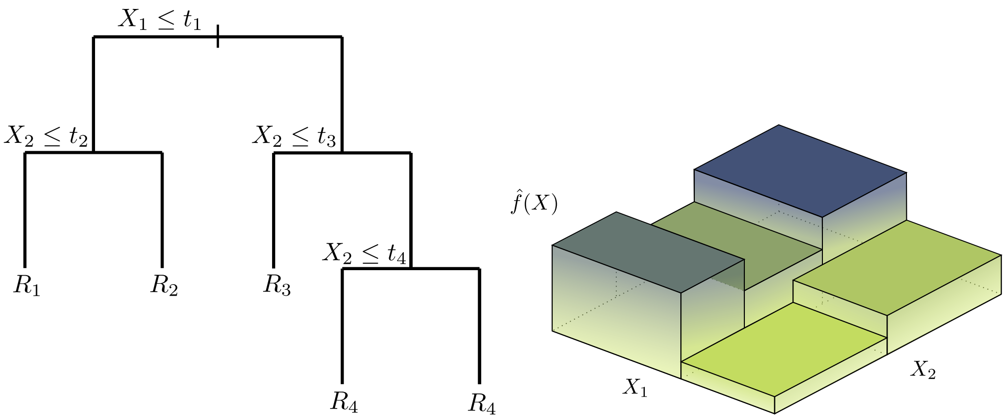

(a) Decision tree for a two-dimensional input space $\mathcal{X} = [0,1]^2$.

(b) Regression function for a two-dimensional input space $\mathcal{X} = [0,1]^2$.

Figure 4.12: Tree based regression.

So we need a simple procedure that leads to an acceptable partition. A possible approach is the following algorithm. We start with the whole input space $\mathcal{X}$ and find the hyperplane that splits the $\mathcal{X}$ into two regions

$$R_1(j,s) = \{X : X_j \leq s\} \text{ and } R_2(j,s) = \{X : X_j > s\}, \tag{4.22}$$

such that it minimizes

$$\min_{j,s}\left[\min_{c_1} \sum_{x_i \in R_1(j,s)} (y_i - c_1)^2 + \min_{c_2} \sum_{x_i \in R_2(j,s)} (y_i - c_2)^2\right]. \tag{4.23}$$

Both of the inner minimization problems are resolved using Equation (4.21). The resultant regions are then subdivided using the same approach until we reach a maximal tree size J. The maximal tree size is a tuning parameter, if J is chosen to large the model tends to overfit but on the other hand a too small value can result in a model that is not capable of capturing the complexity in the data.

Boosting trees contain of M regression trees, the output is the sum over all trees

$$f_M(x) = \sum_{m=1}^{M} T(x; \Theta_m). \tag{4.24}$$

For a boosting tree for each stage the minimization task (4.20) has to be solved, which leads to

$$\hat{\Theta}_m = \arg\min \sum_{i=1}^{N} L(y_i, f_{m-1}(x_i) + T(x_i; \Theta_m)), \tag{4.25}$$

where $f_{m-1}(x)$ is the output of the previous stage and $\Theta_m = \{(R_{j_m}, \gamma_{j_m}) : j_m \in 1, \ldots, J_m\}$. Finding the γ_{j_m} is again straight forward

$$\hat{\gamma}_{j_m} = \arg\min \sum_{x_i \in R_{j_m}} L(y_i, f_{m-1}(x_i) + \gamma_{j_m}), \tag{4.26}$$

therefore $\hat{\gamma}_{j_m}$ is the mean of the residuals $y_i - f_{m-1}(x_i)$ in each corresponding region R_{j_m}.

We here use the Gradient Boosting for building the regression trees. For this method, we use the gradient of the loss function $\mathbf{g}_m$ with components

$$g_{im} = \left[\frac{\partial L(y_i, f(x_i))}{\partial f(x_i)} \right]_{f(x_i) = f_{m-1}(x_i)} \tag{4.27}$$

to generate the tree of stage m. In the case of the quadratic error (4.19), the gradient is given by

$$g_{im} = y_i - f_{m-1}(x_i). \tag{4.28}$$

Rather than optimizing (4.25), for gradient boosting the tree $T(x; \Theta_m)$ is fitted to the negative gradient by least squares

$$\tilde{\Theta}_m = \arg\min_{\Theta} \sum_{i=1}^{N} \left(-g_{im} - T(x_i; \Theta)\right)^2. \tag{4.29}$$

For least square decision trees, fast algorithms exist to compute the $\tilde{R}_{jm}$. These regions approximate the regions R_{jm} that solve (4.25). The corresponding constants for each region are then given by (4.26).

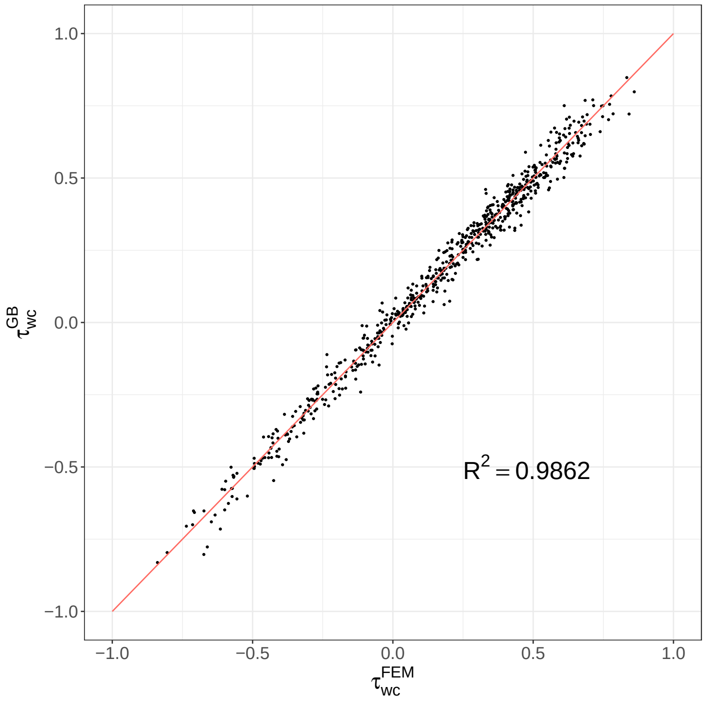

Figure 4.13: Prediction of the surrogate model over the results from the FEM simulations.

4.3.4 The Surrogate Model

As a dataset for the Surrogate Model that predicts the shear stress in the slip systems with a cracked adjacent grain τ_{ij}^{WC}, we use 25000 FEM simulations. These simulations were performed with random orientations for both grains, sampled according to the Haar measure on $SO(3)$. We use a gradient boosting tree, which takes the orientations of both grains and the shears stress in the slip system without the crack in the adjacent grain as an input. For each slip system we train a separate model, so there are 12 models in total

$$\tilde{\tau}_{ij}^{WC} = f_{ij}(\tau_{ij}^{NC}, \mathcal{E}_l, \mathcal{E}_r) \tag{4.30}$$

For the implementation we use the R library `gbm` [34]. We split the dataset into a train and a test set.

The train set is used to build the model. In contrast, the test set exclusively consists of data points that the model has never encountered before. This setup enables us to assess both the performance and the generalization capability of the gradient boosting regression. For the evaluation we use the R-squared value

$$R^2 = 1 - \frac{\sum_{i=1}^{N_t} (y_i - f_i)^2}{\sum_{i=1}^{N_t} (y_i - \bar{y})^2}, \tag{4.31}$$

here y_i is the true value, f_i the prediction of the model and $\bar{y}$ the mean of the true values in the test set.

The predictions of the model for one slip system are shown in Figure 4.13. The x-axis of the plot represents the shear stress values obtained from the FEM simulations, while the y-axis corresponds to the predictions made by the surrogate model.

The model's predictions closely match the results from the FEM simulations, as evidenced by a high R-squared value, approaching 0.986. This strong fit is consistent across all twelve models, with R-squared values consistently falling between 0.98 and 0.99.

4.4 Failure Criteria

The percolation simulations are evaluated with a failure criterion, which is based on the stress intensity factor introduced in Section 2.6.1. For this purpose we need to define the resulting total cracks that can lead to failure of the whole surface. These total cracks extend over multiple grains.

In this context, our initial focus is on crack clusters. A crack cluster C_i includes all the grains that are cracked and connected to each other through shared grain boundaries as shown in Figure 4.14a. Subsequently, we evaluate each potential total crack within this cluster. A total crack, in this context, is represented by the connecting vector formed by the Voronoi seeds originating from the grains within the cluster, as shown in Figure 4.14b.

The crack direction t_c, the crack normal n_c and the crack length l_c for such

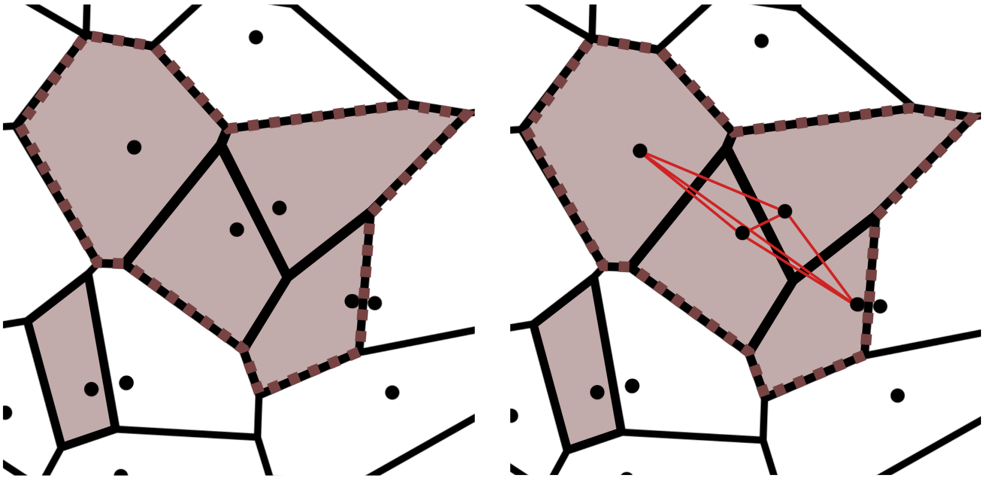

(a) Crack cluster in the percolation, the cracked grains are colored red. The cluster is marked with the doted line.

(b) All resulting total cracks in the cluster.

Figure 4.14: Crack clusters for the failure criteria

a resulting crack between two grains $g_1, g_2 \in C_i$ are given by

$$l_c = \sqrt{(x_{g_1} - x_{g_2})^2 + (z_{g_1} - z_{g_2})^2}, \tag{4.32}$$

$$t_c = \frac{1}{l}\begin{pmatrix} x_{g_1} - x_{g_2} \\ 0 \\ z_{g_1} - z_{g_2} \end{pmatrix}, \; n_c = \frac{1}{l}\begin{pmatrix} z_{g_1} - z_{g_2} \\ 0 \\ x_{g_2} - x_{g_1} \end{pmatrix}. \tag{4.33}$$

With the global isotropic stress σ_{iso} and equation (2.64) the K-factors for the crack are

$$K_I = n_c^T \cdot \sigma_{iso} \cdot n_c \sqrt{\frac{\pi \cdot l_c}{2}} \tag{4.34}$$

$$K_{II} = t_c^T \cdot \sigma_{iso} \cdot n_c \sqrt{\frac{\pi \cdot l_c}{2}}. \tag{4.35}$$

For the equivalent stress intensity factor, we use equation (2.66)

$$K_{eq} = \sqrt{K_I^2 + K_{II}^2}. \tag{4.36}$$

For a cluster we calculate the failure criteria as the maximum over all

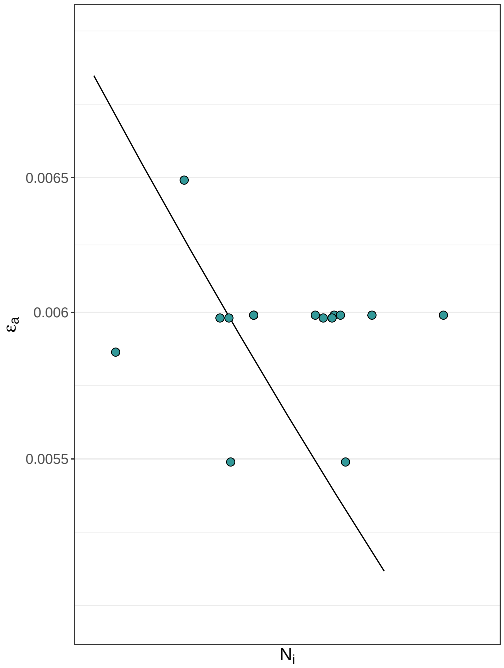

Figure 4.15: Experimental LCF failure times of RENE80 and fitted Coffin Manson Basquin equation.

possible cracks in the cluster

$$K_{eq}(C_i) = \max_{g_j, g_k \in C_i} \sqrt{K_I^2 + K_{II}^2}. \tag{4.37}$$

This leads to an equivalent K-factor for the whole surface given by

$$\bar{K}_{eq} = \max_i K_{eq}(C_i). \tag{4.38}$$

4.5 Results and Experimental Validation

The simulation process proceeds as follows: We begin by determining the initial failure times for a given strain amplitude. Then we initiate the cracking of the first grain. Next we calculate the updated Schmid factors and new failure times in the neighboring grains with the infection function. This iterative process is repeated, with the failure criterion being assessed after each grain has cracked.

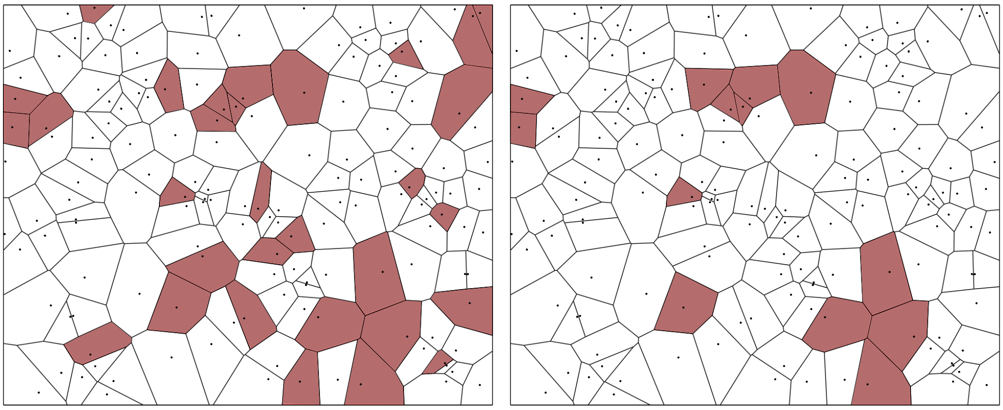

(a) Without infection, 32 grains are cracked.

(b) With infection function, 13 grains are cracked.

Figure 4.16: Comparison of the percolation model wit and without infection function. Both surface with same grain orientations and same K_{crit}.

For the validation of the percolation model we use experimental LCF data with RENE80 described in Section 2.7.

For the simulations we use prefitted parameters for the Coffin Manson Basquin equation as shown in Figure 4.15. For a comparison we run the simulations with and without the infection function.

The impact of the infection on the final crack clusters in the percolation model is significant. In Figure 4.16 the cracked grains in the simulation are shown for both cases. Here the input parameters and the failure criterion are the same. In the model without infection (Figure 4.16a) the crack initiation times of the grains are independent. Hence, a large amount of grains needs to crack to form big clusters. Here, in total 50 grains are cracked to meet the failure criterion. On the other hand, in the simulation with infection (Figure 4.16b), a cracked grain in almost all cases increases the Schmid factors of the adjacent grains. Therefore, the cracked grains tend to form clusters, which overall leads to a reduced amount of grains, that has to crack, to form a large enough cluster that reaches K_{crit}.

4.5.1 Fitting the Models

We now use the parameters from the experimental test as an input for the percolation model. The surface size is equal to the gauge area of the tests. We assume that the number of grains is Poisson distributed with $\lambda = 198$. For each strain amplitude we run 2500 Monte Carlo simulations. We use two parameters to fit the simulational results to the experiments. The first one is shift s_{CMB} of the Coffin Manson Basquin equation

$$\text{CMB}'(\varepsilon) = \text{CMB}(\varepsilon) \cdot s_{\text{CMB}}. \tag{4.39}$$

This parameter just shifts the position of the probability of failure (PoF). The other parameter that is used for fitting is the failure criteria K_{crit}. Which is the stress intensity at the tip of the crack that needs to be reached until we consider material failure. The value K_{crit} significantly influences the dispersion of the PoF, as illustrated in Figure 4.17. Higher values of the critical K-factor result in a broader distribution of failure times.

One of the advantages of this fitting approach for the PoF is its offline capability. Simulations are run once for all the strain inputs until all grains have cracked. We store the number of cycles and the equivalent K-facors every time K_{eq} increases. Subsequently, the parameters are fitted to the obtained results.

For a specific simulation indexed as j with a constant critical factor K_{crit}, the count of LCF cycles required until failure, denoted as $N_i^j(K_{\text{crit}})$, is determined by identifying the earliest cycle where for the equivalent stress intensity factor $K_{eq} \geq K_{\text{crit}}$ holds. The failure time for the set of parameters $\theta = \{K_{\text{crit}}, s_{\text{CMB}}\} \in \Theta$ is then given by

$$N_i^j(\theta) = \exp\left(\log\left(N_i^j(K_{\text{crit}})\right) + s_{\text{CMB}}\right). \tag{4.40}$$

For each strain level we use a kernel density estimation (KDE) to gain smooth densities $\hat{f}(N_i|\varepsilon_a, \theta)$ of the PoF. We use the KDE implementation in the R base package.

Let $n_{i,k}$ denote the number of LCF cycles observed in the k-th experiment conducted at a strain amplitude of $\varepsilon_{a,k}$. Our objective is to maximize the density values provided by $\hat{f}$ for the data points. To achieve this, we opt for the Maximum Likelihood Estimation (MLE) method. The Likelihood

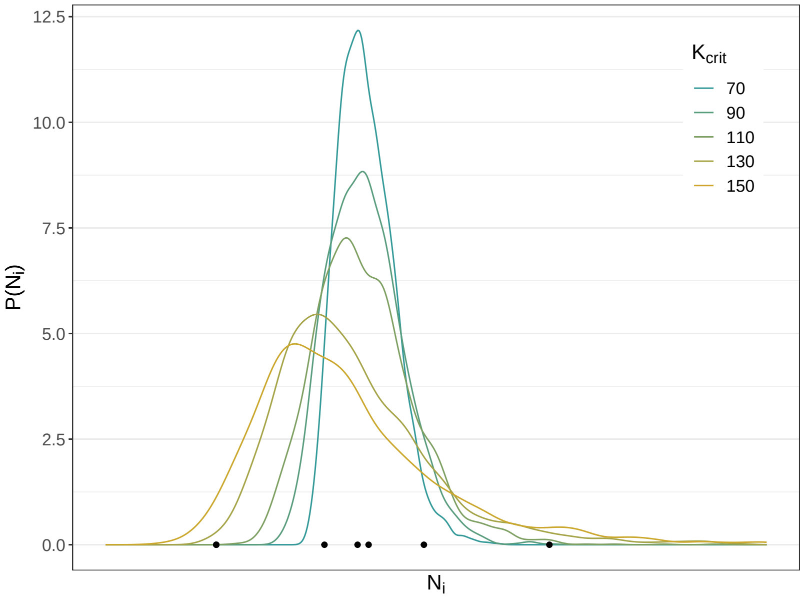

Figure 4.17: Density of the probability of Failure for $\varepsilon_a = 0.6\%$ with different Failure criteria K_{crit}.

function is given by

$$\mathcal{L}(\theta) = \mathcal{L}(n_{i,1}, \dots, n_{i,l}|\theta) = \hat{f}(n_{i,1}|\varepsilon_{a,1}, \theta) \cdot \quad \cdots \quad \cdot \hat{f}(n_{i,l}|\varepsilon_{a,l}, \theta). \tag{4.41}$$

Hence, we gain for the log-Likelihood

$$\log \mathcal{L}(\theta) = \sum_{i=1}^{l} \log \hat{f}(n_{i,k}|\varepsilon_{i,k}, \theta). \tag{4.42}$$

Therefore, we have as an optimization problem

$$\hat{\theta} = \underset{\theta \in \Theta}{\arg\min} - \log \mathcal{L}(\theta). \tag{4.43}$$

We solve this problem numerically with the Nelder-Mead algorithm which is implemented in the R-library `nloptr` [42].

4.5.2 Results

The fitted densities we gain from both models are shown in Figure 4.18. We can see that both models, with and without infection, predict statistical scatter bands that are within the expected order of magnitude. However, the

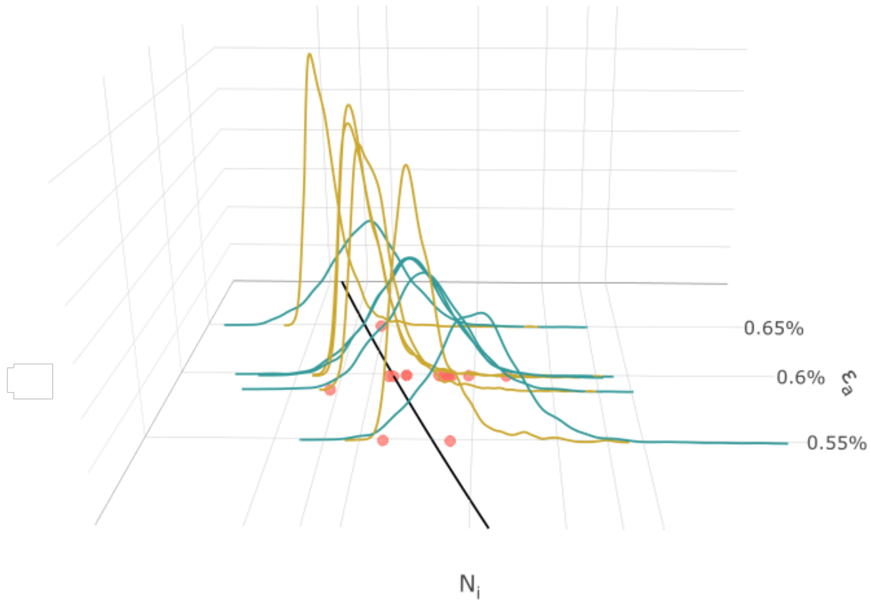

Figure 4.18: Density of the probability of Failure for the different strain amplitudes in a log-log plot. The model without the infection function in green, the one with infection in yellow. The CMB equation in black. The red points are the experimental data points.

infection-free model tends to produce predictions that are overly dispersed, whereas this dispersion is appropriately captured by the model that includes infection. Nevertheless, at a strain amplitude of 0.6%, there appears to be a rightward shift in the average compared to the infection model, although the dispersion is realistically modeled. This discrepancy may be attributed to batch variations in specimen production or experimental fluctuations in laboratory conditions, potentially serving as a secondary source of scatter.

5. Microstructual Models

5.1 Grain Orientations

When casting metal, the surface temperature decreases faster than the internal temperature during solidification of the material. This temperature gradient leads to a directional grain growth, therefore the orientation of the grains differ from the isotropic distribution. The grain orientations on the surface can be measured with an electron backscatter diffraction (EBSD)-based microscopy. As an example the longitudinal section of such an EBSD measurement is shown in Figure 5.1. The measurements are time and cost expensive, so the dataset of orientations is limited. In this section we use machine learning methods to gain the probability density for the distribution of the orientations.

But first we give a brief introduction to the basic concepts of neural networks [38].

5.1.1 Feed Forward Neural Networks

Neural networks are a commonly used method for regression or classification tasks.

Assume we have data from the input space $\mathcal{X} = X_1 \times \cdots \times X_D$ and target values from the output space $\mathcal{Y} = Y_1 \times \cdots \times Y_E$. A neural network consists of n layers: an input layer L_1, an output layer L_n, and $n-2$ hidden layers in between. Each layer L_i contains M_i neurons, where $M_1 = d$ for the input layer and $M_n = e$ for the output layer. The connections between two consecutive layers L_i and L_{i-1} are given by a weight matrix $\alpha_i \in \mathbb{R}^{M_i \times M_{i-1}}$.

Now, suppose we have an input X from the input space $\mathcal{X}$. This input is processed by the neural network as follows:

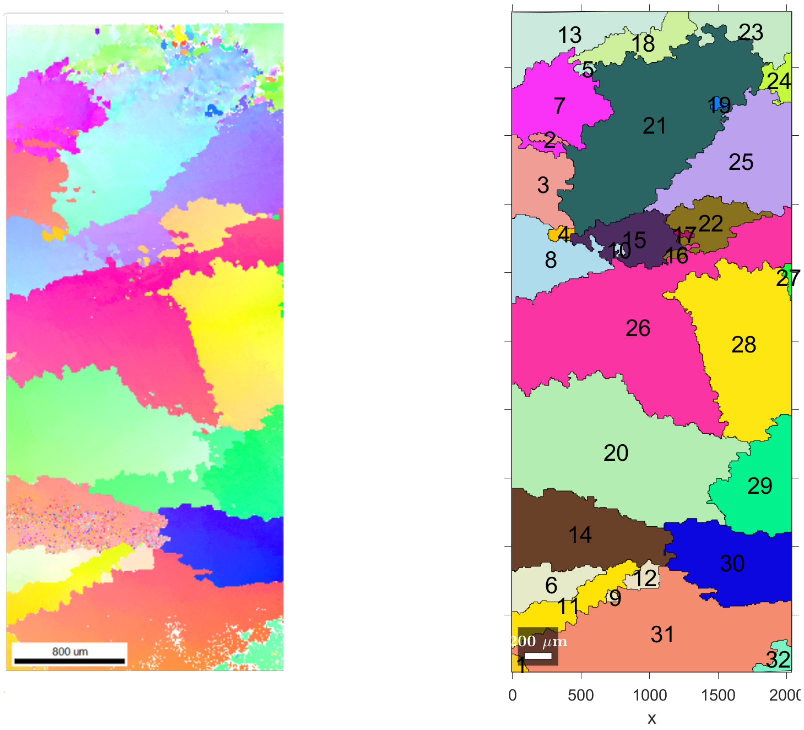

(a) Raw EBSD measurements.

(b) EBSD measurements after postprocessing.

Figure 5.1: Longitudinal section of a cylindrical specimen with EBSD measurement. The orientations are color coded with an inverse pole figure. Reprinted with permission of the RPTU Kaiserslautern-Landau.

$$\begin{aligned} Z^1 &= X \\ Z^i_m &= \sigma^i(\alpha^i_{0m} + (\alpha^i_m)^T Z^{i-1}),\ m = 1, \dots, M_i, i = 2, \dots, n-1 \\ f_e(X) &= Z^n_e, e = 1, \dots, E \end{aligned} \tag{5.1}$$

in this context, σ^i represents an activation function rather than a stress tensor. We use this notation to maintain consistency with the established literature. Common choices for the activation function include the sigmoid function $\sigma^i(\nu) = 1/(1 + \exp(\nu))$ for hidden layers, except for the output layer. For regression tasks, the identity function is often used in the output layer, while for classification tasks, the softmax function is a common choice. The structure of the neural network, i.e. the number of hidden layers, the number of neurons and the choice of activation functions is referred to as the architecture of the network.

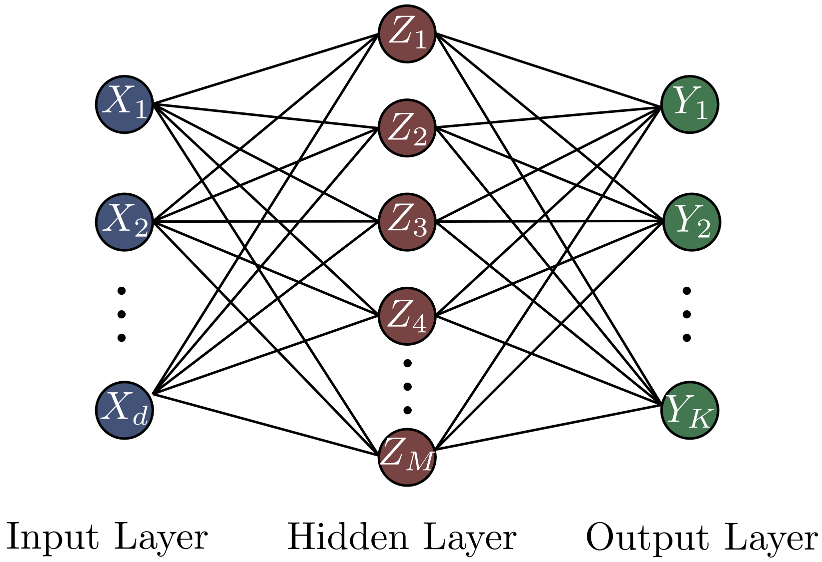

Figure 5.2: Neural network with one hidden layer. The circles are the neurons and the connecting lines represent the weights.

During the training process of a neural network, weights that connect the neurons are updated. The architecture remains the same. For the sake of simplicity we use for the description of the training process an architecture with just one hidden layer containing M_2 hidden neurons as illustrated in Figure 5.2.

In this case we have

$$\theta =(\alpha^1_{0m}, \alpha^1_m, \alpha^2_{0e}, \alpha^2_e) \tag{5.2}$$

as the $M_2 \cdot (D+1) + E \cdot (M_2+1)$ trainable weights connecting these layers. These weights are usually initialized with random values. Let no $x_1, \dots, x_N \in \mathcal{X}$ be the training inputs with associated targets $y_1, \dots y_N \in \mathcal{Y}$. With the output of the network and the targets we can evaluate a loss function. For regression task the sum of squared errors given by

$$R(\theta) = \sum_{e=1}^{E} \sum_{j=1}^{N} (y_{je} - f_e(x_j))^2 \tag{5.3}$$

is a comment loss function. Whereas for classification the cross entropy

$$R(\theta) = \sum_{e=1}^{E} \sum_{j=1}^{N} y_{je} \log f_e(x_j) \tag{5.4}$$

is often used. For the loss functions the derivatives $\partial R / \partial \alpha^1_{ml}$ and $\partial R / \partial \alpha^2_{le}$

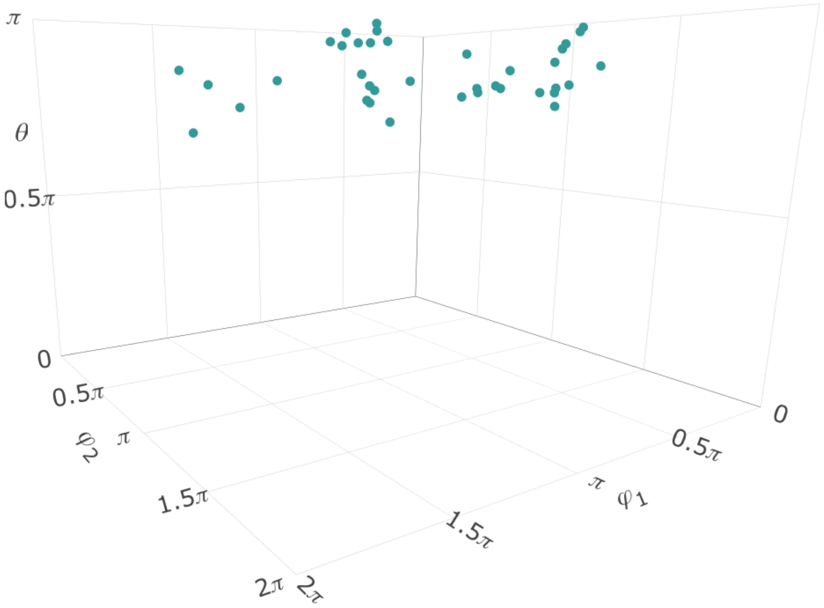

Figure 5.3: Grain orientations from the EBSD-measurements

with respect to weights can be calculated.

The training of the network is an iterative process. The weights are updated in the train step $(r + 1)$ as follows:

$$\begin{aligned}(\alpha^2_{le})^{(r+1)} &= (\alpha^2_{le})^{(r)} - \gamma_r \sum_{i=1}^{N} \frac{\partial R_i}{\partial (\alpha^2_{le})^{(r)}} \\ (\alpha^1_{ml})^{(r+1)} &= (\alpha^1_{ml})^{(r)} - \gamma_r \sum_{i=1}^{N} \frac{\partial R_i}{\partial (\alpha^1_{ml})^{(r)}},\end{aligned} \tag{5.5}$$

where γ_r is the learning rate.

In the training process, the objective is not to identify the parameters that yield the absolute global minimum of the loss function on the training dataset. Instead, we aim for a trade-off between a low loss on the training set and the avoidance of overfitting the network, ensuring that it can generalize effectively when confronted with unfamiliar data.

5.1.2 Density Estimation as Supervised Function Approximation

Our objective is to estimate the grain orientation density using the data obtained from EBSD measurements, but as previously mentioned, our dataset is limited. The 38 measurements of the Euler angles are shown in Figure 5.3. We assume that these measurements, denoted as $x_1, \dots, x_N$, are independent and identically distributed random samples drawn from the unknown probability density $g(x)$.

We address the limited amount of measurements with synthetic minority oversampling technique (SMOTE) [11]. SMOTE is a simple algorithm that generates additional synthetic data from a given dataset. For each data point x_i the k nearest neighbors $x_{i_1}, \dots, x_{i_k}$ in the dataset are estimated. Then n of these nearest neighbors are chosen randomly. The new artificial data points are then given by

$$\hat{x}_{i_j} = x_i + r \cdot (x_{i_j} - x_i), \tag{5.6}$$

where r is sampled from the uniform distribution on $[0, 1]$. We use the implementation of SMOTE, that is provided in R-library `smotefamily` [65]. In addition, we use the symmetries of the FCC crystal lattice which leads to $\bar{N} = 38 \cdot 12 \cdot n$ data points. The dataset with symmetries and the synthetic points is show in Figure 5.4.

To tackle this density estimation challenge, we reframe it as a classification problem [38]. To this end we sample the same amount of additional values $x_{\bar{N}+1}, \dots, x_{2\bar{N}}$ from the uniform distribution on $[0, 2\pi] \times [0, \pi] \times [0, 2\pi] \subset \mathbb{R}^3$. Each data point is associated with a label $Y \in \{0, 1\}$ such that,

$$Y_i = \begin{cases} 1 & \text{if } i = 1, \dots, \bar{N} \\ 0 & \text{if } i = N + 1, \dots, 2\bar{N}. \end{cases} \tag{5.7}$$

With this dataset we train a neural network that predicts whether the input x is from the extended set of the measurements with density $g(x)$ or from the uniform distribution with density $g_0(X)$. For the neural network we use the R-library `keras` [1].

The neural network trained with the samples $(x_1, y_1), \dots, (x_{\bar{N}}, y_{\bar{N}})$,

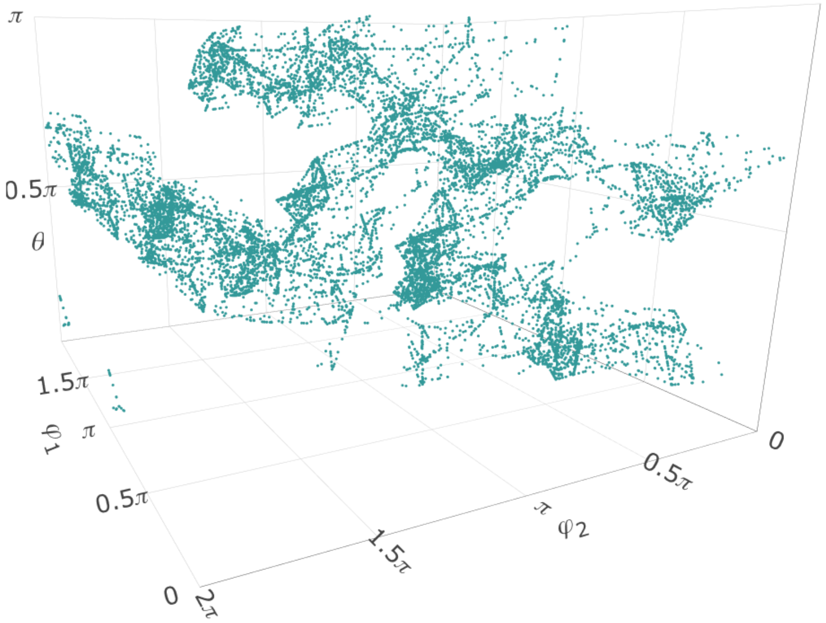

Figure 5.4: Dataset with SMOTE and symmetries.

$(x_{\bar{N}+1}, y_{\bar{N}+1}), \dots, (x_{2\bar{N}}, y_{2\bar{N}})$ approximates the probability of a sample belonging to the extended set of measurements

$$\mu(x) = \mathbb{E}(Y|x) = \frac{g(x)}{g(x) + g_0(x)}. \tag{5.8}$$

Let now $\hat{\mu}$ be the approximation for μ, with equation (5.8) we obtain for the estimated of g:

$$\begin{align} \hat{\mu}(x) = & \frac{\hat{g}(x)}{\hat{g}(x) + g_0(x)} \tag{5.9} \\ \Leftrightarrow & \mu(x)(g(x) + g_0(x)) = g(x) \tag{5.10} \\ \Leftrightarrow & \hat{g}(x)(1 - \hat{\mu}(x)) = \widehat{\mu(x)} g_0(x) \tag{5.11} \\ \Leftrightarrow & \hat{g}(x) = \hat{\mu}(x) \frac{g_0(x)}{1 - \hat{\mu}(x)}. \tag{5.12} \end{align}$$

5.1.3 Sampling new Angles

We now want to sample angles from the distribution with the approximated density $\hat{g}$. To this end, we use the Metropolis Hastings algorithm [39, 59]. For this Markov chain based algorithm we use a conditional density $q(y|x)$

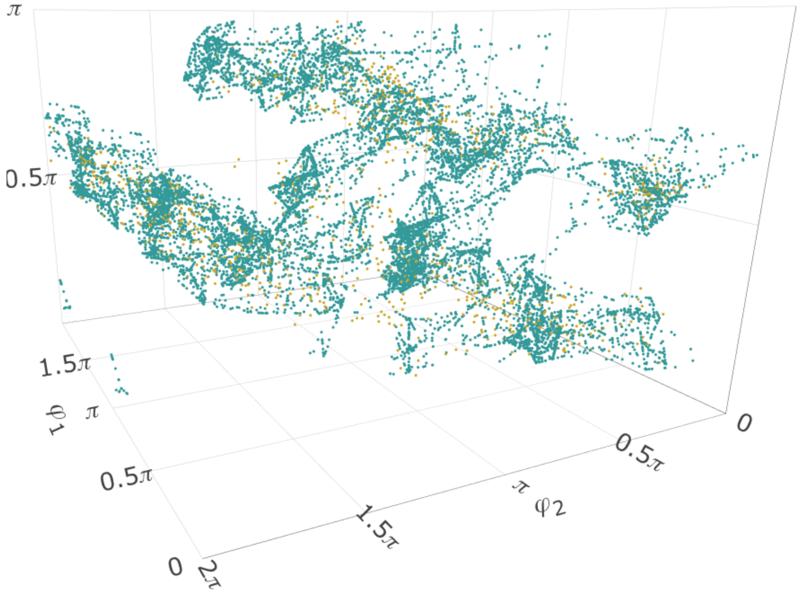

Figure 5.5: Sampled angles from $\hat{g}$ in yellow, the dataset with symmetries and SMOTE as a reference in green.

called the proposal kernel. For a given value $X^{(t)} = x^{(t)}$ of the Markov chain we then sample $Y_t \sim q(y|x^{(t)})$. The next step of the Markov chain is given by

$$X^{(t+1)} = \begin{cases} Y_t & \text{with probability } \rho(x,y) \\ x^{(t)} & \text{with probability } 1-\rho(x,y), \end{cases} \tag{5.13}$$

where

$$\rho(x,y) = \min\left\{\frac{\hat{g}(y)}{\hat{g}(x)}\frac{q(x|y)}{q(y|x)}, 1\right\}. \tag{5.14}$$

We select the proposal kernel $q(y|x)$ for $x = (\varphi_1, \theta, \varphi_2)$ to be a uniform distribution within the ranges $[\varphi_1 - 0.5, \varphi_1 + 0.5] \times [\theta - 0.5, \theta + 0.5] \times [\varphi_2 - 0.5, \varphi_2 + 0.5]$. Since the proposal kernel is symmetric, the acceptance probability simplifies to:

$$\rho(x,y) = \min\left\{\frac{\hat{g}(y)}{\hat{g}(x)}, 1\right\}. \tag{5.15}$$

To initiate the process, we set x^0 as a random orientation sampled from a uniform distribution within the range $[0,2\pi]\times[0,\pi]\times[0,2\pi]$. During the burn-in phase, we discard the first $k = 1000$ samples. For testing the results, we perform 10^5 iterations and obtain a sample of 1000 orientations $\hat{x}_1, \dots, \hat{x}_{1000}$

from the remaining $10^5 - 10^3$ values. A subsample of 200 orientations is displayed in Figure 5.5, alongside the dataset used for training. The sampled orientations appear to align well with the training set.

We compare the average distance of the sampled orientations to the measurements, with random orientation sampled according to the Haar measure. The natural distance metric on $SO(3)$ is the Riemannian distance

$$d_R(U_1, U_2) = \frac{1}{\sqrt{2}} \|\mathrm{Log}(U_1^T U_2)\|_F = |r|, \tag{5.16}$$

where $r \in [-\pi, \pi)$ is the misorientation angle and

$$\mathrm{Log}(U) = \begin{cases} \mathbf{0} & \text{if } \theta = 0 \\ \dfrac{r}{2\sin a}\left(U - U^T\right) & \text{else.} \end{cases} \tag{5.17}$$

Here $a \in [-\pi, \pi)$ satisfies $\mathrm{tr}(U) = 1 + 2\cos a$.

We utilize the 38 orientations from the EBSD measurements, incorporating the 12 symmetries denoted as $U_1^1, \ldots, U_{38}^1, \ldots, U_{38}^{12}$. For an orientation x_i the minimal misorientation angle is then given by

$$r_i = \min_{j=1,\ldots 38, k=1,\ldots,12} d_R(U(x_i), U_j^k). \tag{5.18}$$

The orientations sampled from $\hat{g}$ exhibit an average misorientation angle of 0.26, in contrast to an average misorientation of 0.41 for orientations sampled from the Haar measure.

We investigate the impact of this different distribution of orientations in Section 6.5.

5.2 Percolation with Grain Boundary

In addition to intracrystalline crack initiation, which occurs due to intrusion and extrusion caused by the slip systems of FCC crystals, we also observe transcrystalline crack initiation and growth along the grain boundaries in LCF, as discussed in [53].

Our aim is to investigate the impact of these transcrystalline cracks on the percolation model in this section. The implementation and results in this section are a joint work with Emil Krieger and resulted in the bachelor thesis “Percolation Models for Intergranular Crack Growth”.

5.2.1 Adjustments to the Percolation Model

For modeling crack initiation times at grain boundaries, we consider a mixture of shear and normal stresses acting on these boundaries. Let d denote the normalized direction and n the normalized normal vector of the grain boundary between adjacent grains g_1 and g_2. Utilizing the anisotropic stress tensors σ^{g_1} and σ^{g_2} in both grains, as described in equation (4.3), we calculate the mean normal stress σ_n^b and the shear stress τ^b at the grain boundary as follows:

$$\begin{aligned} \sigma_n^b &= \frac{1}{2}\left(n^T\sigma^{g_1}n + n^T\sigma^{g_2}n\right) && (5.19)\\ \tau^b &= \frac{1}{2}\left(n^T\sigma^{g_1}d + n^T\sigma^{g_2}d\right). && (5.20)\end{aligned}$$

In a first approach to model the failure times of the grain boundaries, we simply utilize the shear stress at the grain boundary. Using the Ramberg-Osgood equation and the Coffin-Manson-Basquin equation we obtain for the failure times

$$N_i^\tau = \mathrm{CMB}^{-1}\left(\mathrm{RO}(\tau^b)\right). \tag{5.21}$$

The shear stress at the grain boundary depends on the anisotropic stress in the adjacent grains and the orientation of the boundary. For a high shear stress both grains have to be orientated in such a way that the applied strain leads to a high anisotropic stress. In addition, the angle between boundary and the uniaxial load has to be around 45°. Compared to the Schmid factors, which only depend on the stiffness of a single grain and the angle between load and one of the twelve slip systems, a high shear stress at the boundary is rare.

Therefore, this modeling leads to the fact that the grain boundaries crack late compared to the grains. The grain boundaries therefore have almost no influence on the percolation model.

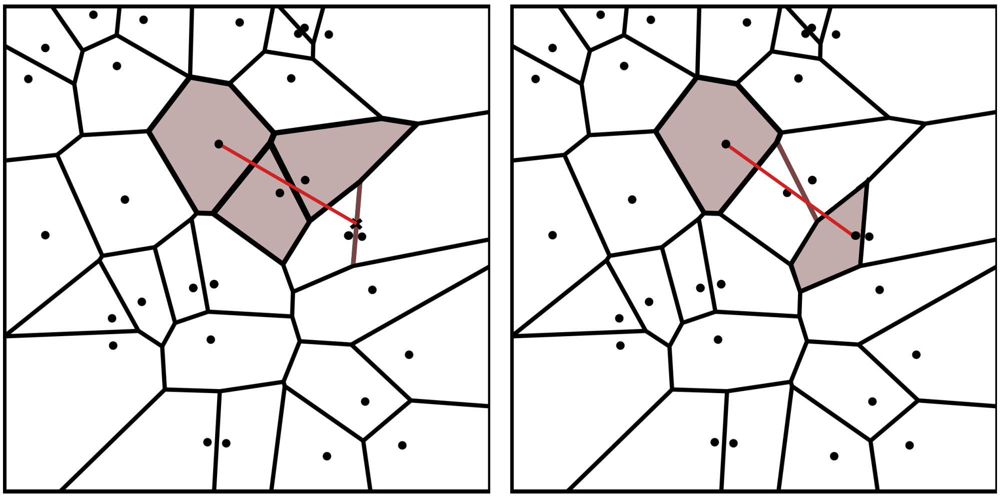

(a) Cracked grain boundary extending a cluster of cracked grains. One possible resulting crack.

(b) Two cracked grains connected by a cracked grain boundary, forming a cluster.

Figure 5.6: Crack clusters with grain boundary.

In a second approach we combine the shear stress and the normal stress into a single factor, we introduce this bound stress impact factor ω^b defined as:

$$\omega^b = \sqrt{\left(\sigma_n^b\right)^2 + \left(\tau^b\right)^2}. \tag{5.22}$$

Next, using the Ramberg-Osgood and Coffin-Manson-Basquin equations, we calculate the failure time for the grain boundary b as:

$$N_i^\omega = \mathrm{CMB}^{-1}\left(\mathrm{RO}(\omega^b)\right). \tag{5.23}$$

This combination of the stresses leads to early failure times of the grain boundaries.

However, to incorporate these cracked grain boundaries into the percolation model, we must also extend the failure criteria to determine how these individual grain boundaries contribute to the overall failure of the material.

A crack cluster contains now all cracked grains, that are adjacent, and connected grain boundaries which are cracked. We define two grain boundaries as connected if they share a common point. Similarly, a grain and a boundary, denoted as b, are considered connected if any of the grain's boundaries and b share a common point. Figure 5.6 illustrates the connection between grain and grain boundary. For the calculation of the stress intensity factor of crack that starts or ends on a grain boundary instead of the seed we simply use the center of the grain boundary, as illustrated in Figure 5.6a.

5.2.2 Results

With the grain boundary crack initiation times and the failure criterion that includes the boundaries, we can compare the percolation with grain boundaries with the model that only accounts for the cracked grains. We use the fitted model from Section 4.5 without the infection function for the simulations with the three strain amplitudes $\varepsilon_a \in \{0.35\%, 0.4\%, 0.45\%\}$.

As mentioned above, the crack initiation criterion for the grain boundaries that only utilizes the shear stress (Equation (5.21)) results in a probability density for the overall failure time that is indistinguishable from the percolation model with pure intracrystalline crack initiation. Therefore, in Figure 5.7 only the densities of the probability of failure for pure intracrystalline crack initiation and the densities obtained from the model which additionally utilize ω^b are shown.

The left plot (Figure 5.7a) shows the probability densities with the fitted K_{crit} from Section 4.5. Both models show a similar scatter band. Due to the additional possible cracked boundaries the percolation with transcrystalline crack initiation leads to an overall early failure.

If we reduce the critical stress intensity (Figure 5.7b), both models show different behavior. As stated in the previous section, the scatter band of the probability density of the model with pure intracrystalline crack growth is reduced. The probability densities of the model which also accounts for transcrystalline crack initiation shows a completely different behavior. For the low strain amplitude ($\varepsilon_a = 0.35\%$) the probability density has a left tail and a sharp peak at higher load cycles. The density for the middle strain amplitude ($\varepsilon_a = 0.4\%$) is a bit higher for the low load cycles, therefore

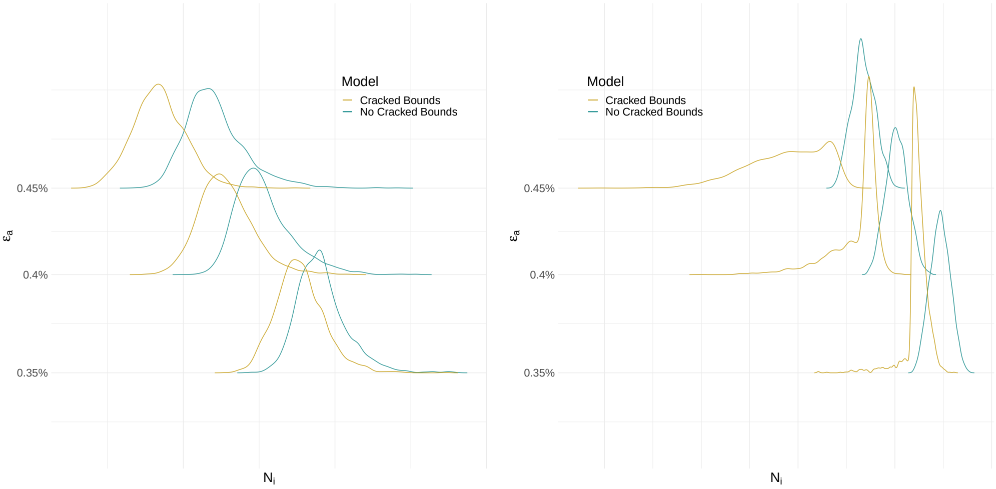

(a) Simulations with $K_{\text{crit}} \approx 100$.

(b) Early stopped simulations, $K_{\text{crit}} = 50$.

Figure 5.7: Density of the probability of failure for the model with and without cracked grain boundaries. Logarithmic scaled axes.

the peak is not so sharp. Under the high strain amplitude ($\varepsilon_a = 0.45\%$), the peak reduce further and the probability density for the low load cycles increases.

The modeling approach for crack initiation times with ω^b, leads to many grain boundaries that crack way earlier than the grains. But for larger crack clusters it is necessary that several grains are cracked, as the boundaries on their own are not so likely to build clusters.

With the reduction of the critical stress intensity factor, the crack clusters that lead to failure are smaller. Therefore, the possibility that just the cracked grain boundaries form a cluster that is large enough to reach the failure criterion increases. This explains the left tail of the densities. Moreover, the peak in the densities align with the cycles at which the probability density of the pure intracrystalline crack initiation becomes larger than zero.

The stress intensity depends on the applied strain, therefore for the higher strain amplitudes the clusters that reach the critical value are even smaller. Hence, the left tail of the probability density is more noticeable and the peak reduces.

Overall, both approaches for the transcrystalline crack initiation are not capable to model the crack initiation times for the boundaries correctly. Investigations of the crack surface from test specimens show that under these loading conditions transcrystalline and intracrystalline crack initiation occur. With our modeling approaches, either transcrystalline or intracrystalline crack initiation dominates.

6. Multiaxial Percolation

In this section, we will broaden the scope of the epidemiological percolation model introduced in Section 4 to accommodate multiaxial stress scenarios. This extension is especially essential when applying the model to real-world components, as these components experience a variety of stress states during their operational use, not restricted to uniaxial stress alone. While the core percolation model requires only minimal adjustments to accommodate this, the development of a multiaxial infection function demands additional effort and consideration.

6.1 Adjustments to the Percolation Model

The input for the percolation model is now the stress tensor σ_{iso}, rather than the strain amplitude ε_a. In the simulations we use the Hooks law to calculate the strain amplitude from the von Mises equivalent stress

$$\varepsilon_a = \frac{\sigma_{vM}}{E}. \tag{6.1}$$

The stress range in the experiments is large compared to the experiments that we used for the uniaxial model. This variation results in a considerable spread in the stress intensity factor. Consequently, the failure criterion would not be achieved for small strains, while for high strains, failure would occur as soon as two adjacent grains crack. We overcome this problem by normalizing the equivalent stress intensity factor with the von Mises stress

$$K_{eq} = \frac{1}{\sigma_{vM}} \sqrt{K_I^2 + K_{II}^2}. \tag{6.2}$$

This has the advantage that the failure criterion is purely geometric. Nevertheless, normalization has its drawback, since it removes the influence of stress levels on the failure criterion. However, when compared to a simplistic criterion that solely considers crack length, the K-factor based criterion offers the advantage of considering both the orientation of the crack and the multiaxiality of the stress state.

6.2 Multiaxial Infection Function

Using the simulations from Section 4.3 with random stress tensors as boundary conditions for the multiaxial infection function is indeed feasible. However, in addition to the 6 angles for the orientations, we now have 6 independent components of the stress tensor and an angle between the surface and the grain boundary, this approach leads to a 13-dimensional input space for the surrogate model. Consequently, a significantly larger number of simulations has to be performed to achieve reasonably accurate predictions of the shear stress within the infected grain. We overcome this problem by using the linear nature of the elastic deformations.

6.2.1 Decomposition of the Stress

The objective here is to decompose the calculation of shear stress within the slip systems into individual components that are dependent solely on single parts of the stress tensor. As the stress tensor is symmetric, it consists only of 6 independent entries. For the decomposition we introduce the following notion for these parts:

$$\begin{aligned}
\mathbf{1}_{xx} &:= \begin{pmatrix} 1 & 0 & 0 \\ 0 & 0 & 0 \\ 0 & 0 & 0 \end{pmatrix}, \mathbf{1}_{yy} := \begin{pmatrix} 0 & 0 & 0 \\ 0 & 1 & 0 \\ 0 & 0 & 0 \end{pmatrix}, \mathbf{1}_{zz} := \begin{pmatrix} 0 & 0 & 0 \\ 0 & 0 & 0 \\ 0 & 0 & 1 \end{pmatrix}, \\
\mathbf{1}_{xy} &:= \begin{pmatrix} 0 & 1 & 0 \\ 1 & 0 & 0 \\ 0 & 0 & 0 \end{pmatrix}, \mathbf{1}_{yz} := \begin{pmatrix} 0 & 0 & 0 \\ 0 & 0 & 1 \\ 0 & 1 & 0 \end{pmatrix}, \mathbf{1}_{zx} := \begin{pmatrix} 0 & 0 & 1 \\ 0 & 0 & 0 \\ 1 & 0 & 0 \end{pmatrix}.
\end{aligned} \tag{6.3}$$

Let now be $I_\sigma := \{xx, yy, zz, xy, yz, zx\}$, a given stress tensor can be rewritten as

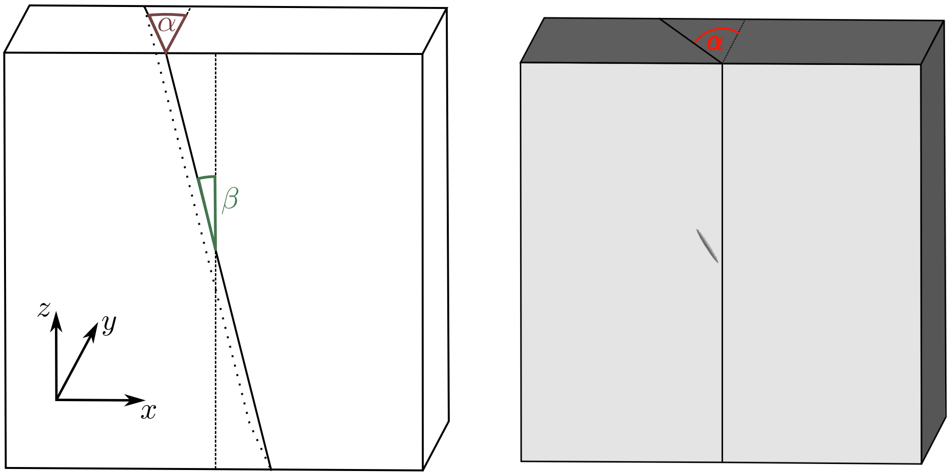

(a) Misalignment of the grain boundary and the y, z-plane.

(b) Cracked geometry for the multiaxial infection with angle between grain boundary and y-axis.

Figure 6.1: Misalignment of the grain boundary and actual geometry for the FEM simulations (right).

$$\sigma = \begin{pmatrix} \sigma_{xx} & \sigma_{xy} & \sigma_{zx} \\ \sigma_{xy} & \sigma_{yy} & \sigma_{yz} \\ \sigma_{zy} & \sigma_{yz} & \sigma_{zz} \end{pmatrix} = \sum_{k \in I_\sigma} \sigma_k \mathbf{1}_k. \tag{6.4}$$

We now use the decomposition to calculate the shear stress. So with equation (2.50) we gain

$$\begin{aligned} \tau_{ij} &= n_i \;\cdot\; \sigma \;\cdot\; t_{ij} \\ &= n_i \;\cdot\; \left(\sum_{k \in I} \sigma_k \mathbf{1}_k \right) \;\cdot\; t_{ij} \\ &= \sum_{k \in I} \left(\sigma_k \; n_i \;\cdot\; \mathbf{1}_k \;\cdot\; t_{ij} \right) \\ &= \sum_{k \in I} \left(\sigma_k \; \tau_{ij}^k \right), \end{aligned} \tag{6.5}$$

where $\tau_{ij}^k = n_i \cdot \mathbf{1}_k \cdot t_{ij}$ is shear stress in the slip system induced by the stress part $k \in I$.

Rather than constructing a model that provides the complete shear stress within the slip systems, we are now creating six distinct models, each dedicated to one of the stress components.

In addition to the linearity of the Schmid factors, the elasticity equation is also linear, hence we can build the infection model from the decomposition.

6.2.2 Geometry

Due to the decomposition introduced in the previous section, the models have become independent of the global stress state. However, since the crack direction depends on the global stress, it is necessary to account for all potential crack directions within the left grain. Instead of conducting FEM simulations using just two geometries (one with a crack in the left grain and one without), we are now employing seven distinct geometries for each angle pair.

To simplify the process, we can reduce the initial 12 slip systems to six crack directions. This simplification is possible because the crack is projected onto the x, z-plane within the geometry, and in an FCC crystal, there are six pairs of slip systems with distinct directions.

With the decomposition of the stress into these six components, we now have a total of 42 FEM simulations for each angle pair.

It is noteworthy that in the simulations for the uniaxial model, the grain boundary was consistently aligned with the y, z-plane. In real polycrystalline materials, such alignment usually is not given. To account for this potential misalignment, we introduce two angles, as illustrated in Figure 6.1a. The angle between the y-axis and the grain boundary is denoted as α, while the angle between the z-axis and the grain boundary is denoted as β.

We consider a random $\alpha \in [-10°, 10°]$ in our simulations (see Figure 6.1b). This range has been carefully chosen because higher values of α could potentially result in a grain boundary intersecting the crack.

We account for the potential misalignment between the boundary and the z-axis during the integration of the infection model into the percolation simulation (in Section 6.2.5). Consequently, during the construction of the geometries, we do not consider the angle β.

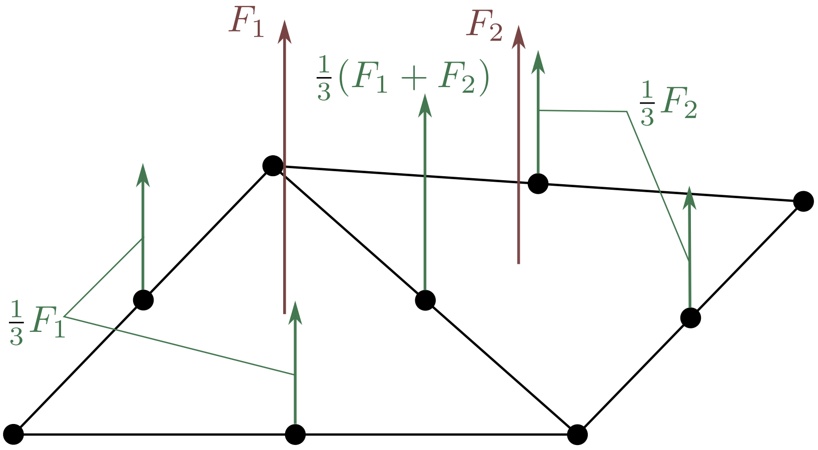

Figure 6.2: Distribution of the surface Force (red) onto the nodes (green) for a quadratic tetrahedral element.

6.2.3 Boundary Conditions

The input deck format employed by `CalculiX` is designed to directly handle normal stresses, and it lacks built-in support for shear stresses. To address this limitation, we devise a workaround by directly applying the resultant force to the nodes rather than using surface stresses.

The stresses that we want to apply are the 6 stress tensors given in equation (6.3). We can determine the force required to be applied to a geometry's surface for a given stress tensor, by

$$F_S = |S| \cdot \sigma \cdot n_S, \tag{6.6}$$

here, n_S represents the outward-pointing normal vector of the surface, and $|S|$ denotes the surface area.

Now, let $|A_E|$ be the surface area of a surface element. The force to be applied to this element can be determined as:

$$F_{A_E} = \frac{|A_E|}{|S|} \cdot F_S. \tag{6.7}$$

This force is then distributed to the nodes, depending on the type of the surface element [18]. For quadratic tetrahedral elements, as illustrated in Figure 6.2, there is no force applied to the corner nodes. Instead, nodes positioned in the middle of an edge receive $\frac{1}{3}$ of F_{A_E}.

Applying boundary conditions to the cracked surface is a challenging en-

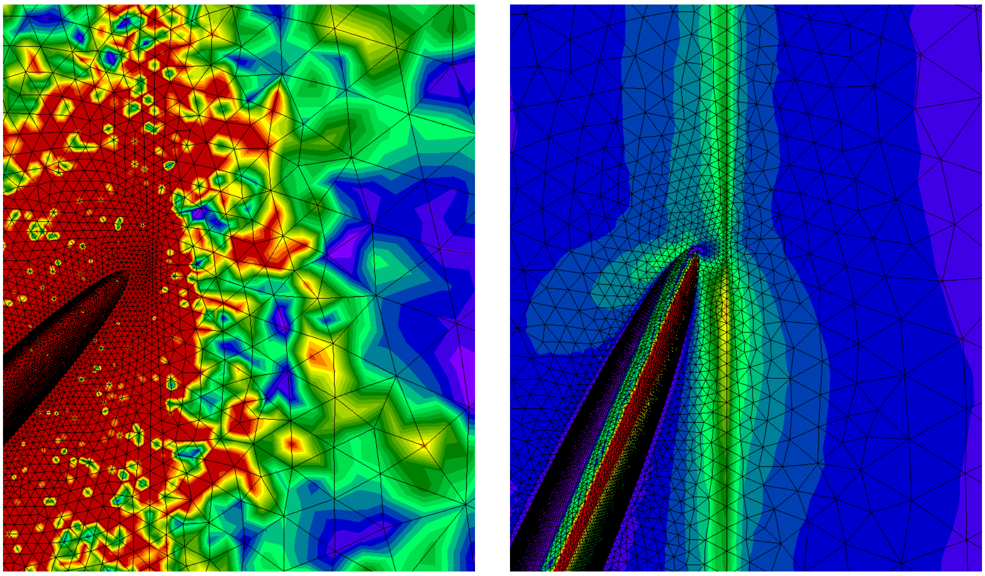

(a) Boundary conditions lead to nonphysical behavior of the stress.

(b) Physical correct simulation.

Figure 6.3: Resulting von Mises stress for two different geometries, applied stress is $\mathbf{1}_{yz}$.

deavor. The forces applied to opposite surfaces have to be in an equilibrium. Even the slightest deviations resulting from rounding or numerical approximations can lead to physical incorrect results of the simulation. The resulting von Mises stress for a simulation with such a slight deviation in the boundary conditions is shown in Figure 6.3a. The stress in the area around the crack is unrealistically high and as we go further out, the stress diverges from node to node. It is evident that these simulations are incorrect when compared to simulations exhibiting physically plausible behavior, as demonstrated in Figure 6.3b. Both simulations utilize the stress tensor $\mathbf{1}_{yz}$ and share the same range of the von Mises stress displayed. In the simulation with correct behavior, the resulting von Mises stress exhibits a smooth and consistent slope.

The simulations that show the nonphysical behavior are easy to identify. With a threshold level for the shear stress most of these simulations can be identified. Furthermore, we check the deviation in stress components between adjacent nodes, and if this deviation surpasses a certain threshold. If either of these criteria are met, we choose to rerun the simulation, employing an alternative random seed for the meshing process. With this remeshing

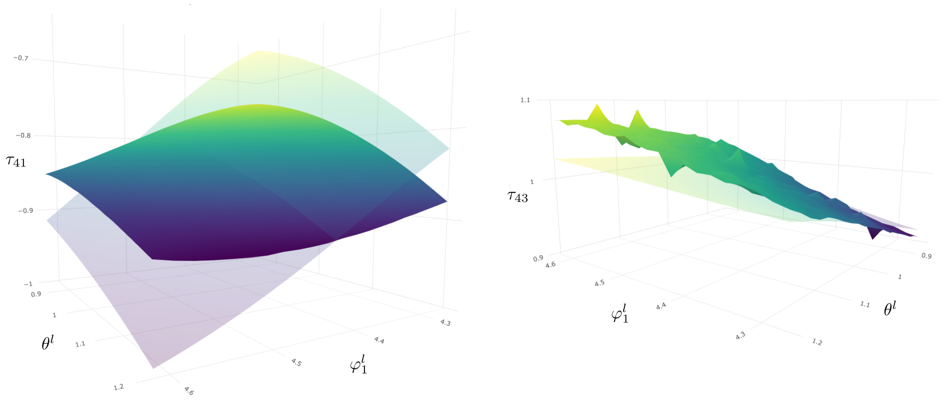

(a) Shear stress induced by $\mathbf{1}_{zx}$.

(b) Shear stress induced by $\mathbf{1}_{yz}$.

Figure 6.4: FEM results for the shear stress in one slip system over different orientations of the left grain. The orientation of the right grain is fixed. With cracked left grain in opaque and with intact left grain transparent. The cracked slip system is fixed.

process the structure of the mesh on the cracked surface changes. This can lead to a smaller rounding error. In all calculations double precision is used, but even the small rounding errors resulting from this precision have an impact on the FEM simulations.

It is noteworthy that only a small fraction, approximately 0.5%, of the simulations met the criteria for a rerun, and importantly, all the simulations that underwent a rerun successfully passed the subsequent consistency check.

The evaluation of the FEM simulations in the same manner as in Section 4.3.2 shows that this rerun process reduces the noise in the results but only up to a certain level. Here we choose a fixed orientation of the right grain with $\varphi_1^r = 3.41, \theta^r = 3.6$ and $\varphi_2^r = 0.94$. For the left grain $\varphi_1^l \in [4.27, 4.62], \theta^l \in [0.86, 1.21]$ and $\varphi_2^l = 6.05$.

In Figure 6.4, the resulting shear stress in one slip system of the right grain for two different stress tensors are shown. On the left (Figure 6.4a) $\mathbf{1}_{ZX}$ is applied. Both shear stresses, the one with crack in the left grain (opaque) and the one without (transparent) follow in a smooth graph. It shows that the crack in the left grain not always results in an increase in shear stress in the slip systems of the infected grain. The simulations, where the boundary conditions are applied to the cracked surface, like in Figure 6.4b, in comparison are slightly more noisy. Here the resulting shear stress for $\mathbf{1}_{YZ}$ is shown. The simulations without cracked left grain result in a smooth graph. But in the simulations with a crack, we can see that the rerun process can not totally eliminate the noise. Nevertheless, the results overall are accurate enough for building the infection model.

6.2.4 The Surrogate Models

With the stress decomposition we have to run six simulations per geometry, and we now have seven geometries instead of two. So simulational effort for one pair of angles increases compared to the uniaxial case with a factor of 36. Therefore, it is not feasible to run simulations for as many angle pairs as for the uniaxial model.

To address this data limitation, we leverage the symmetric structure of the FCC lattice. With the rotation matrices given in equations (3.78), (3.79) and (3.80) the slips systems of a grain are mapped onto each other. Consequently, for a given orientation $\mathcal{E}$ and a given slip system $n_i(U(\mathcal{E})), s_{ij}(U(\mathcal{E}))$ rotation matrices are denoted as U_{ij} such that,

$$\begin{aligned} n_1(U(\mathcal{E}) \cdot U_{ij}) &= n_i(U(\mathcal{E})) \\ s_{11}(U(\mathcal{E}) \cdot U_{ij}) &= s_{ij}(U(\mathcal{E})), \end{aligned} \tag{6.8}$$

for $i \in \{1, \dots, 4\}, j \in \{1, 2, 3\}$. As we recall Section 3.2.1 is the compliance tensor of the material invariant under these rotations.

From the finite element analysis we gain, for each set of angles $(\mathcal{E}_l, \mathcal{E}_r, \alpha)$ and each stress component, 12 shear stresses $\tau_{ij}^{NC}(\mathcal{E}_l, \mathcal{E}_r, \alpha)$ left grain remains intact. When the left grain is cracked, we acquire 144 shear stresses ${}_{km}\tau_{ij}^{WC}(\mathcal{E}_l, \mathcal{E}_r, \alpha)$, where $k \in 1, \dots, 4$ and $m \in 1, 2, 3$ represent the cracked slip system. Rather than training one model for each slip system we transform the orientations such that we only have to consider one slip system

$$\tau^{NC}\left(\mathcal{E}_l, \mathcal{E}(U(\mathcal{E}_r) \cdot U_{ij}), \alpha\right) = \tau_{ij}^{NC}(\mathcal{E}_l, \mathcal{E}_r, \alpha) \tag{6.9}$$

$$\tau^{WC}\left(\mathcal{E}(U(\mathcal{E}_l) \cdot U_{km}), \mathcal{E}(U(\mathcal{E}_r) \cdot U_{ij}), \alpha\right) = {}_{km}\tau_{ij}^{NC}(\mathcal{E}_l, \mathcal{E}_r, \alpha). \tag{6.10}$$

For the dataset we run simulations with 3000 random angles $(\mathcal{E}_l, \mathcal{E}_r, \alpha)$, which is a total 216000 FEM simulations. By taking advantage of rotational

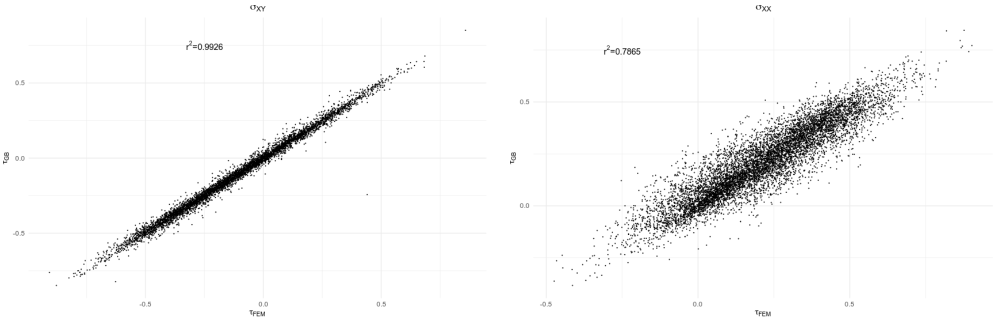

(a) Results of the gradient boosting tree for $\mathbf{1}_{xy}$

(b) Results of the gradient boosting tree for $\mathbf{1}_{xx}$

Figure 6.5: Predictions of the surrogate models over shear stress from the FEM simulations for different stress components.

symmetries, we expand the dataset to include a total of 432,000 data points per stress component.

We use gradient boosting trees, introduced in Section 4.3.3, as surrogate models for our infection function. The setup is almost the same as for the uniaxial case. But instead of training a model for each slip system, here we build a model for each of the 6 stress components. We use the α as an additional input

$$\hat{\tau}_k^{WC} = f_k(\mathcal{E}_l', \mathcal{E}_r', \alpha, \tau^{NC}),\ k \in I_\sigma, \tag{6.11}$$

here $\mathcal{E}_l' = \mathcal{E}(U(\mathcal{E}_l) \cdot U_{km})$ and $\mathcal{E}_r' = \mathcal{E}(U(\mathcal{E}_r) \cdot U_{ij})$.

The predictions made by the surrogate models on the test data are highly accurate for nearly all stress components. Figure 6.5a displays the predictions alongside the results from the FEM simulations for the stress component $\mathbf{1}_{xy}$. The other models exhibit nearly identical R^2 values, ranging from approximately 0.98 to 0.99, with one exception being the stress component $\mathbf{1}_{xx}$. The outcomes for this particular stress component are depicted in Figure 6.5b. Notably, this stress component represents the normal stress that is nearly perpendicular to the grain boundary, and it appears that the behavior of shear stress in this context is more complex.

In Figure 6.6 the von Mises stress obtained from the FEM simulations is shown. If the stress is applied parallelly to the grain boundary (Figure 6.6a and 6.6c), the crack increases the von Mises stress in the right grain. The crack direction has an impact on the von Mises stress. For a large angle

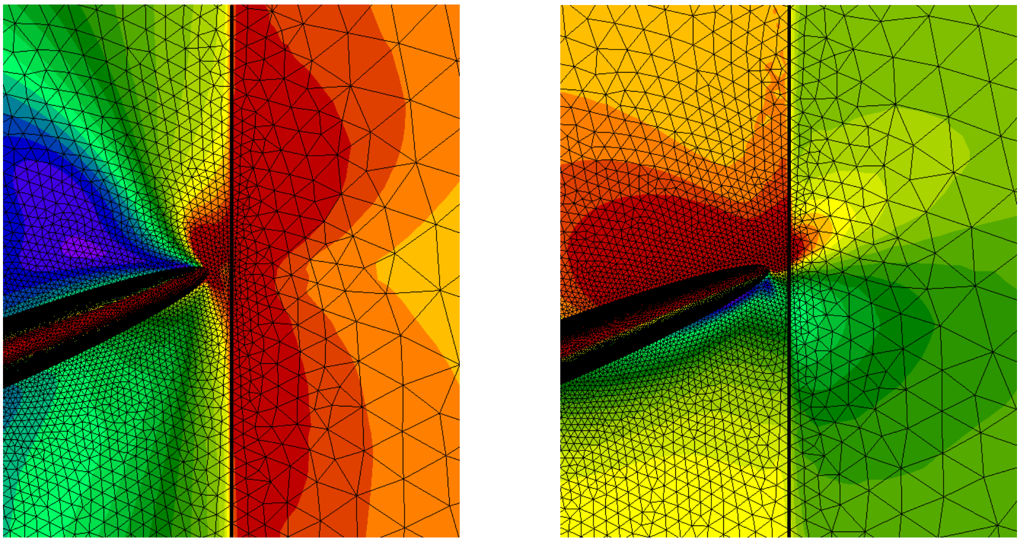

(a) Stress: $\mathbf{1}_{ZZ}$.

(b) Stress: $\mathbf{1}_{XX}$.

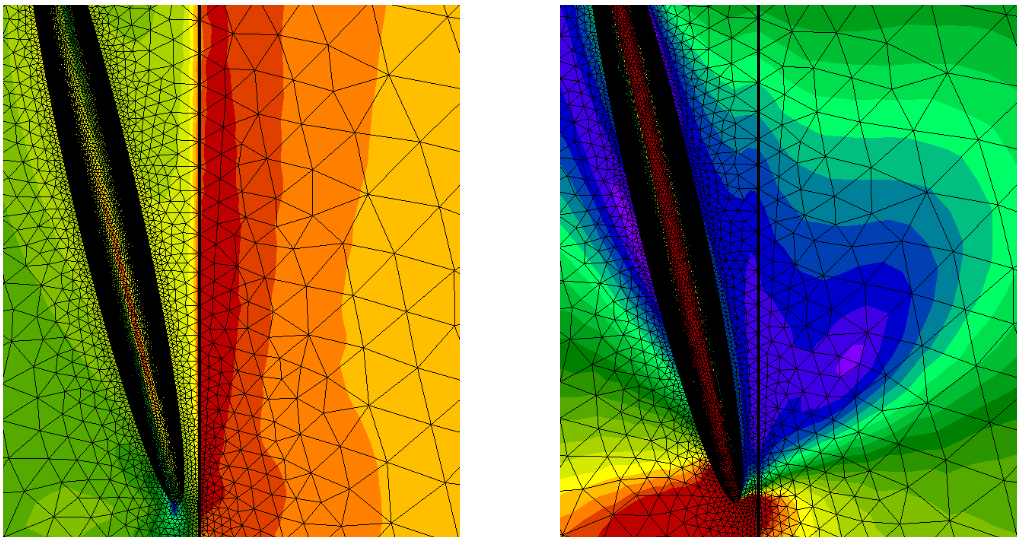

(c) Stress $\mathbf{1}_{ZZ}$.

(d) Stress $\mathbf{1}_{XX}$.

Figure 6.6: Von Mises stress in the region of the crack for different crack orientations and load directions. The grain boundary is the thick line.

between boundary and crack (Figure 6.6a), the resulting stress is higher compared to a smaller angle (Figure 6.6c). For the simulations with an applied normal load in x direction, perpendicular to the grain boundary, the influence of the crack direction is significantly higher. If the crack is almost perpendicular to the grain boundary (Figure 6.6b), the simulation shows that there are two areas at the tip of the crack in the right grain with different behavior. Slightly above the crack the stress increases, and below the von Mises stress reduces due to the crack. This effect becomes significantly larger if the angle between crack and grain boundary is small (Figure 6.6d) and the force acts almost perpendicular to the crack. Stress concentration at the crack tip leads to a reduction of stress in the area behind the crack face in the right grain. It seems that this complex behavior leads to the reduced accuracy for the normal load in x direction.

Nonetheless, with an R^2 value of nearly 0.8, the predictions for this stress component are sufficiently accurate.

6.2.5 Integration into the Percolation Model

The infection model requires an additional input parameter, which is the angle between the grain boundary and the surface normal. To obtain this angle, we sample a random value $\alpha_{g_1,g_2} \in [-10°, 10°]$ at the initiation of the surface for each grain boundary. Here, g_1 and g_2 denote the two adjacent grains sharing this common boundary.

Before applying the surrogate models for the infection function, we perform rotations on the stress tensor and grain orientations to align the grain boundary with the z-axis. Let g_l represent the cracked grain with orientation $\mathcal{E}_l$, and g_r and $\mathcal{E}_r$ represent the grain and orientations of the adjacent grain on which the infection function is to be applied. Additionally, let σ_{iso} denote the isotropic stress acting on the entire surface and $\sigma_{ani}^{g_r}$ be the anistropic stress in grain g_r. Utilizing Voronoi tessellation, we can determine the angle β_{g_l,g_r} as illustrated in Figure 6.7.

Let now $U_{\beta_{g_l,g_r}}$ be the rotation matrix that describes a rotation of β_{g_l,g_r} around the y-axis which is given by

$$U_{\beta_{g_l,g_r}} = \begin{pmatrix} \cos(\beta_{g_l,g_r}) & 0 & \sin(\beta_{g_l,g_r}) \\ 0 & 1 & 0 \\ -\sin(\beta_{g_l,g_r}) & 0 & \cos(\beta_{g_l,g_r}) \end{pmatrix}. \tag{6.12}$$

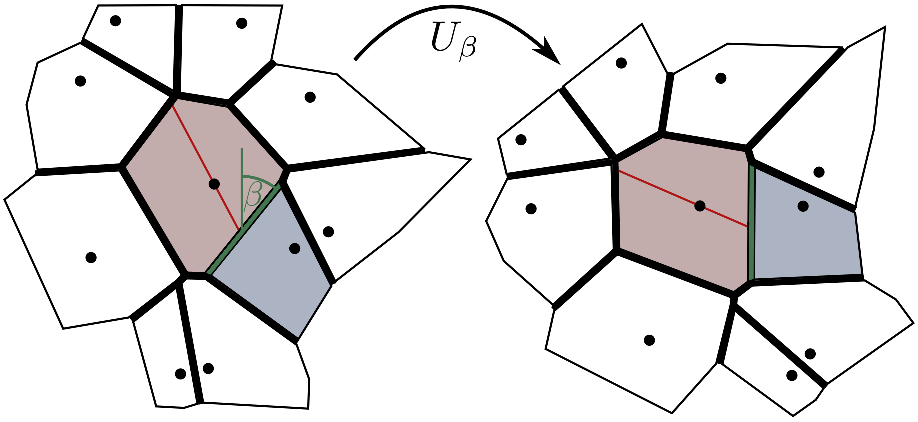

Figure 6.7: Rotation of the whole system, such that the grain boundary (green) between the cracked grain (red) and the infected grain (blue) is aligned with the z-axis.

The grains and the stresses are transformed with this rotation,

$$\bar{\sigma}_{iso} = U_{\beta_{g_l,g_r}} \cdot \sigma_{iso} \cdot U^T_{\beta_{g_l,g_r}} \tag{6.13}$$

$$\bar{\sigma}^{g_r}_{ani} = U_{\beta_{g_l,g_r}} \cdot \sigma^{gr}_{ani} \cdot U^T_{\beta_{g_l,g_r}} \tag{6.14}$$

$$\bar{\mathcal{E}}_l = \mathcal{E}(U(\mathcal{E}_l) \cdot U_{\beta_{g_l,g_r}}) \tag{6.15}$$

$$\bar{\mathcal{E}}_r = \mathcal{E}(U(\mathcal{E}_r) \cdot U_{\beta_{g_l,g_r}}). \tag{6.16}$$

Let now k, m be the indices slip system of grain g_r that the infection function is applied to. We calculate the shear stress parts in the slip system that are induced by the stress components $\mathbf{1}_s, s \in I_\sigma$

$$\tau^s_{km} = n_k \cdot \mathbf{1}_s \cdot t_{km}. \tag{6.17}$$

Additionally, let i, j be the indices slip system that is cracked in grain g_l. We rotate both grains so that the slip systems align with the ones used for building the surrogate model. Therefore, the final orientations of the grains used in the infection function are given by:

$$\begin{aligned} \bar{\mathcal{E}}^{ij}_l &= \mathcal{E}(U(\bar{\mathcal{E}}_l) \cdot U_{ij}) \\ \bar{\mathcal{E}}^{km}_r &= \mathcal{E}(U(\bar{\mathcal{E}}_r) \cdot U_{km}) \end{aligned}. \tag{6.18}$$

For each slip system with indices k, m the shear stress after infection is now

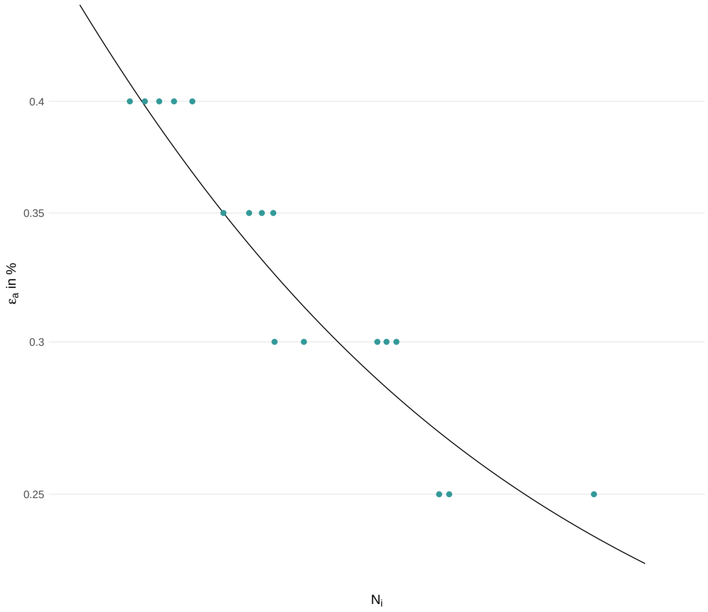

Figure 6.8: Fit of the Coffin Manson Basquin equation to the experimental data.

given by,

$$\hat{\tau}_{km} = \sum_{s \in I_\sigma} (\bar{\sigma}^{g_r}_{aniso})_s \cdot f_s(\bar{\mathcal{E}}^{ij}_l, \bar{\mathcal{E}}^{km}_r, \alpha_{g_l, g_r}, \tau^s_{km}). \tag{6.19}$$

6.3 Fitting the Model

For the calibration of the multiaxial model we utilize the data from the experiments with Alloy427 under uniaxial load as described in Section 2.7.

We initially fit the Coffin-Manson-Basquin equation to the experimental failure times, as illustrated in Figure 6.8.
The fitting process for the parameters s_{CMB} and K_{crit} is the same as for the uniaxial model, as described in Section 4.5.1.
Figure 6.9 displays the resulting probability density functions of failure times for various strain levels. The model appears to be capable of describing the scatter in the experimental data for the lower strain levels quite well. However, at the higher strain levels (0.35% and 0.4%), the predicted probability density is slightly shifted to the left. In these cases, the scatter

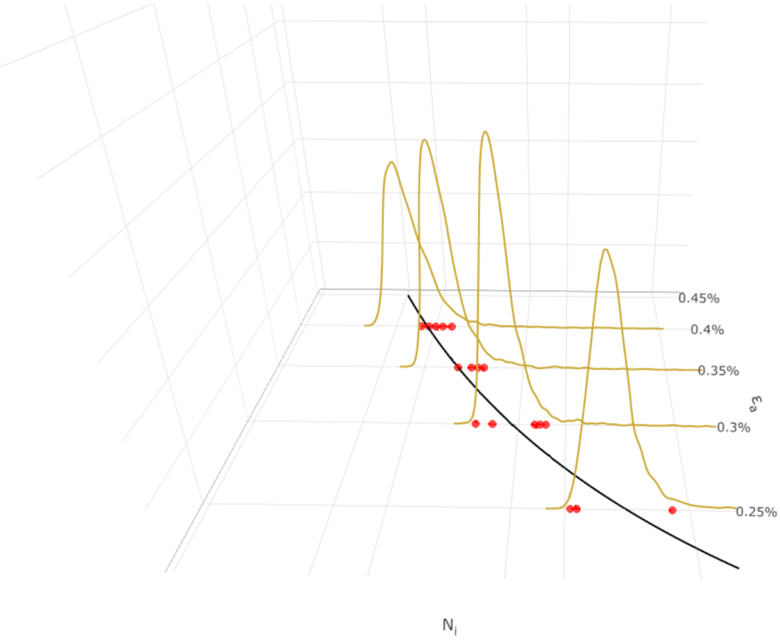

Figure 6.9: Density of the probability of failure (yellow) for the different strain levels under uniaxial load. Experimental data (red) and pre fitted Coffin Manson Basquin equation (black).

band of the experiments is very small compared to the probability density.

6.4 Experimental Validation

For the validation of the model we use the experimental LCF data with Alloy247 under multiaxial load (see Section 2.7).

The multiaxiality measure κ_σ, introduced in [52], is used to quantify the degree of multiaxial stress. For a stress tensor σ, this value is defined as:

$$\kappa_\sigma = \frac{|\sigma'_{III} - \sigma'_{II}|}{|\sigma'_I|}, \tag{6.20}$$

here σ'_I, σ'_{II}, and σ'_{III} represent the principal stress values of σ without the hydrostatic stress component.

When the stress is purely uniaxial, $\sigma'_{II} = \sigma'_{III}$, resulting in $\kappa_\sigma = 0$. On the other hand, $\kappa_\sigma = 1$ if the absolute stress difference between σ'_{II} and σ'_{III} is equal to $|\sigma'_I|$. In other words, κ_σ quantifies how far the stress state is

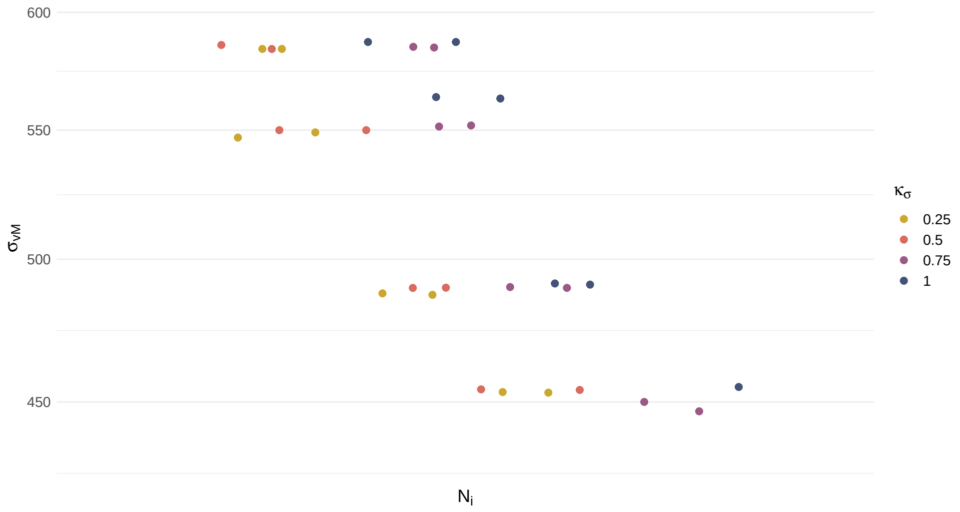

Figure 6.10: Experimental LCF data for different von Mises stress and different levels of multiaxiality.

from being purely uniaxial, with higher values indicating a greater degree of multiaxiality.

The experimental results are depicted in Figure 6.10. It is evident that increasing values of κ_σ correspond to longer LCF life of the specimens. This effect is observed across various stress levels.

We use the geometry parameters from the specimen for the percolation simulations. For the stress we use a mixture of normal stress σ_{zz} and shear stresses $\sigma_{zx} = -\sigma_{yz}$. As the final input we use the tensor without hydrostatic stress, which leads to a stress tensor of the form

$$\sigma = \begin{pmatrix} -1/3\sigma_{zz} & 0 & \sigma_{zx} \\ 0 & -1/3\sigma_{zz} & -\sigma_{zx} \\ \sigma_{zx} & -\sigma_{zx} & 2/3\sigma_{zz} \end{pmatrix}. \tag{6.21}$$

For each combination of σ_{vM} and κ_σ we run 1000 simulations. The resulting density functions of the PoF are illustrated in Figure 6.11.

We can observe that for $\kappa_\sigma = 0$ (yellow), even if we change the specimen geometry, the model predicts failure times in the right order of magnitude. It is not necessary to refit the model for different geometries.

However, when we compare the simulation results for different κ_σ values with the experimental results, the model fails to capture the shift in LCF life accurately. Instead of an increase in failure times, the probabilities of

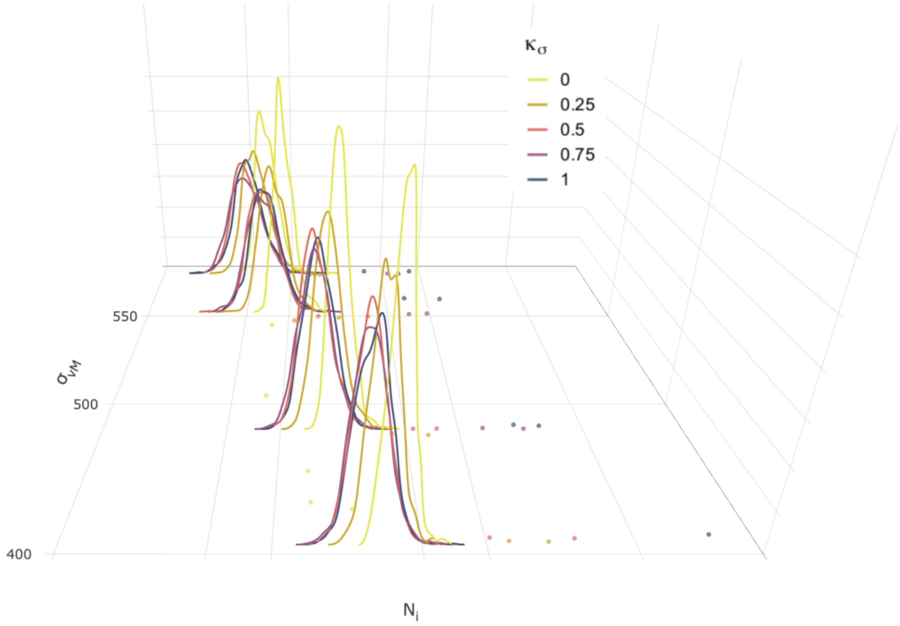

Figure 6.11: Density function of the probability of failure for different σ_{vM} and different levels of multiaxiality.

failure shift to the left as the level of multiaxiality increases. Moreover, for higher levels of κ_σ, the scatter in the simulation results also increases. Due to the limited amount of data available, we are unable to determine whether this effect is also present in the experiments.

If we compare the distribution of the maximum Schmid factors for the different stresses (Figure 6.12a), we can see that an increase in κ_σ leads to over all higher Schmid factors. Due to this effect the single grains tend to crack earlier. Additionally, the infection of the grains starts earlier as well. This over all leads to the reduction of the LCF lifetime in the model.

The multiaxiality of the stress has an effect on the stress intensity factor, which we use as a failure criterion. In Figure 6.12b K_{eq} for a crack with a length $3mm$ for the different stress inputs over the angle between x-axis and the crack is shown. Here we can see two effects, on the one hand for increasing multiaxiality the crack direction becomes less important until for $\kappa_\sigma = 1$ the equivalent stress intensity is independent of the crack direction. On the other hand, the maximum possible stress intensity at the tip of the crack decreases. This effect on its own would lead to an increase in the LCF

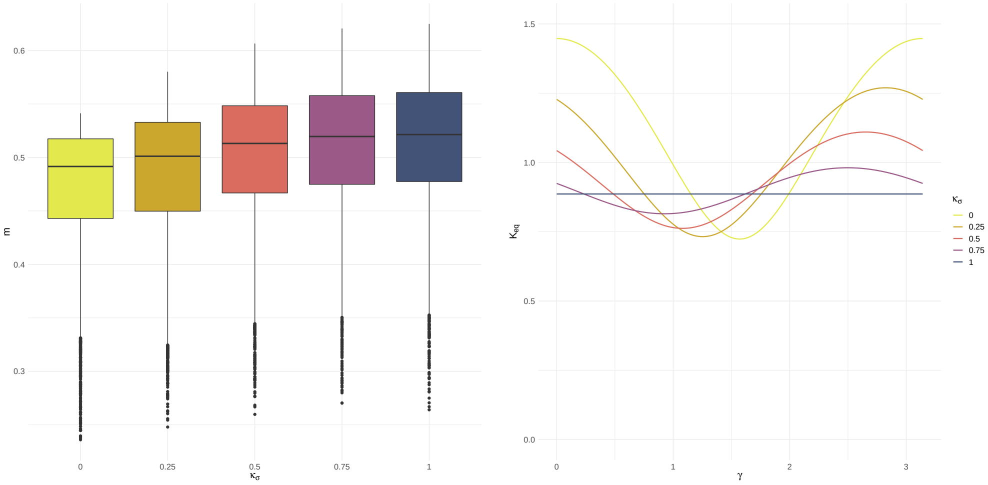

(a) The distribution of the maximum Schmid factors shift to larger values for higher levels of multiaxiality.

(b) The maximal equivalent stress intensity factor becomes smaler for higher values of κ_σ. The direction of the crack becomes less import.

Figure 6.12: Schmid factors and equivalent stress intensity factor for different values of multiaxiality.

lifetime and a broader scatter band of the results (compare Figure 4.17). This both effects combined match with the results from the percolation simulations. The increase of the Schmid factors shift the results to the left and increase in the scatter is due to the reduced stress intensity. Both effects are stronger for lower values of κ_σ, and for the values above 0.5 the increase of the maximum Schmid factors is pretty low. The density function of the PoF show the same behavior, for κ_σ between 0 and 0.5 the probability distribution differ clearly, but for the higher values this difference diminishes.

6.4.1 Empirical shift

To address the discrepancy between the predicted failure times and the results from the experiments for the multiaxial loading states, we introduce an empirical shift of the Coffin Manson Basquin equation. To account for the longer LCF lifetime with increasing level of multiaxiality, we use the linear function

$$s(\kappa) = 1 + a\,\kappa \tag{6.22}$$

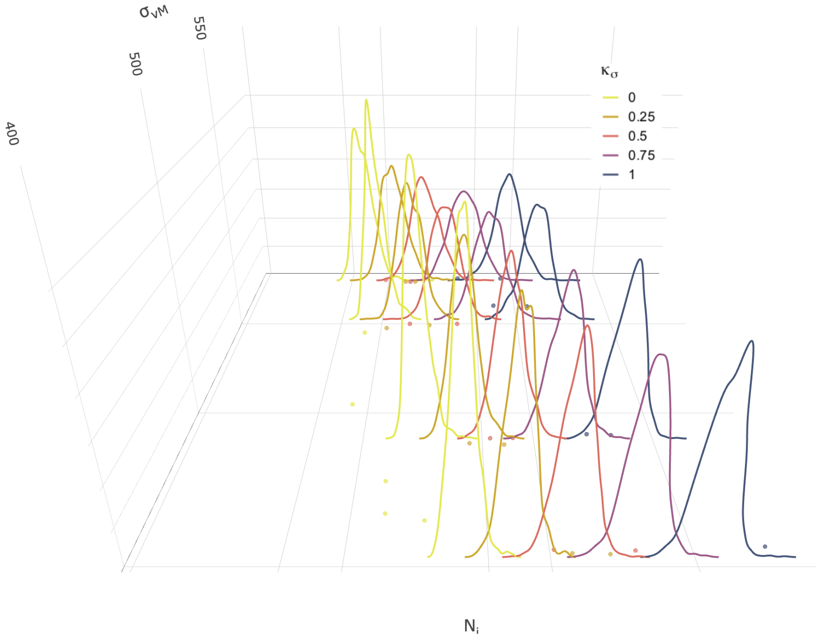

Figure 6.13: Density function of the probability of failure for different σ_{vM} and different levels of multiaxiality.

for the shift. We apply the shift to the single grain crack initiation times via

$$\mathrm{CMB}_s^{-1}(\varepsilon, \kappa) = \mathrm{CMB}^{-1}(\varepsilon) \cdot s(\kappa). \tag{6.23}$$

We use the parameter a to fit the percolation model to the experimental results. Therefore, we employ the MLE method and solve the optimization numerically.

The resulting densities of the probability of failure are shown in Figure 6.13. Due to the empirical shift, the resulting failure probability show the same behavior for increasing levels of multiaxiality κ as the experiments. It seems that the range of scatter is in the right order of magnitude, but for an accurate estimation there are not enough data points available.

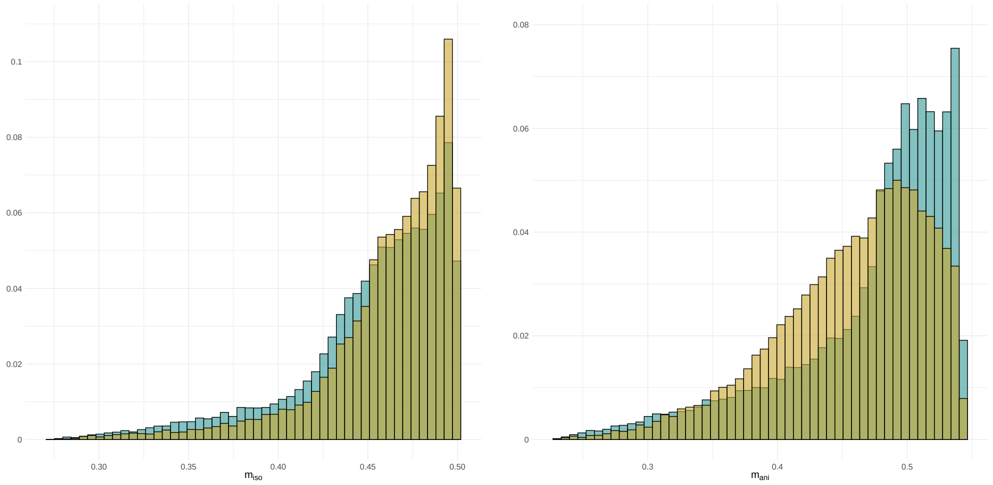

(a) The Schmid factors are calculate with the global isotropic stress.

(b) Here we use the anistropic stress in the grain to calculate the Schmid factor.

Figure 6.14: Distribution of the Schmid factors for orientations sampled according to the Haar measure (green) and according to $\hat{g}$ (yellow).

6.5 Comparison of the Different Orientation Distributions

In this section we investigate the impact of the different distributions for the grain orientations on the percolation model. We compare the distribution from Section 5.1 with the isotropic distributed orientations gained from the Haar measure.

6.5.1 Schmid Factors

Grain orientation affects Schmid factors in two distinct ways. Firstly, it determines the direction and orientation of the slip systems directly. Secondly, it influences the anisotropic stress due to its impact on the stiffness tensor. To make a comparison, we utilize 30,000 orientations obtained from the Metropolis-Hastings algorithm with the density function $\hat{g}$, as well as 30,000 orientations distributed according to the Haar measure.

Initially, we focus solely on the slip systems. Thus, we calculate the maximum Schmid factors with equation 4.6 resulting from the shear stress using an isotropic uniaxial stress:

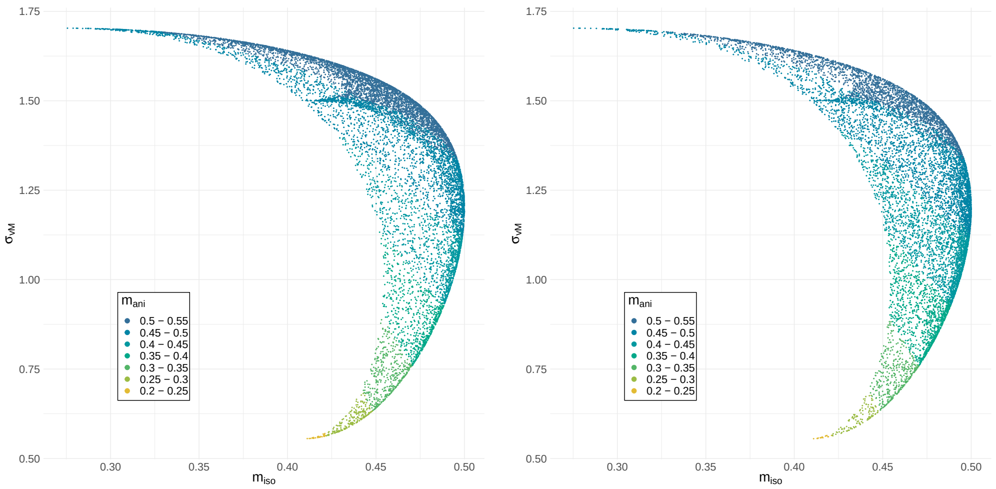

(a) Orientations sampled from the Haar measure. Higher concentration of values on the right edge.

(b) Orientations sampled from $\hat{g}$. Slightly lower concentration on the right edge.

Figure 6.15: Von Mises equivalent stress over Schmid factor from the isotropic stress. Color coding gives the Schmid factor resulting from anisotropic stress.

$$\hat{\tau}_{ij}(U) = n_i(U) \cdot \sigma_{iso} \cdot s_{ij}(U). \tag{6.24}$$

Figure 6.14a illustrates the distribution of Schmid factors for both cases. It shows that grains with orientations sampled from $\hat{g}$ tend to have slightly higher Schmid factors compared to grains without a preferred orientation.

However, when we consider the anisotropy of the stiffness tensor, i.e., replacing the isotropic stress with the anisotropic stress (equation (4.4)), this difference is reversed. Figure 6.14b demonstrates that the number of Schmid factors with values above 0.475 is significantly reduced with preferred orientation. Conversely, the number of Schmid factors falling between 0.35 and 0.475 increases with a preferred orientation.

In Figure 6.15 the Schmid factor resulting from the isotropic stress, the von Mises equivalent stress and the Schmid factor from the isotropic stress are illustrated. Here we can see that for a high anisotropic Schmid factor the direction of the slip system and the stiffness in load direction both play an important role for the Schmid factor resulting from the anistropic

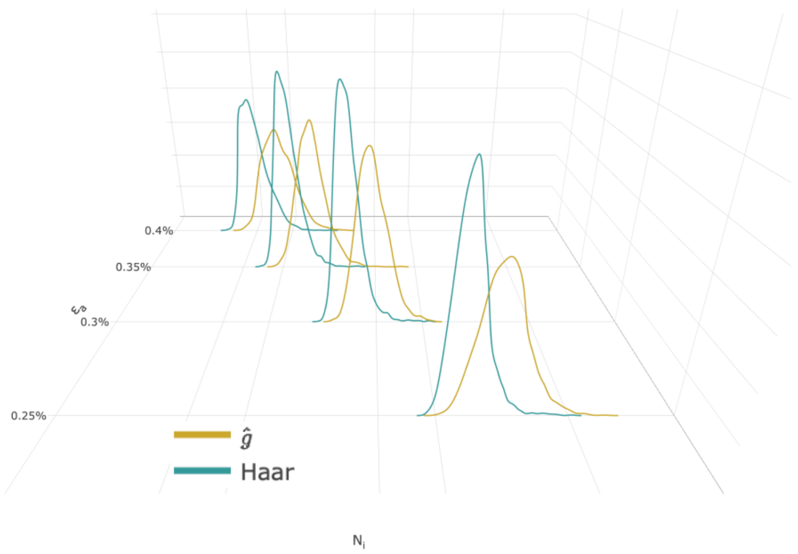

Figure 6.16: Comparison of the probability densities of the probabilities of failure for the different orientational distributions with logarithmic scaled axes.

stress. When comparing the results from isotropically distributed grains (Figure 6.15a) with those from $\hat{g}$ (Figure 6.15b), we notice that in both cases, there is a higher density of values on the right edge of the distribution, indicating a combination of a high isotropic Schmid factor and high stiffness in the load direction. However, this effect is more distinct in the orientations sampled from the Haar measure. This explains the different results for the isotropic and anisotropic stress.

6.5.2 Percolation with different Orientational Distributions

This difference in the Schmid factors influences the results from the percolation model. We compare the results that we use to fit the model with the same amount of simulations where the orientations of the grains are distributed according to $\hat{g}$. The fitted parameters remain the same.

Figure 6.16 depicts a side-by-side comparison of the probability of failure for both orientation distributions. The influence of grains with a preferred orientation is significant. Simulations across all strain levels demonstrate a longer LCF lifetime when compared to the isotropic distribution. Additionally, the scatter band of the density function of the probability of failure widens as well.

Both effects can be well explained with the distribution of the Schmid factors (Figure 6.15b). Surfaces with orientations sampled from the Haar measure are more likely to contain many grains with high Schmid factors, leading to earlier crack initiation. This, combined with the infection process, results in a greater number of distinct grains from which a cluster can propagate, ultimately leading to overall earlier failure.

7. Application to a Turbine Blade

The aim of this section is to estimate the probability of failure to a complex 3D component. In contrast to the test specimens, a realistic mechanical component in operation is subject to an inhomogeneous stress field that can only be computed numerically. To achieve this, we utilize the crack initiation process introduced in Section 3.3. The percolation simulations are employed to determine stress- and cycle-dependent local cumulative hazard rates.

7.1 Linear Hazards

Using the fitted multiaxial model introduced in Section 6, we examine the impact of different surface sizes on the probability of failure. In this regard, we maintain a fixed stress tensor as input while varying the surface size. The average grain diameter remains constant throughout the analysis.

We choose quadratic surfaces with four different sizes 350 mm^2, 450 mm^2, 550 mm^2 and 650 mm^2. For each of these surfaces 12000 simulations are performed. With the resulting failure times $\hat{N}^n_{i_A}, n \in 1, \dots, 12000$ for each area A we obtain an approximation for the survival probability by

$$S_A(N_i, \sigma) = \frac{\#\{\hat{N}^n_{i_A} | \hat{N}^n_{i_A} > N_i, n = 1, \dots, 12000\}}{12000}. \tag{7.1}$$

As $F_A(N_i, \sigma) = 1 - S_A(N_i, \sigma)$ holds, with theorem 3.33 the cumulative hazard function is given by

$$H_A(N_i, \sigma) = -\log S_A(N_i, \sigma). \tag{7.2}$$

If the crack initiation processes in distant regions are independent, this

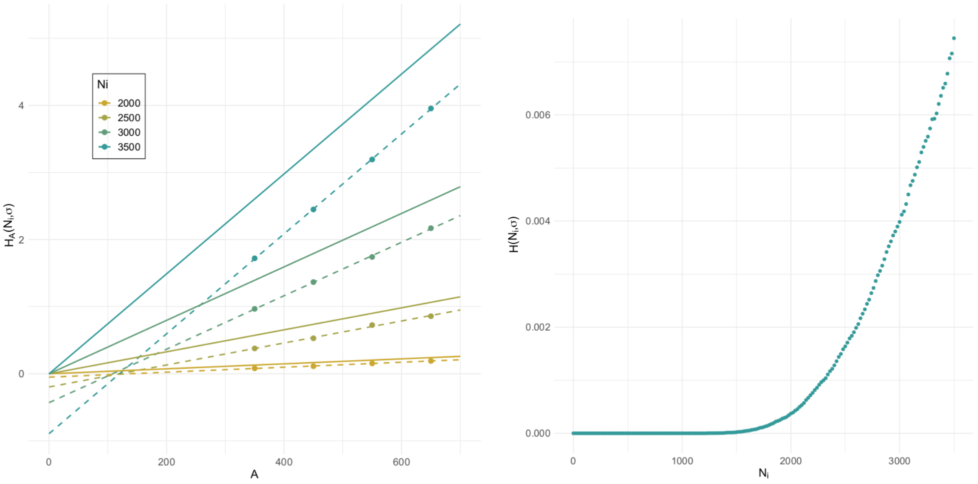

(a) Cumulative hazard function for different load cycles. The points show the simulation results with dotted regression lines. The solid lines represent the cumulative hazards that we use for the application.

(b) Local cumulative hazard rate over the load cycles, obtained from the regression lines in Figure 7.1a.

Figure 7.1: Results of the simulations for different surface sizes.

leads to an exponential decay of the survival probability with respect to the area. Therefore, with equation (7.2) the cumulative hazard are linear.

The results from the simulations for the four different surface sizes are illustrated in Figure 7.1a. The points in the figure represent the cumulative hazards for the stress and load cycles.

Here we can see that the cumulative hazards are approximately linear with respect to the surface area, as they closely align with the dotted regression lines. We use the slopes from the regression lines as the local cumulative hazard rate

$$H(N_i, \sigma) = \frac{H_A(N_i, \sigma)}{|A|} \tag{7.3}$$

which leads to the cumulative hazards plotted as the solid lines.

The shift in hazards resulting in a slight overestimation of the probabilities of failure is not a significant issue in the context of safety-critical applications, such as real gas turbines. In fact, it is generally preferable to err on the side of caution and overestimate failure probabilities in such critical systems to

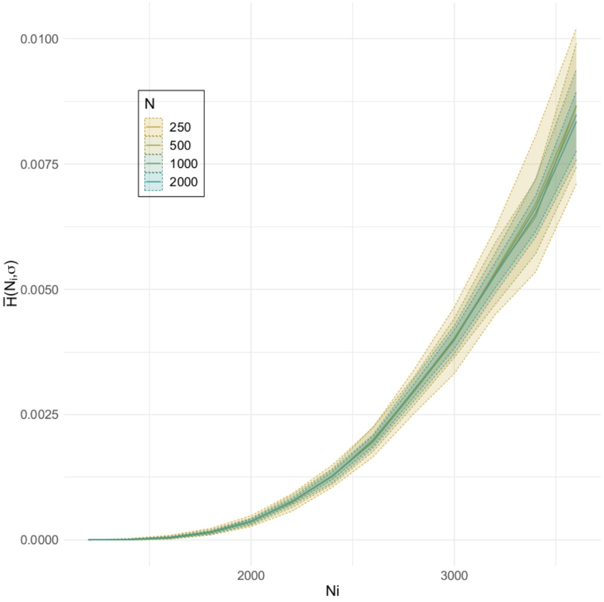

Figure 7.2: Standard deviations of the hazard rates for different number of simulations

ensure safety and reliability.

In Figure 7.1b the local cumulative hazard rate over the load cycles is depicted. The first observed failure in the simulations occurring at load cycle 1041. Prior to this cycle, the hazard density is zero. Notably, $H(N_i, \sigma)$ exhibits exponential growth until approximately load cycle 2500, from which point onward its growth becomes nearly linear. This behavior suggests that the hazard density evolves over time, transitioning from an initial exponential growth phase to a more linear trend.

In the following we build a surrogate model for the local hazard rate. Therefore, we have to gather a database for different stress states from the percolation model. Due to computational limitations it is not feasible to run as many simulations for each stress state and surface size as in this section.

We have to make a trade of between the number of the simulations and accuracy of the obtained local hazard rates. With subsamples of the simulations we investigate the scatter band of the hazard rates for different amounts of simulations per surface area. In Figure 7.2 the standard deviations for $250, 500, 1000$ and 2000 simulations per area are depicted.

Since the difference in results between 1000 and 2000 simulations is minimal

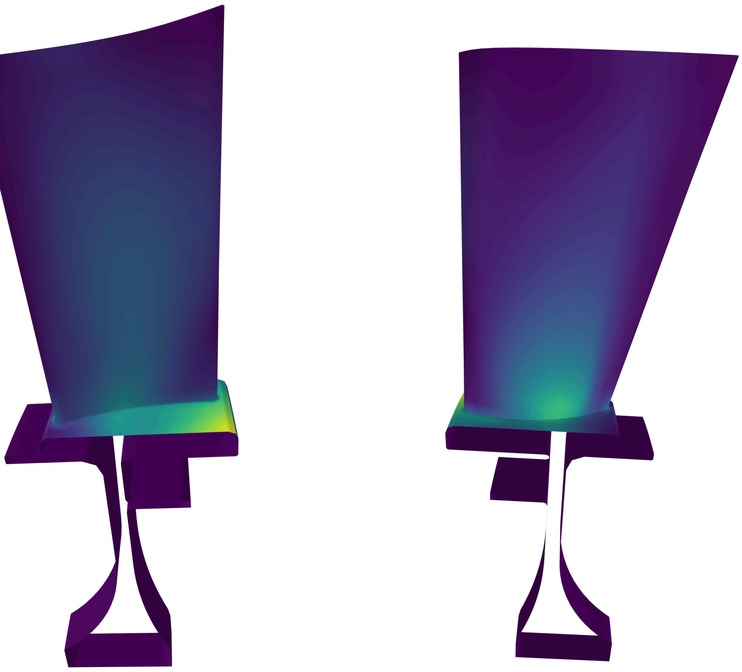

(a) Front side of the turbine blade.

(b) Back side of the turbine blade.

Figure 7.3: Von Mieses stress on the turbine blade under centrifugal loading.

compared to the difference between 500 and 1000 simulations, we have opted to use 1000 simulations per surface area in the following.

7.2 Blisk-Geometry and Surfaces Stress

As an example for the transfer to a component, we use an FEM model of a turbine blade. The geometry is discretized with 1838 quadratic brick elements and contains 13682 nodes. For a meshing study we refer to [29]. We consider here a centrifugal load from a rotation with 55Hz resulting in a volume force. Surface loads induced by air pressure are not taken into account.

We need to define the range of the inputs from which we generate the database for the surrogate model. To this end we calculate with equation (3.60) the surface force σ^{F_i}, for each surface element $F_i \in \mathcal{N}_h$. The

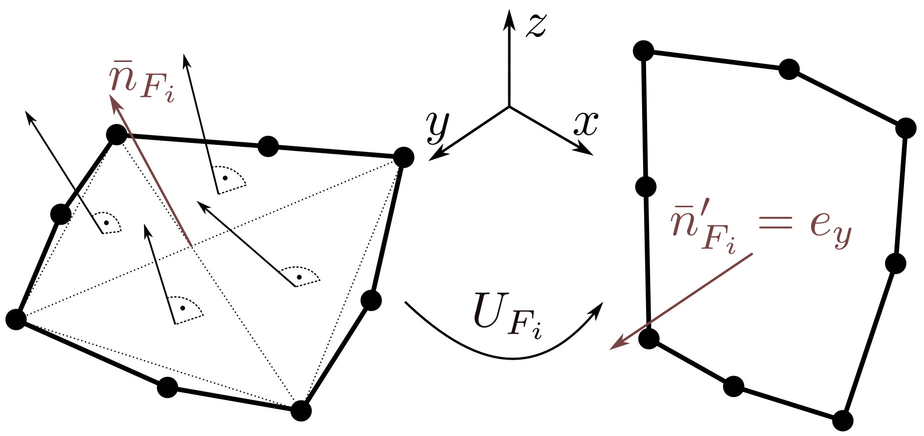

Figure 7.4: Rotation of the surface such that the average normal is aligned with the y-axis.

resulting von Mises stress of the component is illustrated in Figure 7.3. For the use in the percolation model, it is necessary to rotate the surface stresses such that the normal of the surface is aligned with the y-axis. The four corner nodes of the face F_i are usually not coplanar. Accordingly, we calculate the four normals from the planes that contain just three of the corner nodes. We use the average of the four normals as an approximation for the normal $\bar{n}^{F_i}$ of F_i, as illustrated in Figure 7.4. The rotation matrix that maps the normal $\bar{n}^{F_i}$ onto e_y is given by

$$U_{F_i} = g^Z_\beta \cdot g^X_\alpha, \text{ with } \alpha = \arctan\left(-\frac{\bar{n}^{F_i}_z}{\bar{n}^{F_i}_y}\right), \beta = \arctan\left(\frac{\bar{n}^{F_i}_x}{\bar{n}^{F_i}_y}\right), \tag{7.4}$$

for $\bar{n}^y_{F_i} \neq 0$. For the rotated surface stress we obtain

$$\bar{\sigma}^{F_i} = U_{F_i} \cdot \sigma^{F_i} \cdot U^T_{F_i}. \tag{7.5}$$

We use grain orientations that are distributed according to the Haar measure. With these orientations the percolation model is invariant under rotations around the y-axis. Accordingly, we can simplify the stress tensor by an additional rotation such that $\hat{\sigma}^{F_i}_{xy} = 0$. The corresponding rotation matrix is obtained by

$$\begin{aligned} U_{\sigma^{F_i}} &= g^Y_\gamma, \text{ with } \gamma = \arctan\left(\frac{\bar{\sigma}^{F_i}_{xy}}{\bar{\sigma}^{F_i}_{yz}}\right), \bar{\sigma}^{F_i}_{yz} \neq 0, \\ \hat{\sigma}^{F_i} &= U_{\sigma^{F_i}} \cdot \bar{\sigma}^{F_i} \cdot U^T_{\sigma^{F_i}}. \end{aligned} \tag{7.6}$$

Finally, as the hydrostatic stress is negligible, the stress tensor only contains four independent values $\hat{\sigma}^{F_i{}'}$

$$\hat{\sigma}^{F_i{}'} = \begin{pmatrix} \hat{\sigma}_{xx}^{F_i{}'} & 0 & \hat{\sigma}_{zx}^{F_i{}'} \\ 0 & \hat{\sigma}_{yy}^{F_i{}'} & \hat{\sigma}_{yz}^{F_i{}'} \\ \hat{\sigma}_{zx}^{F_i{}'} & \hat{\sigma}_{yz}^{F_i{}'} & \hat{\sigma}_{zz}^{F_i{}'} \end{pmatrix}, \text{ with } \hat{\sigma}_{xx}^{F_i{}'} + \hat{\sigma}_{yy}^{F_i{}'} = \hat{\sigma}_{zz}^{F_i{}'}. \tag{7.7}$$

7.3 Surrogate Model for the local cumulative Hazard rate

With this setup we choose 4000 simulations per stress state to obtain the Hazard density from the percolation model. One of these simulations runs on average 10 minutes, depending on the surface size. It is not feasible to perform these simulations for different geometries or loading conditions. Even just the geometry that we use as an example with one load state would require $7.3 \cdot 10^6$ simulations.

Therefore, it is necessary to build a surrogate model that predicts the hazard density from the surface stress and the load cycles.

7.3.1 Generation of the Database

To generate stress inputs for the percolation model, we employ a Latin hypercube sampling approach. The stress tensor's allowable range for each component is defined as:

$$\sigma_{kl} \in [0.95 \cdot \min_{F_i \in \mathcal{N}_h} \left(\hat{\sigma}_k^{F_i{}'}\right), 1.05 \cdot \max_{F_i \in \mathcal{N}_h} \left(\hat{\sigma}_k^{F_i{}'}\right)], \tag{7.8}$$

with $k \in \{xx, yy, yz, zx\}$. Additionally, we constrain the von Mises stress to lie within the range $[340, 600]$. Lower von Mises stress values result in minimal crack initiation cycles exceeding 20 000. A total of 300 stress inputs are sampled from this hypercube.

These stress tensors serve as input to the percolation model. We follow the same procedure for computing hazard densities as outlined in Section 7.1. For each surface size, 1 000 simulations are performed, resulting in a total of 1.2 million simulations. To expedite this extensive computation, we

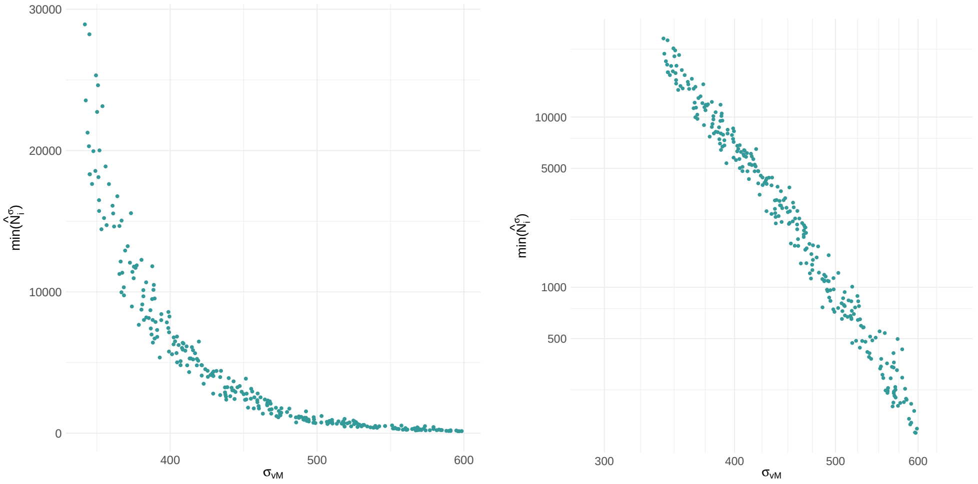

(a) Load cycle over von Miese equivalent stress.

(b) Load cycle over von Miese equivalent stress in a log-log-plot.

Figure 7.5: First load cycle such that the hazard density is greater than 0.

employed up to 125 cores from Intel® Xeon® Gold 6138 Processor which run with a single core frequency of 3.7 GHz. With this hardware we can run 250 simulations simultaneously. The overall computation taking approximately one month to complete.

Figure 7.5 depicts the minimal load cycle $N_i^f = \min(N_i(\sigma))$ over the von Mises stress. Figure 7.5b displays the same data with both axes on a logarithmic scale, highlighting the strong correlation between von Mises stress and the minimal load cycle for crack initiation.

7.3.2 The Model

To construct the surrogate model for hazard densities, we follow a two-step approach. Initially, we exploit the linear correlation between the logarithmic minimal load cycle and the von Mises stress to build a regression model.

The results from Section 6.4 show that additionally to the von Mises stress also the multiaxial influences the failure times. We take that into account by using the whole stress state for the regression. We obtain the best results with a linear model that predicts the logarithm of the first load cycle for which the hazard is greater than zero from the logarithm of the von Mises

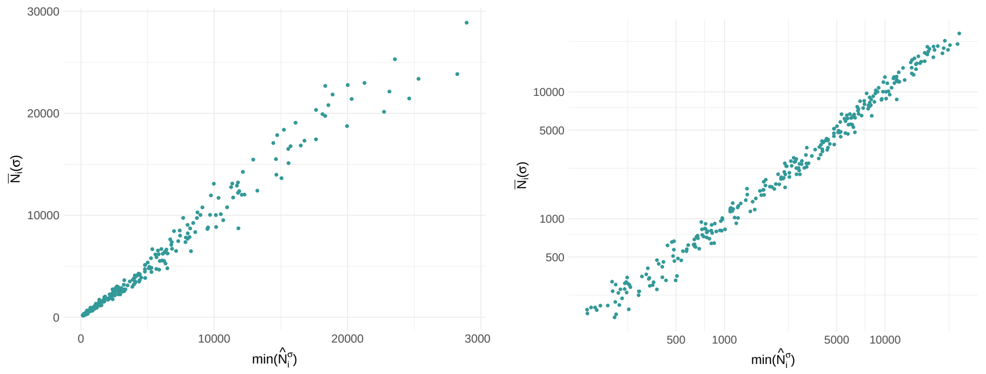

(a) Linear scaled axis **(b)** Logarithmic scaled axis

Figure 7.6: Predicted first load cycle with hazard greater than zero over simulational result.

stress and the absolute values of the single stress components:

$$\log(\bar{N}_i(\sigma)) = a_0 + a_{vM}\log(\sigma_{vM}) + \sum_{k\in\{xx,yy,zz,yz,zx\}} a_k\,|\sigma_k|. \tag{7.9}$$

Figure 7.6 displays the predictions of this regression model compared to the simulation results. The left plot (Figure 7.6a), using linear axes, shows that the predictions align closely with the simulation results. The alignment becomes even clearer when plotted on a log-log scale (Figure 7.6b). Using this regression model, we achieve an impressive r^2 value of 0.993, a significant improvement over the already high r^2 value of 0.95 obtained with the regression using only von Mises stress.

In the second step of building the surrogate model, we use a fitted smooth ReLU (rectified linear unit) to approximate the hazard density at load cycle N_i for a given stress state. The smooth ReLU function is defined as follows:

$$\mathrm{sReLU}(x) = \ln(1 + e^x). \tag{7.10}$$

ReLU functions are often used as activation functions for neural networks. The simple ReLU is defined as zero for negative inputs and the identity for positive values. The smooth ReLU is a differentiable approximation of the ReLU function.

As the smooth ReLU function approaches zero for large negative values and behaves almost linearly for large positive values, we can achieve a good fit to hazard densities using just three parameters. The actual function we use for the surrogate model is as follows

$$f(x) = a_1 \, \left(\ln(1 + e^{a_2\, x - a_3})\right). \tag{7.11}$$

With the assumption that the local cumulative hazard rate $H(N_i, \sigma)$ is almost zero for the minimal crack initiation cycle N_i^f we eliminate one parameter. We use $H(N_i^f, \sigma) = 10^{-4}$ as a threshold, with $a_1 > 0$ we obtain

$$\begin{aligned} && 0.0001 &= a_1 \left(\ln(1 + e^{a_2\, N_i^f - a_3})\right) \\ \Rightarrow && 0.0001 a_1^{-1} &= \ln(1 + e^{a_2 N_i^f - a_3}) \\ \Rightarrow && e^{0.0001 a_1^{-1}} &= 1 + e^{a_2 N_i^f - a_3} \\ \Rightarrow && e^{0.0001 a_1^{-1}} - 1 &= e^{a_2 N_i^f - a_3} \\ \Rightarrow && \ln(e^{0.0001 a_1^{-1}} - 1) &= a_2 N_i^f - a_3 \\ \Rightarrow && a_3 &= a_2 N_i^f - \ln(e^{0.0001 a_1^{-1}} - 1). \end{aligned} \tag{7.12}$$

The two remaining parameters are fitted to the simulation results using the following procedure:

For a given stress state σ, we first determine the support points for the fit. We utilize 101 equidistant load cycles $(N_i(\sigma))_j \in [N_i^f(\sigma), 3N_i^f(\sigma)]$:

$$(N_i(\sigma))_j = (1 + \frac{j}{50}) \cdot N_i^f(\sigma), \qquad j = 0, \ldots, 100 \tag{7.13}$$

We then collect the corresponding local cumulative hazard rate $H((N_i(\sigma))_j, \sigma)$ from the percolation simulations. To ensure the hazard rate increases with respect to the load cycle N_i (accounting for potential scatter), we modify the data for fitting purposes:

$$\begin{aligned} H_0^\sigma &= H((N_i(\sigma))_0), \\ H_j^\sigma &= \max\left(H((N_i(\sigma))_j), H_{j-1}^\sigma\right), \; j = 1, \ldots, 100 \end{aligned} \tag{7.14}$$

With these support points, we fit the two remaining parameters $a_1(\sigma)$ and $a_2(\sigma)$ in the function (7.11). We employ the Nelder-Mead optimization algorithm, available through the `R` library `nloptr` [42].

The fitted functions for two different stress tensors are displayed in Figure 7.7. These fitted functions closely match the results from the percolation

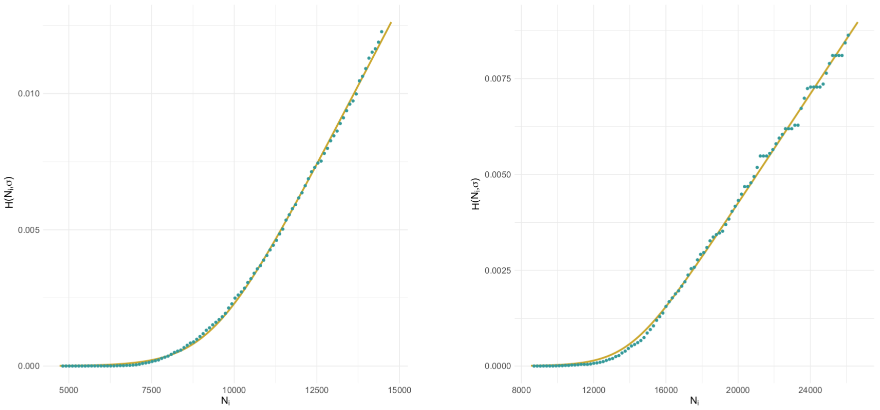

(a) Local cumulative hazard rate for stress input with $\sigma_v M = 420$ and $\kappa_\sigma = 0.85$.

(b) local cumulative hazard rate for stress input with $\sigma_v M = 380$ and $\kappa_\sigma = 0.33$.

Figure 7.7: Fitted smooth ReLU functions (yellow) for the hazard density obtained from the percolation (green).

model in both cases. Even for slightly noisy simulation results, such as those with $\sigma_{vM} = 380, \kappa_\sigma = 0.33$ (Figure 7.7b), the smooth ReLU function fits well with the data points.

Now, as a final step, we want to get the parameters for local cumulative hazard rate directly from the stress tensor, rather than from the percolation simulations. We therefore use a neural network that predicts the two parameters $a_1(\sigma)$ and $a_2(\sigma)$ directly from a given stress tensor σ. Additionally to the entries of the stress tensor $\sigma_{xx}, \sigma_{yy}, \sigma_{zz}, \sigma_{yz}$ and σ_{zx}, we use the von Mises equivalent stress σ_{vM} and $\bar{N}_i(\sigma)$ as input features for the network.

The architecture of the neural network consists of an input layer with 7 neurons, 3 hidden layers with $20, 25$ and 10 neurons and an output layer with 2 neurons and a linear activation function. For the loss function we use the mean squared error. The implementation is done with Keras and Tensorflow as the backend which are provided in the `R` [58] libraries `keras` [1] and `tensorflow` [2].

For the training of the neural network we split the database into train-

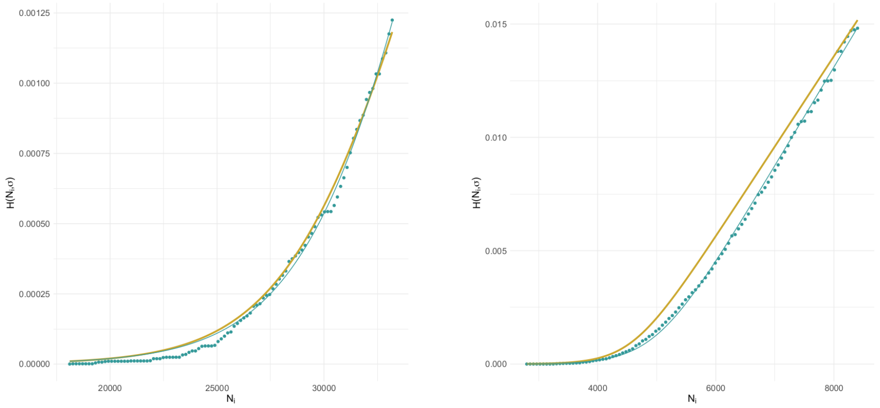

(a) Both smooth ReLU functions for von Mises stress 350 and $\kappa_\sigma = 0.5$.

(b) Both smooth ReLU functions for von Mises stress 460 and $\kappa_\sigma = 0.85$.

Figure 7.8: Comparison of the fitted (green) and the smooth ReLU gained from the neural network (yellow). The local cumulative hazard rate from the percolation model is visualized with the green dots.

and test data. Two hazard densities resulting from the test dataset with parameters gained from the trained network are depicted in Figure 7.8. In both cases the predicted hazard density and the hazard densities gained from the percolation simulation match well.

7.4 FEM Postprocessor

We now use the surrogate model from the previous section to build an FEM postprocess. Let now $\sigma(\hat{T}_{K(F)}(\hat{x}^{F_l}))$ be the stress tensors obtained from the FEM simulation in the quadrature points with $F \in \mathcal{N}_h$ and $l \in 1, \ldots, q^F$. We rotate the stress and subtract the hydrostatic part with the same procedure as introduced in Section 7.2 to obtain the input $\hat{\sigma}'_{F_l}$ for the surrogate model.

We use the linear regression from the previous section to approximate the first load cycle where the Hazard is larger than zero $\bar{N}_i(\hat{\sigma}'_{F_l})$. With the trained gradient boosting tree, we can now determine the parameters for the

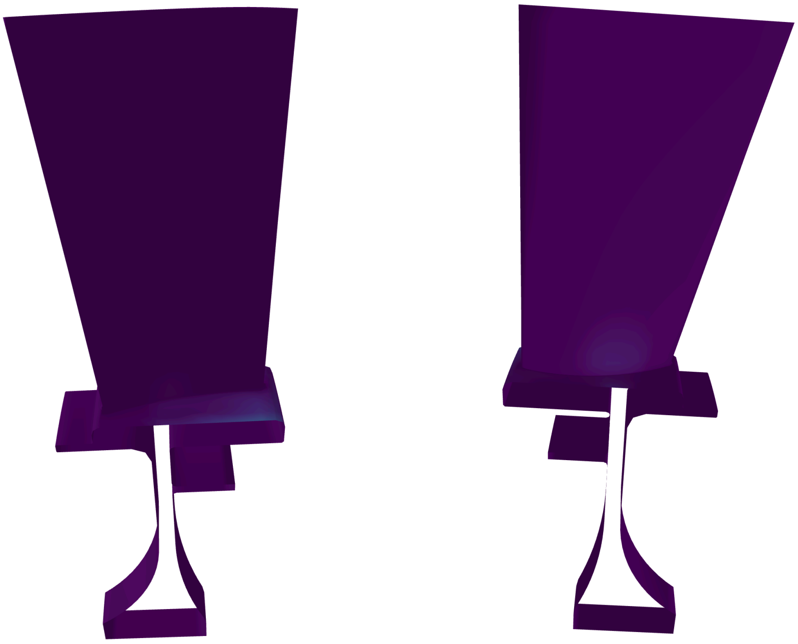

(a) Front of the blade. **(b)** Back of the blade.

Figure 7.9: Turbine blade with Hazard after 1000 load cycles, intensity from dark blue to yellow.

sReLU functions that approximate the local cumulative hazard functions

$$\begin{aligned} H(t,\sigma(\hat{T}_{K(F)}(\hat{x}^{F_l}))) &\approx \bar{H}(t,\sigma(\hat{T}_{K(F)}(\hat{x}^{F_l}))) \\ &= a_1(\hat{\sigma}'_{F_l})\left(\ln\left(1+e^{a_2(\hat{\sigma}'_{F_l})t-a_3(\hat{\sigma}'_{F_l})}\right)\right) \end{aligned} \tag{7.15}$$

at each quadrature point.

With equation (3.102) we can directly apply the local cumulative hazards to a FEM geometry. As an example we use here the blisk geometry under centrifugal load (Section 7.2). In Figure 7.9 the Hazard on the surface after 1000 load cycles is displayed.

On the back side of the blade (Figure 7.9b) there is no damage on the whole surface. If we look at the front side of the turbine blade (Figure 7.9a) at the right edge of the base there is already a hazard above 0.

After 5000 load cycles (Figure 7.10), the hazards on the right edge of the base have grown (Figure 7.10a). The hazard intensity increases. On the back side (Figure 7.10b) there is an area at the transition of the blade to the base which now is also damaged. With increasing load cycles these

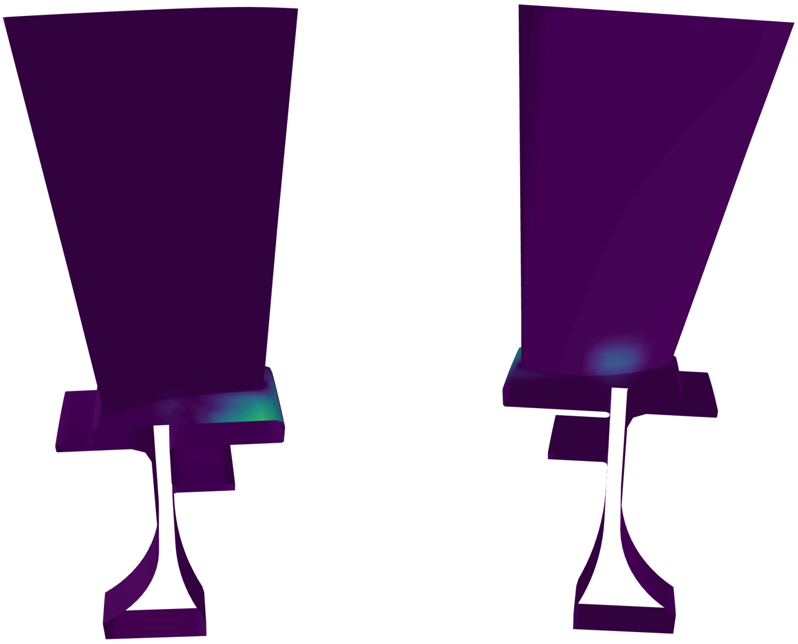

(a) Front of the blade. **(b)** Back of the blade.

Figure 7.10: Turbine blade with Hazard after 5000 load cycles, intensity from dark blue to yellow.

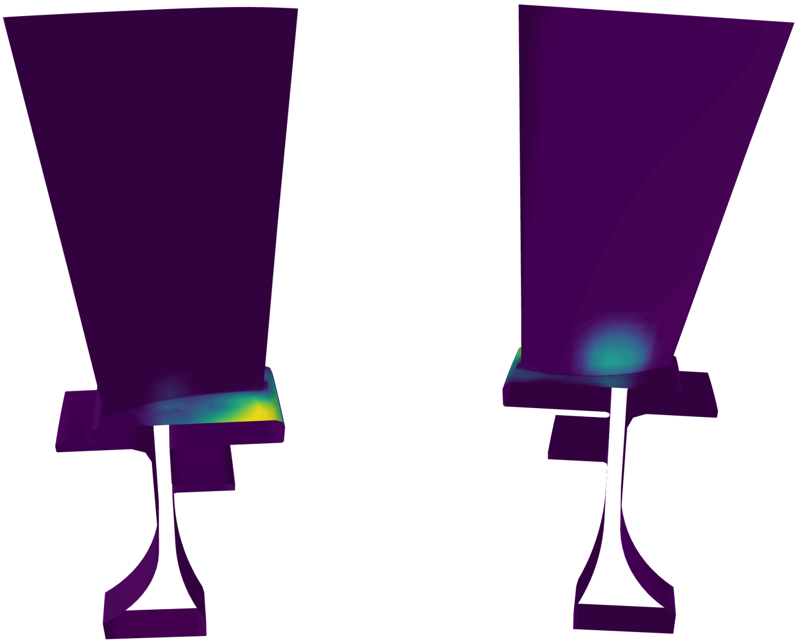

(a) Front of the blade. **(b)** Back of the blade.

Figure 7.11: Turbine blade with Hazard after 10000 load cycles, intensity from dark blue to yellow.

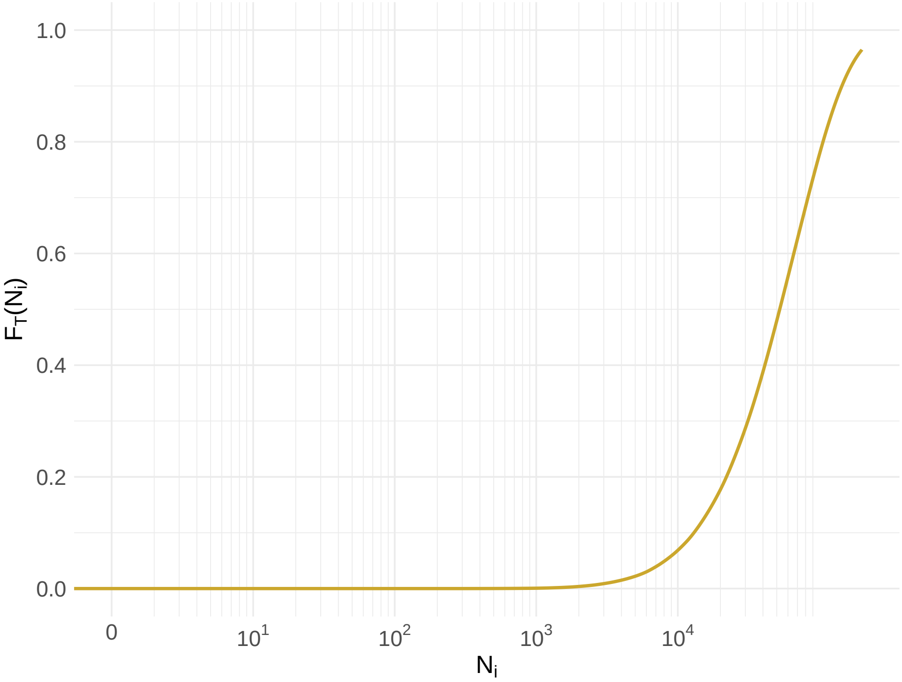

Figure 7.12: Probability of failure over load cycle for the turbine blade

areas become larger and the intensity of the hazards grows. At the front of the blade, after 10 000 load cycles (Figure 7.11) the transition area between base and blade is now damaged as well (Figure 7.11a).

The areas on the surface of the blade which have high hazards correlate with the areas with high von Mises stress (Figure 7.3).

With equation (3.103) we now can determine the LCF-failure probability of the whole blisk blade, which is depicted in Figure 7.12. Up to about 1200 start-stop operations, the blade operates in the safe-life regime. Here, the probability of failure is approximately zero. After about 13000 start-stop operations, the probability of failure exceeds 10% and increases fast.

The resulting failure probability is of a realistic order magnitude. Purely statistical failure models, such as Weibull-based approaches, have the problem when transferring to realistic large components that even with a few load cycles, there is a risk of failure. With our local physical based approach and the approach via local hazard rates, we are able to predict a realistic safe-life regime.

Another advantage of the chosen approach is its flexibility in utilizing various microstructural models to determine local hazard rates. The transfer to the component is independent of the details of the microstructural model.

8. Conclusion and Outlook

In this thesis, we developed a probabilistic model for low cycle fatigue lifetime prediction of nickel-bases alloys. This physics based approach is derived from the random orientations of the individual grains in the microstructure and the anisotropic characteristic of the material. We combined the single grain failure times with an infection mechanism. To this end, we used FEM simulations to calculate the local excess in shear stress that is induced due to a crack in an adjacent grain. As the FEM simulations are time-consuming, we built a gradient boosting based surrogate model for the infection function.

In Section 4 we fitted the model, using failure time data obtained from LCF experiments under uniaxial loading conditions. We could observe, that the infection model reduce the scatter band of the predicted probability of failure in comparison to the model without the infection. The resulting failure times are in the correct order of magnitude.

Within Section 6 we utilized the linearity of the elastic equation and the linearity of the Schmid factors to extend the infection model to multiaxial stress states. Additionally, the multiaxial version of the infection model takes the orientation of the grain boundary into account. The model was fitted to experimental results with uniaxial loading conditions. The validation with multiaxial experiments showed that our model is not able to predict the failure times correctly for these loading conditions. In the experiments an increase in multiaxiality leads to an overall longer LCF lifetime of the specimens, in the percolation model we observe the opposite effect. This is due to an increase in Schmid factors under uniaxial loading conditions. To correct the predictions a linear shift of the Coffin-Manson-Basquin equation was introduced.

We found that an increase in multiaxiality leads not only to an increase in Schmid factors but also to a reduction in stress intensity. The crack initiation in a single grain is not only driven by the dislocation movements along the slip systems but also by a cyclic crack opening. A promising approach to predict the failure times under multiaxial load purely from the microstructure, even without an additional linear shift, would therefore be to use the stress intensity factors for crack initiation in addition to the Schmid factors.

In Section 5.1 we presented an approach to model orientation distributions, which differ from the isotropic distribution, with a small dataset via neural networks. In combination with the percolation model, we were able to show in Section 6.5 that the directional solidification of the nickel-based alloy leads to longer lifetimes and larger scatter of the failure times.

In Section 5.2 we have presented a modeling approach for the integration of transcrystalline crack initiation into the percolation model. Here we used two different attempts to determine the crack initiation times of the grain boundary. On the one hand, the crack initiation times were determined purely via the shear stress at the grain boundary, which leads to very high crack initiation cycles, such that the grain boundaries have no influence on the percolation model. On the other hand, in the second approach, we used a combination of shear stress and normal stress for the crack initiation. It turns out that this leads to a much too early crack initiation, with many grain boundaries forming cracks before the first grain is cracked. Here, a more detailed investigation of the mechanism of transcrystalline crack initiation is necessary for accurate modeling.

In combination with the percolation model it turns out, that for forming clusters that lead to an overall failure, intercrystalline crack growth is necessary.

Within Section 7, a method was presented to transfer probabilistic microstructural failure models to large engineering components. An advantage of this method is that it works independently of the microstructural model and thus other microstructural failure models are also usable.

As the calculation of the local cumulative hazard rates requires a lot of computing time, we have used a neural network as a surrogate model. This means that most of the computing time is required offline, which results in a fast FEM post-processor.

As an example we transferred the local cumulative hazard rates to a turbine blade in Section 7.4. The regions with high von Mises stress correlate here with the regions that have a high probability of crack initiation.

When considering the overall probability of the turbine blade, we found that we get a realistic safe-live regime of about 1000 load cycles. This is an advantage of our modeling compared to classical purely statistical approaches with, for example, Weibull models, which for large components predict spontaneous failure at only a few load cycles due to the size effect.

9. References

[1] JJ Allaire and François Chollet. *keras: R Interface to 'Keras'*. R package version 2.9.0. 2022.

[2] JJ Allaire and Yuan Tang. *tensorflow: R Interface to 'TensorFlow'*. R package version 2.9.0. 2022.

[3] José David Arregui-Mena, Lee Margetts, and Paul M. Mummery. "Practical Application of the Stochastic Finite Element Method". In: *Archives of Computational Methods in Engineering* 23.1 (Mar. 1, 2016), pp. 171–190.

[4] U. Bayerlein and H.G. Sockel. "Determination of Single Crystal Elastic Constants from DS- and DR-Ni-Based Superalloys by a New Regression Method Between 20C and 1200C". In: *Superalloys 1992 (Seventh International Symposium)*. Superalloys. TMS, 1992, pp. 695–704.

[5] Stefano Beretta, S. Foletti, and Andrea Sanguineti. *A Simple Format for the Definition of Safety Factors for LCF*. Vol. 7. June 16, 2014.

[6] Laura Bittner and Hanno Gottschalk. "Optimal reliability for components under thermomechanical cyclic loading." In: *Control & Cybernetics* 45.4 (2016).

[7] Béla Bollobás, Bela Bollobás, and Oliver Riordan. *Percolation*. Cambridge University Press, 2006.

[8] Matthias Bolten, Hanno Gottschalk, and Sebastian Schmitz. "Minimal Failure Probability for Ceramic Design Via Shape Control". In: *Journal of Optimization Theory and Applications* 166.3 (Sept. 1, 2015), pp. 983–1001.

[9] Matthias Bolten et al. "Numerical Shape Optimization to Decrease Failure Probability of Ceramic Structures". In: *PAMM* 18 (Apr. 17, 2017).

[10] Dietrich Braess. *Finite Elemente.* Springer-Lehrbuch. Berlin, Heidelberg: Springer, 1992.

[11] N. V. Chawla et al. “SMOTE: Synthetic Minority Over-sampling Technique”. In: *Journal of Artificial Intelligence Research* 16 (June 1, 2002), pp. 321–357.

[12] W.R. Chen and L.M. Keer. “Fatigue crack growth in mixed mode loading”. In: *Journal of Engineering Materials and Technology, Transactions of the ASME* 113.2 (Jan. 1991), pp. 222–227.

[13] Denise Chenais. “On the Existence of a Solution in a Domain Identification Problem”. In: *Journal of Mathematical Analysis and Applications* 52.2 (Nov. 1, 1975), pp. 189–219.

[14] P. G. Ciarlet. “Basic Error Estimates for Elliptic Problems”. In: *Handbook of Numerical Analysis.* Vol. 2. Finite Element Methods (Part 1). Elsevier, Jan. 1, 1991, pp. 17–351.

[15] R. S. J. Corran and S. J. Williams. “Lifing Methods and Safety Criteria in Aero Gas Turbines”. In: *Engineering Failure Analysis.* UK Technical Advisory Group for Structural Integrity (TAGSI)Design Margins and Safety Factors Relating to Structural Integrity 14.3 (Apr. 1, 2007), pp. 518–528.

[16] F. Coudon et al. “A Multiscale Model for Nickel-Based Directionally Solidified Materials”. In: *International Journal of Plasticity* 115 (Apr. 1, 2019), pp. 1–17.

[17] Laurens De Haan, Ana Ferreira, and Ana Ferreira. *Extreme value theory: an introduction.* Vol. 21. Springer, 2006.

[18] Guido Dhondt. “CalculiX CrunchiX USER’S MANUAL Version 2.18”. In: (Sept. 15, 2021).

[19] Jürgen Elstrodt. *Maß- und Integrationstheorie.* Berlin, Heidelberg: Springer, 2018.

[20] B. Engel et al. “Effect of local anisotropy on fatigue crack initiation in a coarse grained nickel-base superalloy”. In: *MATEC Web Conf.* 165 (2018), p. 04004.

[21] B. Engel et al. “Influence of grain orientation distribution and stress gradient on the high temperature fatigue behaviour of polycrystalline Nickel base superalloys – an experimental and numerical approach”. October 2019: In preparation.

[22] B. Engel et al. “Probabilistic modeling of slip system-based shear stresses and fatigue behavior of coarse-grained Ni-base superalloy considering local grain anisotropy and grain orientation”. In: *Metals* 9.8 (2019).

[23] Benedikt Engel. “High Temperature Low-Cycle Fatigue of the Ni-base Superalloy RENÉ80”. In: *LCF8*. 2017.

[24] Alexandre Ern and Jean-Luc Guermond. *Theory and Practice of Finite Elements*. Vol. 159. Springer, 2004.

[25] Geuzaine, Christophe and Remacle, Jean-Francois. *Gmsh*. Version 4.6.0. June 22, 2020.

[26] H. Gottschalk and S. Schmitz. “Optimal Reliability in Design for Fatigue Life”. In: *SIAM Journal on Control and Optimization* 52.5 (Oct. 2012).

[27] H. Gottschalk et al. “Probabilistic Schmid factors and scatter of low cycle fatigue (LCF) life”. In: *Mat.-wiss u. Werkstofftech.* 45.2 (2015), pp. 156–164.

[28] Hanno Gottschalk and Marco Reese. “An analytical study in multiphysics and multi-criteria shape optimization”. In: *Journal of Optimization Theory and Applications* 189.2 (2021), pp. 486–512.

[29] Hanno Gottschalk and Mohamed Saadi. “Shape gradients for the failure probability of a mechanic component under cyclic loading: a discrete adjoint approach”. In: *Computational Mechanics* 64.4 (2019), pp. 895–915.

[30] Hanno Gottschalk and Sebastian Schmitz. “Optimal Reliability in Design for Fatigue Life”. In: *SIAM Journal on Control and Optimization* 52.5 (Jan. 2014), pp. 2727–2752.

[31] Hanno Gottschalk et al. “Adjoint method to calculate the shape gradients of failure probabilities for turbomachinery components”. In:

Turbo Expo: Power for Land, Sea, and Air. Vol. 51135. American Society of Mechanical Engineers. 2018, V07AT32A003.

[32] Hanno Gottschalk et al. “Probabilistic Schmid factors and scatter of low cycle fatigue (LCF) life: Probabilistischer Schmid-Faktor und Streuband der Lebensdauer bei niedrigen Lastspielzahlen (LCF)”. In: *Materialwissenschaft und Werkstofftechnik* 46.2 (2015), pp. 156–164.

[33] G. Gottstein. *Physikalische Grundlagen der Materialkunde*. Springer-Lehrbuch. Springer Berlin Heidelberg, 2013.

[34] Brandon Greenwell et al. *gbm: Generalized Boosted Regression Models*. R package version 2.1.8. 2020.

[35] D. Gross and T. Seelig. *Bruchmechanik - mit einer Einführung in die Mikromechanik*. Berlin (u.a.): Springer, Jan. 2001.

[36] M.M. Hadj. “Estimation of mixed-mode stress intensity factors with presence of the confinement parameters T-stress and A3”. In: *Advanced Engineering Forum* (2016).

[37] Mathis Harder et al. “Probabilistic Modeling of LCF Failure Times Using a Epidemiological Crack Percolation Model”. In: *ECCOMAS Congress 2022 - 8th European Congress on Computational Methods in Applied Sciences and Engineering* Computational Solid Mechanics (Nov. 25, 2022).

[38] Trevor Hastie et al. *The elements of statistical learning: data mining, inference, and pre diction*. Vol. 2. Springer, 2009.

[39] W. K. Hastings. “Monte Carlo Sampling Methods Using Markov Chains and Their Applications”. In: *Biometrika* 57.1 (Apr. 1, 1970), pp. 97–109.

[40] Mark Horstemeyer. “Multiscale Modeling: A Review”. In: *Practical Aspects of Computational Chemistry*. Oct. 3, 2009, pp. 87–135.

[41] Gareth James et al. *An Introduction to Statistical Learning: With Applications in R*. Springer Texts in Statistics. New York, NY: Springer US, 2021.

[42] Steven G. Johnson. *The NLopt nonlinear-optimization package*.

[43] Olav Kallenberg. *Random Measures*. Elsevier Science & Technology Books, 1983. 196 pp.

[44] Olav Kallenberg. *Random Measures, Theory and Applications.* Vol. 77. Probability Theory and Stochastic Modelling. Cham: Springer International Publishing, 2017.

[45] Peter Knabner and Lutz Angermann. *Numerical Methods for Elliptic and Parabolic Partial Differential Equations: With Contributions by Andreas Rupp.* Vol. 44. Texts in Applied Mathematics. Cham: Springer International Publishing, 2021.

[46] H. Gottschalk L. Mäde S. Schmitz and T. Beck. “Combined notch and size effect modeling in a local probabilistic approach for LCF”. In: *Computational Materials Science* 142 (2018), pp. 377–388.

[47] Jean-Sebastien Lecomte and Hans-Joachim Bunge. *Texture Analysis in Materials Science H.-J. Bunge.* May 28, 2015.

[48] Alexander Liefke et al. “Towards Multidisciplinary Turbine Blade Tolerance Design Assessment Using Adjoint Methods”. In: *Turbo Expo: Power for Land, Sea, and Air.* Vol. 84096. American Society of Mechanical Engineers. 2020, V02DT38A008.

[49] L. Mäde et al. “Probabilistic LCF Risk Evaluation of a Turbine Vane by Combined Size Effect and Notch Support Modeling”. In: *Proc. ASME. 50923.* Vol. 7A: Structures and Dynamics. GT2017-64408. ASME. June 2017, V07AT32A004.

[50] Lucas Mäde. “Probabilistic modeling of stress gradients, microstructural and size size effects in low-cycle fatigue”. PhD thesis. Technical University of Kaiserslautern, 2019.

[51] G. Martin et al. “A multiscale model for the elastoviscoplastic behavior of Directionally Solidified alloys: Application to FE structural computations”. In: *International Journal of Solids and Structures* 51.5 (2014), pp. 1175–1187.

[52] Nadine Moch. “From Macroscopic Models of Damage Accumulation to Probability of Failure of Gas Turbines”. PhD thesis. Facultiy of Mathematics Bergische Universität Wuppertal, 2018.

[53] Haël Mughrabi. “Microstructural Mechanisms of Cyclic Deformation, Fatigue Crack Initiation and Early Crack Growth”. In: *Philosophical*

Transactions of the Royal Society A: Mathematical, Physical and Engineering Sciences 373.2038 (Mar. 28, 2015), p. 20140132.

[54] Sergey Nazarov and Boris A. Plamenevsky. “Elliptic Problems in Domains with Piecewise Smooth Boundaries”. In: *Elliptic Problems in Domains with Piecewise Smooth Boundaries*. De Gruyter, June 1, 2011.

[55] Robert Newnham. *Properties of Materials: Anisotropy, Symmetry, StructureAnisotropy, Symmetry, Structure*. Nov. 11, 2004.

[56] Xiao-Peng Niu et al. “Probabilistic Modeling of Uncertainties in Fatigue Reliability Analysis of Turbine Bladed Disks”. In: *International Journal of Fatigue* 142 (Jan. 1, 2021), p. 105912.

[57] Vissarion Papadopoulos and Dimitris G. Giovanis. *Stochastic Finite Element Methods*. Mathematical Engineering. Cham: Springer International Publishing, 2018.

[58] R Core Team. *R: A Language and Environment for Statistical Computing*. R Foundation for Statistical Computing. Vienna, Austria, 2020.

[59] Christian P. Robert. *The Metropolis-Hastings Algorithm*. Jan. 27, 2016. URL: `http://arxiv.org/abs/1504.01896` (visited on 09/11/2023). preprint.

[60] Joachim Rösler, Harald Harders, and Martin Bäker. *Mechanical Behavior of Materials*. 4th ed. Springer Vieweg, 2012.

[61] S. Schmitz et al. “A Probabilistic Model for LCF”. In: *Computational Materials Science* 79 (2013), pp. 584–590.

[62] S. Schmitz et al. “Risk estimation for LCF crack initiation”. In: *Proc. ASME. 55263*. Vol. 7A: Structures and Dynamics. GT2013-94899 GT2013-94899. ASME. June 2013, V07AT27A007.

[63] Sebastian Schmitz. “A Local and Probabilistic Model for Low-Cycle Fatigue”. PhD thesis. Faculty of Informatics of the Universita della Svizzera Italiana, 2014.

[64] M. M. Shenoy, R. S. Kumar, and D. L. McDowell. “Modeling Effects of Nonmetallic Inclusions on LCF in DS Nickel-Base Superalloys”. In: *International Journal of Fatigue* 27.2 (Feb. 1, 2005), pp. 113–127.

[65] Wacharasak Siriseriwan. *smotefamily: A Collection of Oversampling Techniques for Class Imbalance Problem Based on SMOTE*. R package version 1.3.1. 2019.

[66] Severin Strobl, Arno Formella, and Thorsten Pöschel. “Exact Calculation of the Overlap Volume of Spheres and Mesh Elements”. In: *Journal of Computational Physics* 311 (Apr. 15, 2016), pp. 158–172.

[67] K. Tanaka. “Fatigue crack propagation from a crack inclined to cyclic tensile axis”. In: *Engineering Fracture Mechanics* 6 (Oct. 1974), pp. 493–507.

[68] Luc Tarta. *An Introduction to Sobolev Spaces and Interpolation Spaces*. Vol. 3. Lecture Notes of the Unione Matematica Italiana. Berlin, Heidelberg: Springer, 2007.

[69] Salvatore Torquato and HW Haslach Jr. “Random heterogeneous materials: microstructure and macroscopic properties”. In: *Appl. Mech. Rev.* 55.4 (2002), B62–B63.

[70] Kevin Ushey, JJ Allaire, and Yuan Tang. *reticulate: Interface to 'Python'*. R package version 1.25. 2022.

[71] Michael Wächter, Christian Müller, and Alfons Esderts. *Angewandter Festigkeitsnachweis nach FKM-Richtlinie: Kurz und bündig*. Wiesbaden: Springer Fachmedien, 2021.

[72] Guang-Jian Yuan et al. “Low-Cycle Fatigue Life Prediction of a Polycrystalline Nickel-Base Superalloy Using Crystal Plasticity Modelling Approach”. In: *Journal of Materials Science & Technology* 38 (Feb. 2020), pp. 28–38.

[73] Clarence Zener. “Contributions to the Theory of Beta-Phase Alloys”. In: *Phys. Rev.* 71 (12 June 1947), pp. 846–851.

[74] S. P. Zhu, S. Foletti, and S. Beretta. “Probabilistic Framework for Multiaxial LCF Assessment under Material Variability”. In: *International Journal of Fatigue* 103 (Oct. 1, 2017), pp. 371–385.

[75] Shun-Peng Zhu et al. “Computational-Experimental Approaches for Fatigue Reliability Assessment of Turbine Bladed Disks”. In: *International Journal of Mechanical Sciences* 142–143 (July 1, 2018), pp. 502–517.